UNIVERSITY
OF MICHIGAN
FEB 21 1951
ENGINEERING
LIBRARY

JOURNAL OF THE AERONAUTICAL SCIENCES

VOLUME 18 FEBRUARY, 1951 NUMBER 2

CONTENTS

The Minimum Drag of Thin Wings in Frictionless Flow ..... ROBERT T. JONES 75

Design and Performance of a Simple Interferometer for Wind-Tunnel Measurements ..... HARRY I. ASHKENAS AND ARTHUR E. BRYSON 82

Remarks on Low-Aspect-Ratio Configurations in Supersonic Flow ..... P. A. LAGERSTROM AND M. E. GRAHAM 91

Wind-Tunnel Tests for Temperature Recovery Factors at Supersonic Velocities ..... W. F. HILTON 97

Structural Load Measurements on Complex Aircraft Components Using Strain-Gage Summation Circuits ..... MAURICE A. WALTER 101

Conical Flow Methods Applied to Uniformly Loaded Wings in Subsonic Flow ..... SEYMOUR LAMPERT 107

Calculation of Thermal Stresses in a Wedge-Shaped Wing ..... GEORGE H. EISENHARDT AND WARREN M. ROHSENOW 115

Buckling Load of a Stepped Column ..... FREDERIC M. HOBLIT 124

On Some Special Problems in Linearized Axially Symmetric Flow ..... BERTRAND DES CLERS AND CHIEH-CHIEN CHANG 127

Readers' Forum: "Generalized Complex Forces in Flutter Calculations," by J. E. V. Nilsson and N. B. Langefors; "Vibrations of Rectangular Plates," by Harold Lurie; "On Supersonic Wing-Body Center of Pressure," by G. K. Morikawa and T. F. Coleman; "Airplane Pitching Moment of Inertia," by Innes Bouton; "Base Pressures at Supersonic Speeds," by J. Leith Potter; "A Simple Graphical Solution of the Duhamel Integral," by E. V. Laitone and J. T. Ahlin; "Aerodynamics of Blasts," by L. Ting and H. F. Ludloff 139–144

Published by the

INSTITUTE OF THE AERONAUTICAL SCIENCES, INC.

JOURNAL OF THE AERONAUTICAL SCIENCES

Editor: HUGH L. DRYDEN, *Director, N.A.C.A.*

Associate Editor: ROBERT R. DEXTER *Managing Editor:* BERNEICE H. JARCK

The Institute of the Aeronautical Sciences publishes monthly the JOURNAL OF THE AERONAUTICAL SCIENCES and the AERONAUTICAL ENGINEERING REVIEW.

The JOURNAL OF THE AERONAUTICAL SCIENCES prints papers of scientific and technical interest to Institute members and subscribers. In general, it provides an opportunity for specialists to publish articles disclosing new knowledge and new applications in the field of the aeronautical sciences. The JOURNAL restricts itself to the aeronautical aspects of advances in science and engineering, and papers printed have either been submitted directly to the JOURNAL or have been previously presented at a meeting of the Institute.

The AERONAUTICAL ENGINEERING REVIEW keeps members and subscribers informed regarding the contents of new books and current periodicals in the field of aeronautics. It reviews new developments in the aircraft industry and reports on progress from house organs and catalogs published by aircraft and engine manufacturers and other companies engaged in aeronautical activities. It publishes papers on applied engineering and aircraft production. News of Institute activities is published in the REVIEW.

Statements and opinions expressed in the JOURNAL are to be understood as individual expressions of the authors and not those of the Institute.

SUBSCRIPTION RATES

Journal of the Aeronautical Sciences
Published Monthly

United States and Possessions		Foreign Countries Including Canada (American Currency Rate)	
1 Year	$12.00	1 Year	$13.00
Single Copies	1.50	Single Copies	1.50

Aeronautical Engineering Review
Published Monthly

United States and Possessions		Foreign Countries Including Canada (American Currency Rates)	
1 Year	$3.00	1 Year	$3.50
Single Copies	0.50	Single Copies	0.50

Notices of change of address should be sent to the Institute at least 30 days prior to actual change of address.

Manuscripts for publication, proofs, and all correspondence should be addressed to the Editorial Office of the JOURNAL.

Correspondence regarding subscriptions may be addressed to Publication Office, 20th and Northampton Sts., Easton, Pa., or to the Editorial Office of the JOURNAL OF THE AERONAUTICAL SCIENCES, 2 East 64th Street, New York 21, New York.

Copyright, 1951, by the Institute of the Aeronautical Sciences, Inc.

Entered as Second Class Matter at the Post Office, Easton, Pa., May 1, 1937. Acceptance for mailing at a special rate of Postage provided for in the Act of August 24, 1912. Authorized April 29, 1937.

JOURNAL OF THE AERONAUTICAL SCIENCES

VOLUME 18 FEBRUARY, 1951 NUMBER 2

The Minimum Drag of Thin Wings in Frictionless Flow

ROBERT T. JONES*

Ames Aeronautical Laboratory, N.A.C.A.

SUMMARY

The assumptions of the thin airfoil theory are found to provide certain necessary conditions for the minimum drag of airfoils having a given total lift, a given maximum thickness, or a given volume. The conditions are applicable to steady or unsteady motions and to subsonic or supersonic speeds without restriction on the plan form. The computation of drag and the statement of the conditions for minimum drag depend on the consideration of a "combined flow field," which is obtained by superimposing the disturbance velocities in forward and reversed motions.

If the plan form of the airfoil and its total lift are given, it is found that, for minimum drag, the lift must be distributed in such a way that the downwash in the combined field is constant over the entire plan form. If the plan form is given and the thickness of the airfoil is required to contain a specified volume, then the thickness must be distributed over the plan form in such a way that the pressure gradient of the combined field in the direction of flight is constant at all points of the wing. A specification of the thickness along some line drawn on the plan form is found to lead to the requirement that the gradient of the pressure vanishes on either side of this line. For the drag to be a minimum with respect to small changes in the plan form, the foregoing conditions must extend continuously for a small distance beyond the edge of the plan form.

INTRODUCTION

THE DRAG OF A BODY moving through a fluid is attributable partly to the action of tangential, or friction, forces and partly to the action of normal pressures. With well-streamlined bodies, the friction forces are ordinarily confined to a relatively thin boundary layer adjacent to the surface, and in such cases that part of the drag arising from the normal pressures can be determined on the assumption of a frictionless potential motion in the region outside the boundary layer.

A practical way of minimizing the pressure component of the drag is to make the body slender and its angle of attack small. Many of the results of the modern airfoil theory, such as the theory of the induced drag of airfoils, are based on the assumption that the velocities imparted to the air are small in relation to the velocity of flight and, hence, are limited to cases of thin airfoils and small lift coefficients.

In the present paper, certain necessary conditions for the minimum pressure drag of thin airfoils are derived. The analysis makes use of, and extends, certain "reversed flow" theorems originally derived by Hayes[1] and von Kármán[2] and is based on the idea of superimposing the disturbances in forward and reversed motions originally advanced by Munk.[3] Although the analysis is restricted to motions involving small disturbances, the conditions for minimum drag are found to be applicable in a wide variety of circumstances of such motions. Thus, the motion may be steady or unsteady and the velocity of flight may be greater or less than the velocity of sound.

MINIMUM DRAG DUE TO THICKNESS

In the linearized theory the effects of camber, or lift, and thickness can be treated independently and later superimposed in any desired linear combination. Wing problems can therefore be divided into two classes—i.e., those involving thickness but no lift and those involving a distribution of lift over a surface having zero thickness.

Consider first the case of a thin nonlifting body or wing, such as shown in Fig. 1. The surface is assumed to be everywhere nearly parallel to a horizontal plane in the direction of motion. A distribution of thickness, symmetrical above and below this plane, is supposed to be given over the plan form. Computation of the drag of such a body will involve, first, the determination of the pressure distribution over its surface. The drag may then be obtained by one of two methods. In the first method the body is divided into elements of area, and the element of drag is obtained from the in-

Presented at the Aerodynamics Session, Annual Summer Meeting, I.A.S., Los Angeles, July 12–14, 1950.

* Aeronautical Engineer.

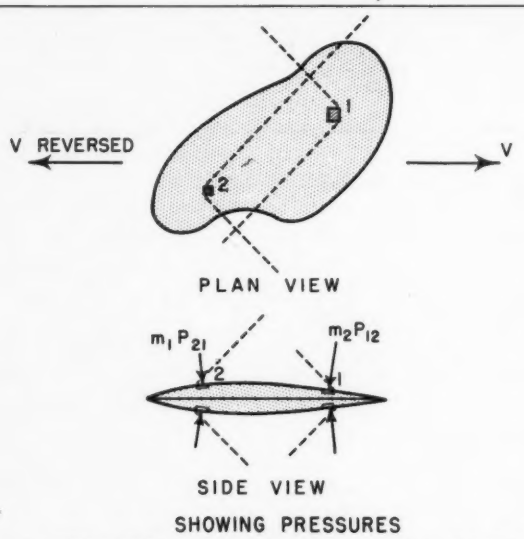

FIG. 1. Thin airfoil with elements representing slope of surface.

clination of the local pressure force. In the second method, which is related to the first through an integration by parts, the body is divided into small elements of volume, and the drag is computed from the force of buoyancy on each element arising from the local gradient of the pressure distribution.

As is well known, the pressure distribution over such a thin, nearly flat body can be calculated by considering only the inclinations or slopes of the surface elements—without regard for the actual displacement of the surface away from the mean plane. The body can then be replaced by a large number of small elementary areas having slopes equal to the local slope of the surface. Each such element can be conceived to create a disturbance field of its own, and the geometric character of this field will depend on the properties of the medium (its elasticity, density, etc.) and on the circumstances of the motion. The disturbance fields of all elements will be alike except for a factor of strength, which is measured by the product of the area of the element and its slope. The total disturbance field of the body may be obtained by superimposing the individual disturbance fields of its elements.

With the aid of this concept of superposition it may be shown that the drag of such a body is unchanged by a reversal of the direction of motion. The pressure at each point of the body is obtained by summing up the influence at this point of every element of the surface. The drag is then obtained by a second summation involving the total pressure force on each element and the slope of its surface in the dragwise direction. Thus, two integrations over the surface are required— or four integrals in all. A typical single element of this sum (see Fig. 1) will be represented by the pressure force on element 2 caused by the pressure field of element 1 and multiplied by the slope of element 2. Now the pressure field of any element, regardless of the distribution or zone of action of the pressure, will be proportional in magnitude to the slope and area of the element. The magnitude of the small contribution to the pressure on element 2 caused by element 1 will therefore be given by the product m_1P_{21}, where m_1 is the "strength" of element 1 as determined from the product of its slope by its elementary area (i.e., m_1 is equal to the frontal area of element 1) and where P_{21} is the pressure arising at element 2 from a unit disturbance at element 1. The increment of drag produced will be equal to the product of the pressure m_1P_{21} by the area and the slope of element 2—i.e., $m_1P_{21}m_2$. In reversed motion, element 1 will lie in the same relation to element 2 formerly occupied by 2 in relation to 1. Hence, P_{21} is equal to P_{12} provided the fluid itself is homogeneous. The signs of m_1 and m_2 are both changed, but their product retains the same sign. The corresponding element of drag in reversed motion is, therefore, $m_2P_{12}m_1$, which is exactly equal to the element of drag in forward motion. Such an equality can be assigned to every pair of elements and therefore must apply to the total drags on forward and reversed motion.

It should be noted that the reversal principle involves hardly any restrictive assumptions aside from those involved in the linearization. It applies, therefore, to steady or accelerated motions and to subsonic or supersonic speeds.

The fact that the drag of the body is the same for either direction of motion leads to the consideration of a method of computing the drag wherein the forward and reversed disturbance fields are considered simultaneously. It is found that the sum of the two drags, or twice the actual drag, can be obtained by superimposing the two fields of disturbance velocities and considering the pressures that would arise from motion of the combined field in the flight direction. The superposition of the two disturbance fields produces a fore-and-aft symmetry in the disturbance field of each element, with the result that the combined flow field is generally simpler in structure than the actual physical field and the calculation of drag is simplified. The pressure in the combined field is simply the difference between the pressures in forward and reversed motions.

It can be shown that in the combined flow field the mutual interference drags of two distributions of thickness are equal. Consider two distributions A and B as illustrated in Fig. 2. The two distributions can be divided into an equal number of elements, and elements from the two distributions may then be paired in an arbitrary way. Considering two elements such as 1 and 2 shown in Fig. 2, it is evident from the symmetry of the combined field of each element that the drag of element 1 caused by element 2 is equal to the drag of element 2 caused by element 1. Since this equality holds for every pair of elements, it must hold for the total distributions A and B.

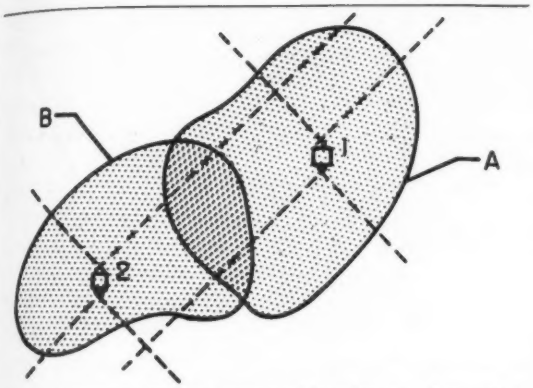

FIG. 2. Elements showing the mutual interference of two wings in combined flow.

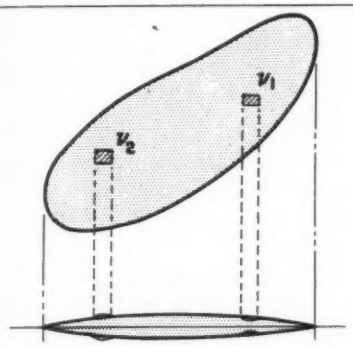

AIRFOIL SHOWING ADDITION OF EQUAL OPPOSITE ELEMENTS OF VOLUME.

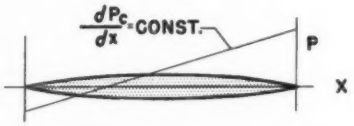

PRESSURE DISTRIBUTION FOR WHICH DRAG OF ADDED ELEMENTS IS ZERO.

FIG. 3a (*top*). FIG. 3b (*bottom*).

We are now in a position to determine the conditions for minimum drag with various specifications of thickness or volume. Consider, first, the following problem: Let the plan form of the wing be given, and suppose that the thickness distribution is required to contain a certain specified volume. What distribution of thickness over the plan form will result in the minimum drag? First, let a distribution of thickness having the specified volume and designed to achieve the minimum drag be given. If the drag is actually a minimum, then a small variation in the shape of the distribution will produce no first-order change in the drag. The variation in shape must not change the original volume and, hence, may be divided into pairs of elements having equal and opposite volumes. The drag of each element is a force of buoyancy equal to the volume of the element multiplied by the local gradient of the pressure.

Consider two such elements of volume added to the original distribution as shown in Fig. 3. Following the principle of superposition, the drag added by the elements will be composed of three parts: (1) the drag of the elements in their own pressure fields; (2) the drag added to the original distribution by the pressure fields of the elements; and (3) the drag of the elements in the pressure field of the original distribution. Since the variation in thickness distribution is small compared to the original thickness, item (1) will be of smaller order than (2) or (3).* Furthermore, if use is made of the combined flow field, items (2) and (3) will be equal because of the mutual drag theorem previously demonstrated. The added drag is then equal to twice the buoyancy of the volume elements in the pressure field of the original distribution. Denoting the pressure in the combined field by P_c and the volumes of the elements by v_1 and v_2, as in Fig. 3, we have the following two equations:

(1) *For no change in total volume:* $v_1 + v_2 = 0$

(2) *For no change in drag:* $v_1\left(\frac{\partial P_c}{\partial x}\right)_1 + v_2\left(\frac{\partial P_c}{\partial x}\right)_2 = 0$

The two equations will be consistent if

$$(\partial P_c/\partial x)_1 = (\partial P_c/\partial x)_2$$

Since such equations must hold for all positions of the elements within the specified plan form, we conclude that the pressure gradient $\partial P_c/\partial x$ must have the same value at all points of the wing. For minimum

* The fact that the second-order variation in drag is always positive ensures that a stationary value will be a minimum and not a maximum.

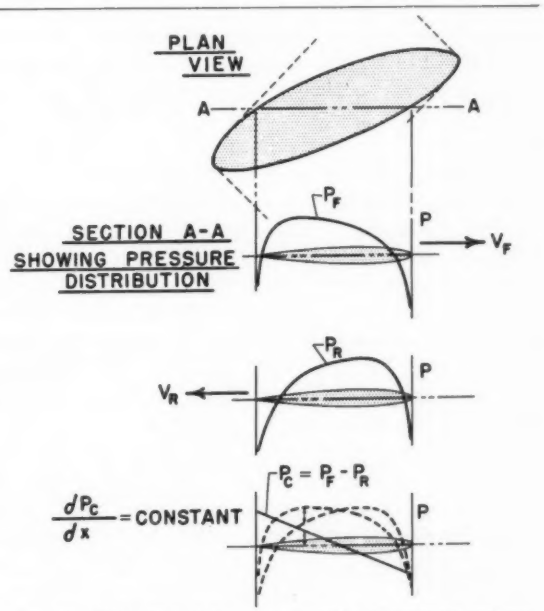

FIG. 4. Condition for minimum drag with a given total volume

drag, therefore, the thickness must be distributed in such a way that the drag per unit volume is constant over the entire wing in the combined flow field. The significance of this condition in terms of the pressure distributions on an oblique airfoil in supersonic motion is illustrated in Fig. 4.

Examples of bodies satisfying this condition are not difficult to find. One example is that of a thin, flattened ellipsoid accelerating in an incompressible fluid. The drag force in this case is in opposition to the acceleration of the motion and, hence, is attributed to a "virtual additional mass" of the body. The surface pressures due to the acceleration are proportional to $\partial\varphi/\partial t$, where φ is the surface potential. As is well known, the surface potential of any ellipsoid moving in a direction x parallel to a principal axis is of the form $\varphi = KVx$, where K is a constant depending on the proportions of the ellipsoid and V is the velocity. In accelerated motion, $\partial\varphi/\partial t$ and, hence, the pressure are also proportional to x, and this is true for motion in either direction except that the pressures are changed in sign. The pressure distribution in the combined flow, therefore, has a constant gradient in the direction of x, and the ellipsoid satisfies the necessary condition for minimum drag with a given volume. In this case the condition is perhaps better stated as the condition for minimum virtual volume with a given actual volume.

Another example is that of a biconvex airfoil of infinite aspect ratio in steady motion at supersonic speeds. If the upper and lower surfaces are parabolic arcs, the Ackeret theory gives a straight-line distribution of pressure from nose to trailing edge for motion in either direction.

The foregoing method may be readily extended to other problems of minimum drag involving different specifications on the thickness distribution. Perhaps the simplest of these is the case in which the thickness of the wing is specified along some line such as A–B in Fig. 5. Over the remainder of the wing plan form the thickness is to be distributed so as to achieve the minimum drag under the specified conditions.

In this example we wish to consider variations in the thickness distribution which do not alter the shape of the cross section A–B. Any small element of slope having the strength m_1, as in Fig. 5, must therefore be followed by an equal opposite element m_2 at some downstream position ahead of the line A–B so that the thickness along the line A–B is not changed. The two equations determining the necessary condition on the pressure distribution are:

(1) *For no change in thickness along A–B:*

$$m_1 + m_2 = 0$$

(2) *For no change in drag:* $m_1 P_{c1} + m_2 P_{c2} = 0$

and these lead to the relation

$$P_{c1} = P_{c2}$$

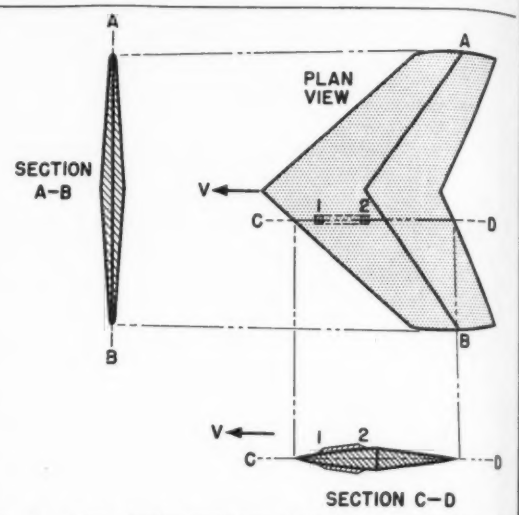

FIG. 5. Wing showing variation of thickness distribution with fixed section A–B.

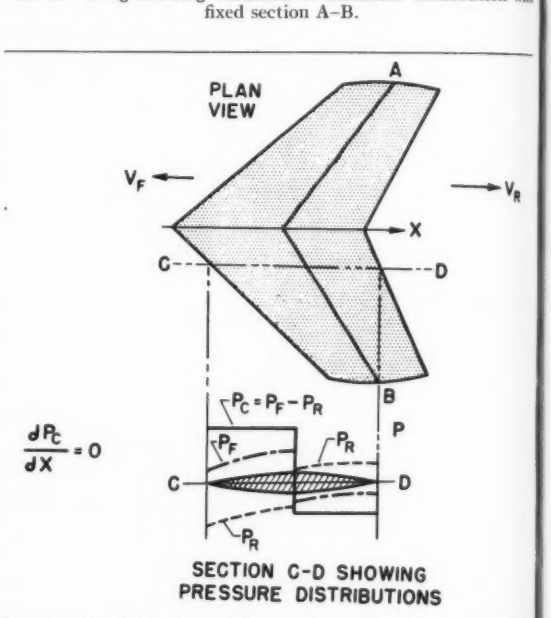

FIG. 6. Condition for minimum drag with given maximum thickness.

Hence, the pressure must not vary in the streamwise direction at points ahead of the section A–B. If the airfoil is further required to close along the trailing edge, a similar condition will be imposed on the pressures in the region behind the line A–B (see Fig. 6).

It will be noted that the condition for minimum drag does not impose a restriction on the spanwise variation of the pressure and that this variation will presumably be determined by the given shape of the section A–B. If the shape of the section A–B is not given exactly but is merely required to have a certain frontal area, then it is found that the pressure in the combined flow field must have the same constant value at all points ahead of this section. The existence of a constant pres-

sure means that the drag per unit of frontal area is constant.

It is interesting to note that the condition for minimum drag with a given frontal area requires that the drag per unit frontal area be constant over the entire wing, while the condition for minimum drag with a given volume requires a constant drag per unit volume. If the maximum thickness of each streamwise section is specified, then the drag per unit thickness must be constant over each section.

Minimum Drag for a Given Lift

The foregoing principles of calculation can be carried over without essential modification to the problem of lift distribution. The drag arising from the lift can be calculated independently of the thickness; hence, the wing can be considered a "lifting surface" slightly cambered or twisted in such a way as to support the desired distribution of lift. A given distribution of lift will induce a certain downwash velocity, and the resultant inclination of the stream lines must agree with the slope of the lifting surface at all points. The drag of the lifting surface will be computed by integrating the product of the local lift by the local inclination of the lifting surface.

The fact that a given distribution of lift has the same drag for either direction of motion can be seen by considering the mutual drags of a pair of lifting elements. Each element of lift produces a distribution of downwash over the plane. The actual configuration of the downwash field does not need to be specified, but its value at all points is assumed to be proportional to the lift of the element. Hence the downwash of an element l_1 at the position of another element l_2 may be expressed in the form $w_{21} = l_1 W_{21}$, where W_{21} is an influence function that depends on the geometric position of element 2 in relation to element 1. The drag of element 2 caused by element 1 is, therefore, $l_1 W_{21} l_2$.

In reversed motion the roles of the elements are reversed and the drag of element 1 caused by element 2 is now $l_2 W_{12} l_1$ and $W_{12} = W_{21}$. Similarly, the drag of element 2 caused by element 1 in reversed motion is equal to the drag of l_1 caused by l_2 in forward motion. These statements do not exclude the possibility that each element lies wholly or partially outside the zone of influence of the other element, and, hence, the reversal principle holds for unsteady or supersonic motions.

Suppose a plan form and a distribution of lift are given, and consider again the field of perturbation velocities obtained by superimposing the fields in forward motion and in reversed motion. The horizontal perturbation velocities that give rise to the lift will be exactly canceled at each point of the surface. However, the downwash velocities over the surface will not, in general, be canceled, and the drag of the given distribution of lift for either direction of motion can be computed by considering this lift to act in the combined downwash field.

If consideration is restricted to the method of calculating drag by combining the flow fields in forward and reversed motion, it is easily seen that the mutual interference drags of any two lifting areas are equal. The drag of a lifting surface A caused by the downwash of lifting surface B is exactly equal to the drag of B caused by the downwash field of A. This theorem follows from the symmetry of the combined flow field of any element and the equality of interference drags of two elements exactly as was previously demonstrated in the case of thickness.

Consider now a lifting surface supporting a given lift L, and suppose that a distribution of lift over the plan form designed to achieve the minimum drag under the stated conditions is given. Any small variation in the shape of the lift distribution which meets the condition of constant total lift can be divided into pairs of elements of equal, opposite lifts. If the drag added by every such pair of elements is zero, then the drag added by any small continuous distribution of the required type will also be zero.

Considering two such elements of a small additional distribution of lift, it is seen that the drag added to the original distribution will again consist of three parts: (1) the drag of the elements alone; (2) the drag added to the original distribution by the downwash fields of the elements; and (3) the drag of the elements in the downwash field of the original distribution. The drag of the elements alone will be of second order but will always be positive so that the second-order variation in drag is positive. Items (2) and (3) will be equal by virtue of the equality of mutual interference drags. For the first-order variation in drag, therefore, we need only consider the elements of lift acting in the downwash of the original distribution. Since the elements of lift are equal and opposite, their drags will be equal and opposite, and the added drag will be zero if the downwash is the same at each element. For all such pairs to contribute zero drag, the downwash must be constant over the whole wing. Hence, for minimum drag the lift must be distributed over the wing in such a way that the downwash in the combined flow field is constant at all points of the plan form. The condition is illustrated in Fig. 7.

Examples of the Minimum Drag of Lifting Surfaces

The stated condition for minimum drag with a given total lift obviously includes the well-known condition for minimum induced drag in steady flight at subsonic speeds.[4] In that case the combined flow field is nothing more or less than the two-dimensional field of motion induced by the vortex wake that is normally trailing but which now extends to infinity both ahead of and behind the wing. The elliptic span loading, which

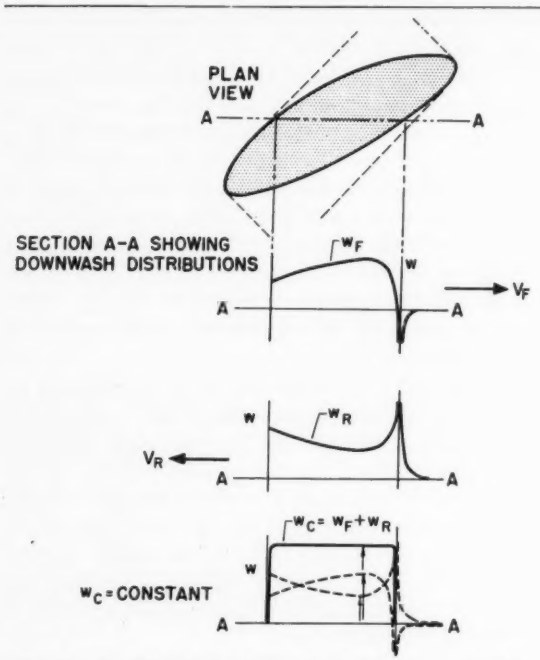

FIG. 7. Condition for minimum drag with a given total lift.

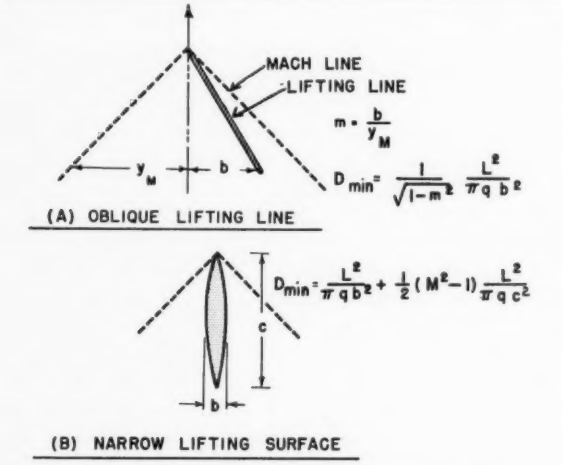

FIG. 8. Examples of minimum drag for a given lift.

yields the minimum drag in this case, produces a uniform downwash not only over the plan form of the wing but over the whole infinite vortex ribbon as well.

In addition to providing the conditions for minimum drag, the combined flow field also provides a simplification of the actual computation of the drag in specific cases. Thus, in the case of steady motion at subsonic speeds, the superposition of the forward and reversed disturbance fields, which are three-dimensional, results in a two-dimensional field of motion. In supersonic motion, the combined field retains its three-dimensional character, but the integration for the downwash is nevertheless considerably simplified when the forward and reversed fields are considered simultaneously.

In the supersonic case, the computation of downwash over the surface involves the superposition of lifting elements whose individual disturbance fields are represented by the potential of an elementary horseshoe vortex that has the form[2, 5]

$$\varphi = \frac{\Gamma\, dy}{2\pi} \frac{xz}{(y^2 + z^2)\sqrt{x^2 - y^2 - z^2}}$$

for an element of lift $\Gamma\rho V\, dy$ located at the origin. The downwash at the position x_2, y_2, z_2 near the plane $z = 0$ arising from an element of lift at the position x_1, y_1 is obtained by differentiating φ with respect to z near $z = 0$ and introducing the displaced origin

$$w_{21} = \frac{\Gamma_1\, dy_1}{2\pi} \times \frac{(x_2 - x_1)}{[(y_2 - y_1)^2 + z_2^2]\sqrt{(x_2 - x_1)^2 - (y_2 - y_1)^2 - z_2^2}}$$

Normally, the computation of downwash over the lifting surface requires that the range of integration be limited to a portion of the plan form so as to exclude the forward branches of the Mach cones, where there is no real disturbance. In the combined flow field, however, both branches of the cones are to be included, and the integration for the downwash at each point can be extended over the entire plan form provided the sign of the radical in the equation is chosen so that the downwash of the lifting element has the same sign in both branches of the cone.

One example that lends itself to calculation is that of an extremely long narrow wing or "lifting line" at an angle of yaw such that the line lies inside the Mach cone originating from its forward tip (see Fig. 8). Here the integration for the downwash in the combined flow field extends from one end of the line to the other, as in the subsonic case, and it is found that an elliptic distribution of lift results in a uniform downwash, yielding the value

$$D = \left(1/\sqrt{1 - m^2}\right)(L^2/\pi q b^2)$$

for the minimum drag. Here, the quantity m is the ratio of the slope of the lifting line to the slope of a Mach line and is less than 1.0 when the crosswise component of velocity of the lifting line is subsonic. As the angle of yaw is decreased so that the lifting line approaches the Mach cone, the drag of this distribution of lift approaches infinity, a fact that must be taken to mean that the concentration of a finite amount of lift within an extremely narrow chordwise dimension is not permissible when the crosswise velocity component is near sonic velocity or is supersonic.

For a lifting surface of narrow proportions lying near the center of the Mach cone, it is found that the expression for the drag can be separated into two components,

one of which depends on the lengthwise distribution of lift while the other depends on the spanwise loading. The minimum value in this case is found to be

$$D = \frac{L^2}{\pi q b^2} + \frac{1}{2}(M^2 - 1)\frac{L^2}{\pi q c^2}$$

where b is the overall span of the wing and c is the overall length. The minimum value of the drag is achieved when both the spanwise and the lengthwise loadings are elliptical.

Determination of Optimum Plan Form

In practice, the determination of the best distribution of lift or thickness for a given plan form may not be so important as the problem of determining the best shape for the plan form. Unfortunately, it is difficult to formulate the latter problem in such a way as to lead to a single definite solution that will be generally useful. The foregoing analysis does, however, provide one important principle concerning wings of minimum drag. Such wings will be characterized by the fact that the drag is stationary not only with respect to variations in the lift or thickness distribution but also with respect to variations in the shape of the outline. Suppose the plan form of such a wing, together with the distribution of lift or thickness satisfying the desired condition for minimum drag, is given. If the drag is to remain unchanged when the outline of the wing is displaced through a small distance, then the distribution of pressure or downwash corresponding to a minimum drag not only must appear over the plan form itself but must also extend for a small distance, without first-order variation, away from the edge of the plan form.

That the foregoing condition leads to a stationary value of the drag can be seen by considering the effect of a small displacement of the outline of a lifting wing, as illustrated in Fig. 9. Supposing the total lifts of the original and the distorted wings to be the same, lift must be removed from the original area and placed on the added area. The first-order variation in drag can again be computed by considering only the effect of the original downwash field on the added distribution of lift. If this downwash, which was required to have a constant value at all points of the original plan form, remains constant in the regions of the added area, then a redistribution of lift from the original to the added area will not affect the total drag.

Curves of variation of the drag with plan-form coefficients seldom show local maxima or minima but show, more often, a monotonic character. As an example

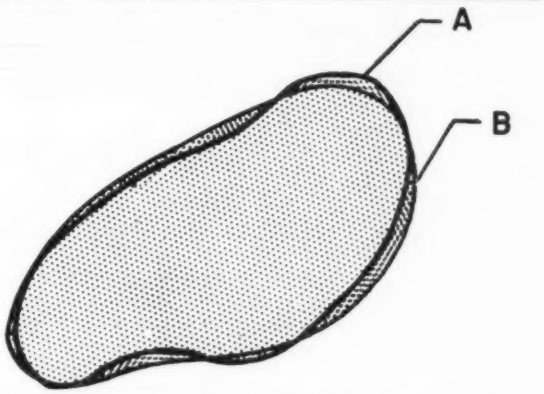

Fig. 9. Condition for drag to be a minimum with respect to variations in plan form.

we may consider the induced drag of wings at subsonic speed. Here, the combined flow field, as previously noted, is simply the two-dimensional motion induced by the vortex wake, and, in the case of minimum drag, the downwash is constant over the whole wake extending ahead of and behind the wing. Since the condition for minimum drag persists along the whole wake, the drag is unaltered by any displacement of the wing boundary in the chordwise direction parallel to the wake. If one proceeds beyond the tip of the wing, however, the downwash changes sign abruptly, and large values of upwash are encountered. The drag is thus not a minimum with respect to changes in the span of the wing but can be continually diminished by removing area from the center portions of the wing and placing it at the tips. At supersonic speeds, the minimum drag for a given area and lift occurs when the wing surface is disposed along narrow lines lying near the center of the Mach cone and having the greatest possible length and span.

References

[1] Hayes, Wallace D., *Linearized Supersonic Flow*, Rep. No. AL-222, North American Aviation, Inc., Los Angeles, June 18, 1947.

[2] von Kármán, Th., *Supersonic Aerodynamics—Principles and Applications*, Journal of the Aeronautical Sciences, Vol. 14, No. 7, pp. 373–409, July, 1947.

[3] Munk, M. M., *The Reversal Theorem of Linearized Supersonic Airfoil Theory*, Jour. Applied Physics, Vol. 21, No. 2, pp. 159–161, February, 1950.

[4] Munk, Max M., *The Minimum Induced Drag of Aerofoils*, N.A.C.A. Report No. 121, 1921.

[5] Heaslet, Max. A., Lomax, Harvard, and Jones, Arthur L., *Volterra's Solution of the Wave Equation as Applied to Three-Dimensional Airfoil Problems*, N.A.C.A. Report No. 889, 1947.

Design and Performance of a Simple Interferometer for Wind-Tunnel Measurements

HARRY I. ASHKENAS* AND ARTHUR E. BRYSON†
California Institute of Technology

ABSTRACT

The design of an interferometer with a 3½-in. diameter light field and its application to a continuously operating 4- by 10-in. supersonic wind tunnel are discussed. The main features of this interferometer are (1) its extremely low cost compared to previous designs; (2) its light weight and flexibility; (3) its simplicity, permitting the instrument to be used also as a schlieren system; and (4) its unique feature of passing both light beams through the test section to minimize the effect of the side-wall boundary layers in the interferograms.

INTRODUCTION

DURING THE PAST FEW YEARS, the Mach-Zehnder interferometer has come into increased use throughout this country for investigating high-speed aerodynamic phenomena. Ladenburg and his coworkers at Princeton University have been particularly active in this field.[1–7] The main attraction of the instrument for the aerodynamicist is its ability to provide quantitative data on the density distribution for the complete flow field under investigation without the necessity of inserting probes into the flow (which introduce changes in the flow and require many measurements to describe the complete flow field). The bibliography at the end of this paper lists references giving ample information on the optical theory of the instrument and describing its application to the study of two-dimensional and axially symmetric flow fields.

In the course of work on boundary-layer-shock-wave interaction at GALCIT,‡ it became apparent that an interferometer could be used to great advantage. However, the location and physical setup of the GALCIT 4- by 10-in. Transonic Wind Tunnel are highly unfavorable for the use of an interferometer according to standard concepts: The tunnel is continuously operating, the test section being directly above two 300-hp. centrifugal blowers; the power plant of the GALCIT 10-ft. Wind Tunnel is close to the test section room; and the floor of the test section room is of temporary wood construction. Thus, the vibration and noise levels near the test section are unusually high. The main problem, therefore, in the design of the interferometer was to obtain proper vibration isolation. Furthermore, it was required that the interferometer be mounted and removed easily to make room for other setups (such as schlieren) and also to make possible easy changes to the test section. (For details of the wind tunnel see references 43 and 44.) The tunnel has a flexible nozzle and variable second throat permitting operation from $M = 0.7$ to 1.5.

The instrument developed is comparatively simple and has proved to be adequate. It is believed that a description of the design and installation of the interferometer will be useful, since similar problems will probably arise with other wind tunnels.

The instrument was designed and built during the course of an investigation that was begun under Air Force sponsorship but which, for the past year, has been carried out under the sponsorship of the National Advisory Committee for Aeronautics.

The authors wish to thank Dr. Hans-Wolfgang Liepmann, who started them on the design and whose idea it was to put both light beams through the test section. They also wish to thank Satish Dhawan, who suggested and designed the schlieren attachment to the instrument.

DIFFERENCES FROM PREVIOUS INTERFEROMETERS

The principal innovations of this interferometer are believed to be (1) its low cost, (2) its light weight and simplicity of construction, (3) its simple attachment for taking schlieren pictures, and (4) its feature of passing both light beams through the test section.

Table 1 contains an itemized cost estimate for the interferometer. It should be noted that the cost of reproducing the instrument now would be considerably less, mainly because of the elimination of the engineering time.

A rather thick boundary layer exists on the test-section windows so that, if only one beam traversed the test section, a large error would be introduced because of the fact that the interferometer integrates the value of density through the flow. Most of the previous interferometers put one beam through the flow being investigated and the other beam through a glass-paneled compensating chamber in which the air density

Received June 12, 1950.

* Graduate Assistant. Now at Cornell University.

† Graduate Assistant.

‡ Guggenheim Aeronautical Laboratory, California Institute of Technology.

can be adjusted to approximately the free-stream density of the flow. In this interferometer, both beams traverse the test section, one passing through the flow being investigated and the other passing through the test section $7^3/_4$ in. ahead of that beam. The boundary layer does not change its thickness appreciably in the distance between the two beams, so that both beams traverse effectively the same boundary layers and the latters' effects are thus canceled. At the same time, the flow in the front beam corresponds to an "automatic compensating chamber" providing free-stream density as the basis for the fringe shifts. This is particularly applicable to supersonic flow where the flow ahead of the disturbance is uniform, but it can also be used for subsonic flows where the effect felt ahead of the model is small.

TABLE 1
Cost of the GALCIT Interferometer

Plane-parallel plates	$2,000.00
Mirror frames	75.00
Turning motors	50.00
Light source	50.00
Filter	30.00
Lens	18.00
Spherical mirror	27.50
Paraboloidal mirror	100.00
Shutter	40.00
Camera back	18.00
Suspension frame	34.00
Optical bench	25.00
Two test-section windows	13.00
Traversing table, switch box, mirror cells, rails, suspension clamps, etc.—shop labor	1,500.00
Temporary setup	40.00
Engineering time	2,000.00
Total	$6,020.50

OVERALL DESCRIPTION OF THE INTERFEROMETER

(1) *Optical Path*

A schematic diagram of the optical path through the instrument is shown in Fig. 1. Light from a mercury vapor lamp is passed through a filter and focused by a lens on a small mirror that is at 45° to the incident beam; this small mirror is also at the focus of a parabolic mirror causing the reflected light to be parallel. This parallel beam is passed back over the small mirror (which shows up as a slight shadow on the interferograms but does not interfere at all in their evaluations) and is then split at the half-silvered mirror No. 1 into two beams; one beam passes through mirror No. 1, reflects off the fully silvered mirror No. 3, then passes through the test section ahead of the model; the other beam reflects from mirror No. 1, passes through the test section over the model, then reflects from the fully silvered mirror No. 2. The two beams are recombined at the half-silvered mirror No. 4 and are brought to a focus by a spherical mirror on a ground-glass screen. The plane mirrors are at the corners of a $7^3/_4$- by $35^3/_4$-in. rectangle, the plane of the rectangle being horizontal. The light beams are circular and can be varied in diameter from 2 in. to $3^1/_2$ in. by varying the position of the lens. Both beams pass through the 12-in. diameter test section windows that are made of good quality plate glass of 1-in. thickness. (The use of plate glass instead of high-quality plane-parallel optical glass provides a substantial reduction in cost; it was found that there was no need for the latter.) The instrument can be traversed forward and backward, as well as up and down, so that the small field of view is not a disadvantage. Actually, most of the phenomena studied are local flow phenomena that are adequately covered by the $3^1/_2$-in. diameter light field. Other test-section-

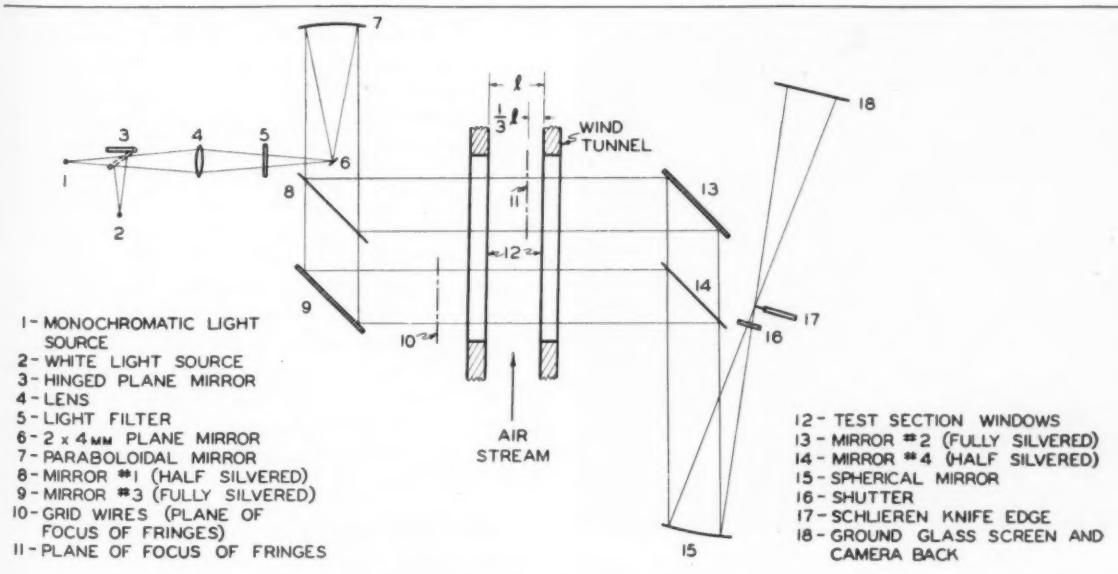
1 - MONOCHROMATIC LIGHT SOURCE
2 - WHITE LIGHT SOURCE
3 - HINGED PLANE MIRROR
4 - LENS
5 - LIGHT FILTER
6 - 2 x 4 MM PLANE MIRROR
7 - PARABOLOIDAL MIRROR
8 - MIRROR #1 (HALF SILVERED)
9 - MIRROR #3 (FULLY SILVERED)
10 - GRID WIRES (PLANE OF FOCUS OF FRINGES)
11 - PLANE OF FOCUS OF FRINGES
12 - TEST SECTION WINDOWS
13 - MIRROR #2 (FULLY SILVERED)
14 - MIRROR #4 (HALF SILVERED)
15 - SPHERICAL MIRROR
16 - SHUTTER
17 - SCHLIEREN KNIFE EDGE
18 - GROUND GLASS SCREEN AND CAMERA BACK
WIND TUNNEL
AIR STREAM

FIG. 1. Schematic diagram of optical path.

window arrangements for studying various types of flows are being designed.

(2) *Light Source*

The interferometer has been designed with a minimum of air-glass interfaces to prevent loss of light, there being only four such surfaces—two at the lens, and two at the filter. These surfaces are coated to prevent further loss of light. As a result of this design, a 100-watt mercury light can be used, and, in conjunction with the filter, it gives sufficient monochromatic light for pictures to be taken at 1/800 sec. (Figs. 5 to 8 were taken with this light source at exposures of 1/400 or 1/800 sec.)

(3) *Mounting*

The four plane mirrors, the light source, the paraboloidal mirror, and the spherical mirror are mounted on a wooden box that is suspended from a welded-pipe framework by four sets of eight rubber bands each. The box with all the equipment mounted on it weighs only 250 lbs., which is in contrast to all other interferometers that have come to the authors' attention where the mirror base plates have been massive to provide rigidity. Here, the box is allowed to deflect in any manner it chooses, and, once it has assumed its deflected position and the mirrors have been adjusted, the shock mounting of the system effectively prevents any further misalignment from taking place. The action of the rubber bands rubbing over each other provides sufficient damping for the system. The natural frequency of the box is about 1 cycle per sec. This was found to provide not quite enough vibration isolation, and, therefore, the frame has also been isolated by placing 12 in. of foam rubber under each of the four corners. This has provided sufficient vibration isolation to permit one to see the fringes while running the wind tunnel (two 300-hp. centrifugal compressors power the tunnel) and also while the GALCIT 10-ft. Wind Tunnel is running (its 750-hp. motor and fan are near the interferometer). The rubber bands are attached to jackscrews, permitting the box to be traversed in a vertical direction and allowing a fine vertical adjustment to be made in getting the light beam parallel to the surfaces of two-dimensional models. The whole interferometer can be traversed along the test section on four casters; it can also be rotated through small angles on these casters, also allowing a fine horizontal adjustment to be made in getting the light beam parallel to the surfaces of two-dimensional models. The interferometer can also be completely traversed away from the test section and the regular schlieren system traversed into its place. (Although schlieren pictures can be taken with the interferometer as described below, these pictures are not of such high quality as those taken with the regular schlieren system.)

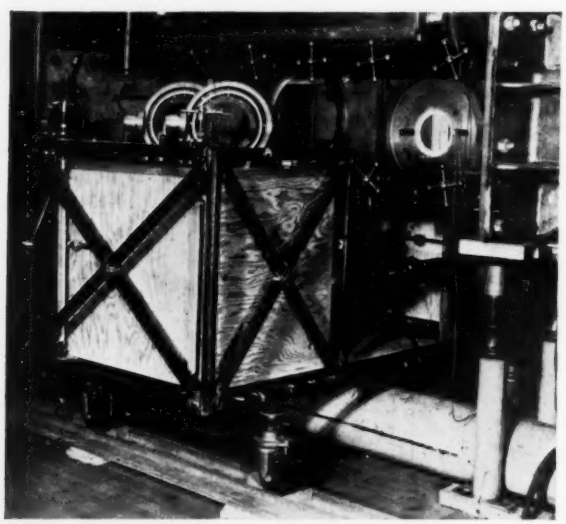

FIG. 2. North half of the interferometer mounted on the GALCIT Transonic Wind Tunnel showing parabolic mirror, plane-parallel mirrors Nos. 1 and 3, and the vibration mounting.

The camera box is mounted on the pipe frame so that putting film holders in the camera does not disturb the instrument's adjustment.

(4) *Adjustments*

The various component parts of the interferometer are fitted with a large number of adjustments. This practice, while giving rise to a large number of possible misalignments, also results in considerable ease in setting up the instrument. Locking devices are present to prevent any change in the final setup.

Detailed Description of Component Parts

(1) *Monochromatic Light Source*

The monochromatic light source is a mercury vapor lamp, General Electric Type AH-4, housed in a Cenco No. 87269 lamp housing. The lamp house is attached to a brass tube that contains a Bausch & Lomb achromatic coated lens of 142.9-mm. focal length and 46.0-mm. diameter. The brass tube also contains a receptacle for a Wratten No. 77A filter, which filters out the green line at 5,461Å. in the mercury spectrum. Attached to the top of the brass tube is a U-frame that supports a rectangular frame on which a small diameter wire is mounted carrying the 2- by 4-mm. first-surface plane mirror that acts as a secondary light source since it is at the focus of a $5^1/_2$-in. diameter, 15-in. focal length paraboloidal mirror. The paraboloidal mirror is mounted in an aluminum mirror cell of the type described by Strong.[21] A central flexure post and four adjusting screws provide the fine adjustment of position, while the course adjustment of position is provided by the sliding tubular mounting that is attached to the interferometer box.

(2) *White Light Source*

A 2- by 2-in. first-surface plane mirror has been mounted on a hinge in the mercury lamp housing and a

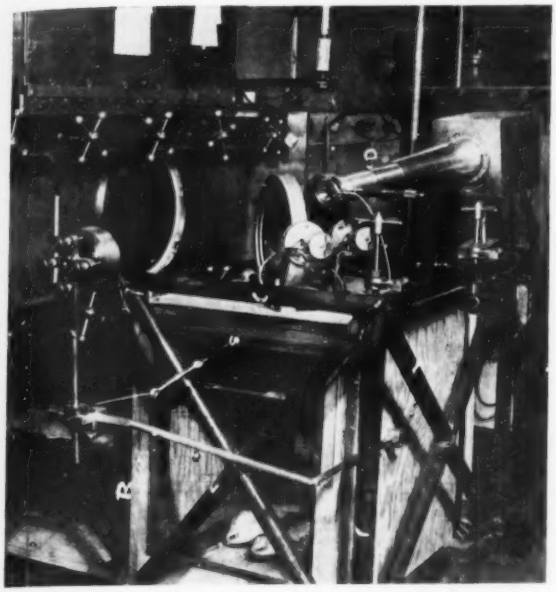

FIG. 3. South half of the interferometer showing the plane-parallel mirrors Nos. 2 and 4, the spherical mirror, the shutter, the micrometer knife edge for schlieren pictures, and the camera.

hole cut out of the housing so that by turning a screw the mirror is brought to a position that is at 45° to the light from a 500-watt motion-picture projector lamp that is mounted adjacent to the lamp housing. This light source is the same distance from the mirror as the mercury light so that both sources are optically at the same point with respect to the lens (see Fig. 1).

(3) *Plane-Parallel Mirrors*

The plane-parallel mirrors are carried in a frame shown in Fig. 4. Each mirror itself is held in a split brass ring by means of a soft rubber, full-circumference support. Two gimbals allow rotation of the mirror about a horizontal and vertical axis. Rotation of the gimbals is obtained by means of remotely controlled, reversible electric clock motors. The output shaft of these motors (Haydon No. 3200) makes one revolution per 8 days, resulting in an extremely fine control of the angular displacements of the mirrors. The gearbox on the motor is equipped with stamped metal gears, and a not inconsiderable amount of backlash is present; hence, a simple torsion spring is placed at each bearing to supply a backlash-eliminating force.

The frames of all four mirrors are identical. Duralumin castings are used for the outer frame and the inner gimbals. There is no provision for coarse angular adjustment of the mirrors, which makes the initial adjustment somewhat tedious but thereafter no coarse adjustment is needed. Mirror Nos. 1, 2, and 3 (see Figs. 2 and 3) are bolted to the top of the plywood box. Mirror No. 4 is mounted on a traversing table to provide the adjustment for equalizing the optical path lengths of the two arms of the interferometer. The traversing mechanism features a Le Blond lathe bed type way; a traversing screw of 1-mm. pitch, driven by a hand-operated 50:1 worm-gear reduction unit; a simple nut; and a pin-driven gravity-emplaced traversing table.

(4) *Camera and Schlieren System*

The photographic components consist of a $3^1/_2$-in. diameter, 24-in. focal length spherical mirror, Eastman Synchro-Rapid 800 shutter (speeds up to 1/800 sec.), and a 4- by 5-in. Graphic camera back with a ground-glass viewing screen. Because of the shutter's small diameter, it has been placed at the end of a truncated conical piece extending from the camera box (see Fig. 3). The focal point of the light beam reflected from the spherical mirror is just inside the shutter in the conical part of the camera, and a micrometer with a razor blade mounted on its end is placed there as the knife edge of a schlieren system. The knife edge can be traversed along the light beam to obtain best sensitivity, and it can be rotated to give "knife-edge horizontal" and "knife-edge vertical" pictures. To take schlieren pictures, the forward light beam of the interferometer is blocked out, the filter is removed, and the white light source is used.

The film used is Ansco Triple-S-Pan, which is sufficiently fast to take good pictures at 1/400 sec. Slightly better pictures are obtained using Eastman 103-G spectroscopic plates, which are especially sensitive in the green range containing the wave length of the monochromatic light used (5461Å.). These plates are fast enough for pictures at 1/800 sec. and have the added advantage that there is no film shrinkage that could cause errors in fringe shift measurement. (Actually, by com-

FIG. 4. Close-up of plane-parallel mirror frame showing gimbals and rotating motors.

paring the film and the glass plates, no significant errors in fringe shift measurement have been found.)

Performance of the Interferometer

(1) *Initial Adjustment*

The initial adjustment of the interferometer was made using the pentaprism method as described in reference 30. This adjustment required several days to perform because of the slow mirror movements, but, once completed, it does not have to be done again.

(2) *Daily Adjustment*

Because of slight deflections of the box caused by temperature and humidity changes, the interferometer gets slightly out of adjustment from day to day. However, with an experienced operator, fringes of the desired spacing and orientation can be focused on the ground-glass screen in less than 10 min. using the "near-and-far cross-hair" method of adjustment described in reference 30. For this, an auxiliary plane mirror is placed at 45° to the light beam just ahead of the spherical mirror, and an autocollimating telescope is placed in the reflected beam from this mirror. If the telescope has been previously focused on a distant object, it will now focus on the two images of the secondary light source (the 2- by 4-mm. mirror) if the light is parallel. These images serve as the "far cross-hairs" being optically at infinity; the "near cross-hairs" are the shadows of this 2- by 4-mm. mirror, which is only a few inches from the half-silvered mirror No. 1. Now, focusing on the "far cross-hairs," mirror No. 1 is rotated about its vertical and horizontal axes until the two images coincide; then, focusing on the "near cross-hairs," mirror No. 4 is rotated about its horizontal and vertical axes until these two images coincide. This latter adjustment slightly disturbs the previous adjustment of mirror No. 1, which is then done over again, and, similarly then, mirror No. 4 is readjusted. This process is rapidly convergent, usually requiring only the first adjustment of each mirror.

(3) *Horizontal or Vertical Fringes*

The geometry of this particular interferometer is such that by now rotating both mirror No. 1 and mirror No. 4 in the same direction about horizontal (or vertical) axes in a ratio of 7 to 5, horizontal (or vertical) fringes appear very nearly in the plane of the ground-glass screen. The spherical mirror is rotated slightly, placing the reflected beam outside the camera so that a white card can be placed in the beam to determine the plane in which the fringes are focused. By reference to the "linear interferometer representation" described in reference 34, the operator can then tell which way to rotate mirror Nos. 1 and 4 to focus the fringes precisely on the ground-glass screen with the desired spacing and orientation. Previously, the spherical mirror has been located so as to focus a plane that is one-third of the way from the exit window to the entrance window on the ground-glass screen. This minimizes refraction errors in the interferogram.[7] Thus, both model and fringes are in focus on the ground-glass screen.

(4) *Equalizing Optical Path Lengths*

The next adjustment is to equalize the optical path lengths in the two legs of the interferometer. This is done by placing an auxiliary mirror in front of the paraboloidal mirror so that it cuts out half of the monochromatic light beam. An auxiliary white light source is then reflected onto this auxiliary mirror so that its light travels the same circuit as the monochromatic light. The image formed near the ground-glass screen is then half monochromatic light fringes and half white light field. Mirror No. 4 is then traversed until the white light fringes appear in the white light field; usually only a few turns of the traversing wheel are required, and often the white light fringes have not "strayed" since the last use of the interferometer. The correct direction to traverse is easily checked by the fact that monochromatic fringes should get more "contrasty" if the traversing is done in the correct direction.

(5) *Eliminating "Twist"*

The next adjustment is to eliminate "twist" from the beam—i.e., to place the two images directly above each other (for the case of horizontal fringes). This gives the maximum contrast in the fringes. This can be done by rotating mirror Nos. 1 and 4 about their vertical axes slightly (for the case of horizontal fringes) until the monochromatic fringes are parallel to the white light fringes and they are both horizontal. This adjustment works only if divergent white light is used in the auxiliary beam. Getting rid of "twist" can also be done by trial and error without the white light by simply rotating about the vertical axes (as above) until the fringes appear to have maximum contrast.

(6) *Infinite Fringe Adjustment*

The infinite fringe adjustment is obtained by first making the adjustment above for either vertical or horizontal fringes and then slowly increasing the fringe spacing keeping the fringes focused on the ground-glass screen (this is easily done by rotating mirror Nos. 1 and 4 in the same direction in a ratio of 7 to 5).

(7) *Aligning Light Beam to Models*

The final adjustment is to align the light beam to the surface of two-dimensional models or, in the case of axially symmetric models, to align the light beam perpendicular to the axis of symmetry.

(8) *Procedure During a Run*

Before the tunnel is turned on, an undisturbed fringe picture is taken. Then, after the flow has been turned

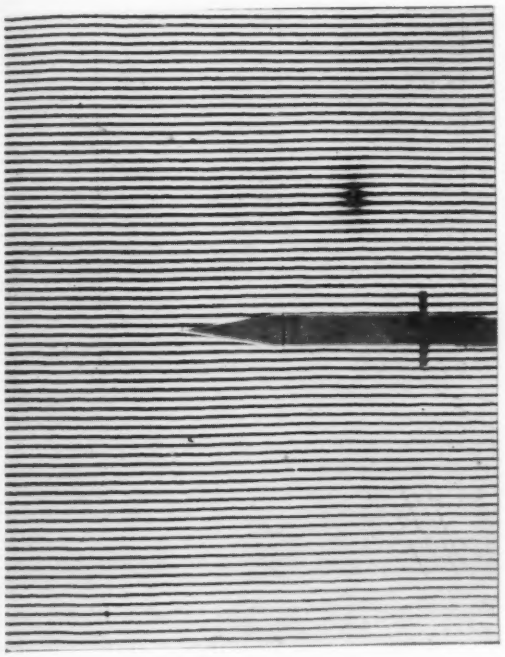

FIG. 5. Undisturbed horizontal fringes.

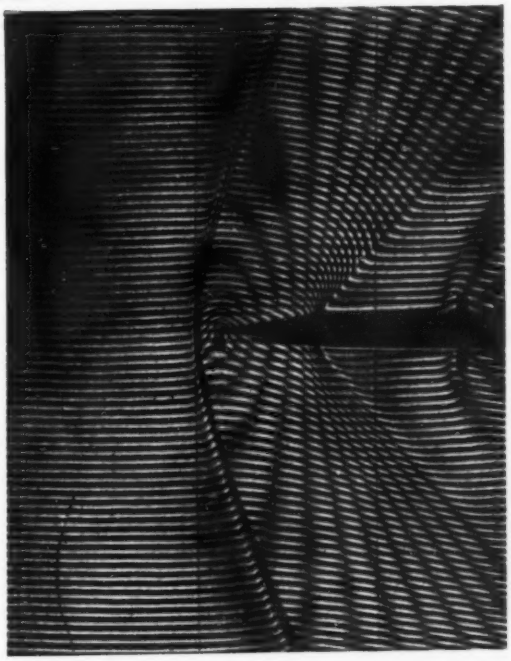

FIG. 7. Lines of constant air density made by superimposing a positive of Fig. 5 and a negative of Fig. 6.

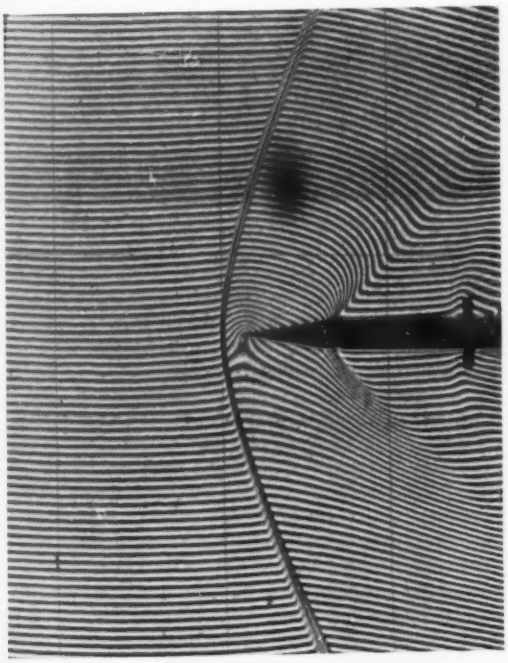

FIG. 6. Horizontal fringe picture of a 10° semiangle wedge at $M = 1.28$.

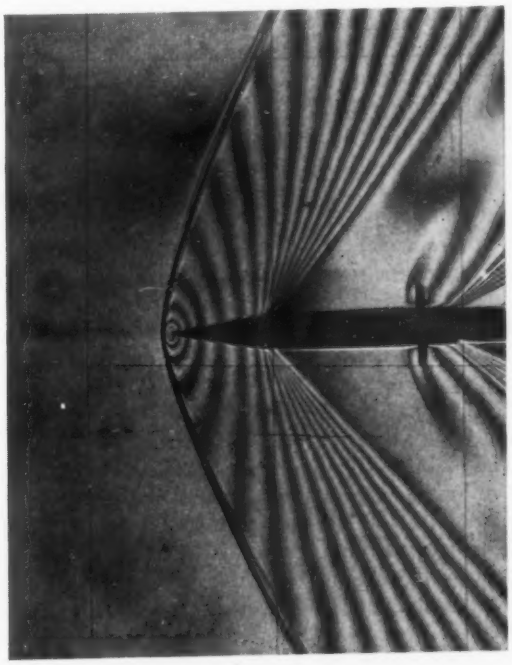

FIG. 8. Lines of constant density by the method of the infinite fringe.

on and has reached an equilibrium flow condition, the monochromatic fringe pictures are taken. While still running, the filter is removed, the mirror in the lamp housing is rotated into place, and the white light then becomes the light source. The white light fringe picture is then taken. Next, the front beam of the interferometer is blocked out and the schlieren system is adjusted; then, a schlieren picture is taken. A shadowgram can also be taken at this point, if desired, simply by moving the knife edge back out of the beam. All of these operations can be performed in a few minutes so that a minimum of tunnel time is used for each run.

(9) *Evaluation of Interferograms*

Knowing the stagnation temperature and pressure in the settling chamber and the Mach Number in the test section, the density of the air in the front beam is readily calculated by the isentropic flow relations. If, in addition, we know the span of the model, the wave length of the light used, and the Gladstone-Dale constant for this wave length, the interferogram can then be completely evaluated to give the density distribution throughout the entire flow field about the model.

For two-dimensional flows, the evaluation is particularly simple, since the density change is directly proportional to the distance the fringes shift from their undisturbed positions. By comparing the fringe pictures taken with and without flow, this fringe shift can be determined. A particularly simple way of doing this, mentioned in reference 18, is to superimpose the negatives of these two pictures; faint lines then appear which are lines of constant fringe shift. Since the negatives are small, this cannot be done too accurately if the fringe spacing is narrow. To overcome this difficulty, enlarged transparencies of the undisturbed fringe pictures are made. Placing this transparency on the enlarger table, the other picture is focused until the two pictures "line up"—i.e., the fringes ahead of the shock wave fall on top of each other. Then, the printing paper is put under the transparency and a picture is printed, giving the lines of constant fringe shift as shown in Fig. 7. To determine the proper number of fringe shifts associated with each line, the white light picture must be used to trace the central fringe through the shock wave, or the fringe shift at a pressure tap on the model is calculated.

The infinite fringe picture serves as a check on the above method, but its accuracy is dependent on the accuracy with which the mirrors were made; therefore, it is usually only accurate (for this interferometer) within $\pm 1/2$ fringe shifts. The method of finite fringes above "calibrates out" the inaccuracies of the optical system.

The evaluation for axially symmetric flows is described in reference 1; it is considerably more difficult and tedious than the evaluation for two-dimensional flows, since the fringe shift is related to the density change by an Abel integral equation.

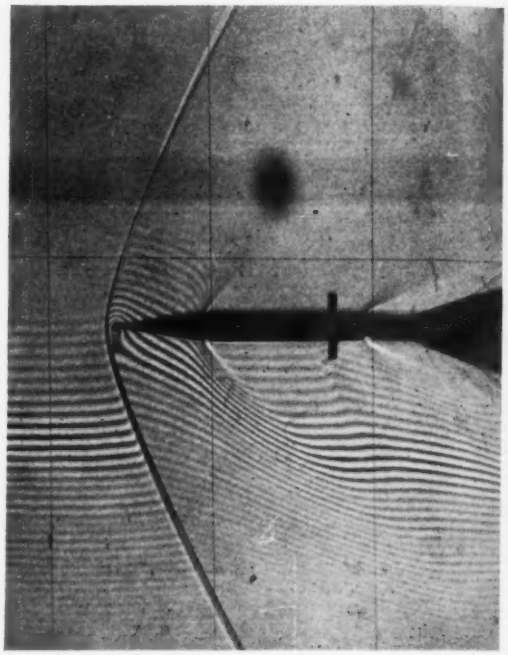

FIG. 9. White light picture showing how fringes may be traced through a shock wave.

(10). *Obtaining Two-Dimensional Flows*

One difficulty in the use of the interferometer for two-dimensional flows is that two-dimensional flows are difficult, if not impossible, to obtain, and, consequently, errors are introduced into the interferogram. As previously described, passing both beams through the test section is a help in overcoming this difficulty by minimizing boundary-layer effects. Permitting models to span the tunnel only up to the beginning of the side-wall boundary layers seems to minimize the three-dimensional effects, although this has not been thoroughly checked as yet. The three-dimensional or "tip" effects probably vary considerably with the model being used and with the flow velocity. Also, the interaction of the shock waves with the side-wall boundary layers alters the tip effects and the boundary layers. The tip effects and the shock-wave-boundary-layer interaction effects cannot be separated and must be considered together in determining the accuracy of the interferograms. Preliminary tests on detached shock waves indicate that both boundary-layer and three-dimensional effects are practically eliminated by careful choice of the model span.

CONCLUSION

Figs. 5 to 10 are typical interferograms taken with this instrument. Fig. 5 is an interferogram showing horizontal undisturbed fringes taken through the test-section windows with the wind tunnel turned off. Fig. 6 shows the flow field about a 10° semiangle wedge with a detached shock wave (the pegs on the flat portion fol-

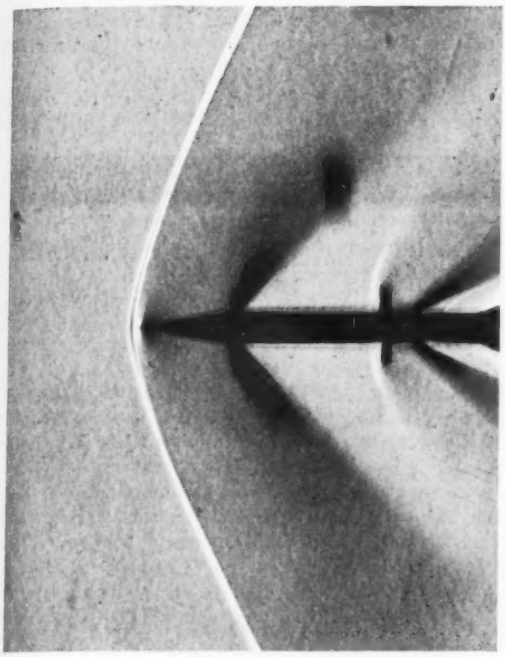

FIG. 10. Schlieren picture made with knife edge mounted on the interferometer.

lowing the wedge are for aid in alignment of the light beam to the leading edge of the wedge.) An investigation of the flow field behind such detached shock waves is at present being carried on using the interferometer. Fig. 7 is an interferogram made by superimposing the negatives of an interferogram with flow and one without flow; the shadowy lines are the lines of $n + {}^1/_2$ fringe shifts (n an integer) and are lines of constant density. Fig. 8 is an interferogram taken with the "infinite fringe," and the dark lines are approximately lines of $n + {}^1/_2$ fringe shifts (n an integer) and are lines of constant density. Fig. 9 is an interferogram taken with white light instead of monochromatic light and shows the manner in which the fringes can be traced through a shock wave. Fig. 10 is a schlieren picture taken with the special attachment to the interferometer described above.

The performance of this interferometer on the GALCIT Transonic Wind Tunnel has proved satisfactory to date, and it is hoped that many interesting aerodynamic phenomena may be studied with it in the future.

REFERENCES

[1] Ladenburg, R., Van Voorhis, C. C., and Winckler, J., *Interferometric Study of Supersonic Phenomena. Part I, A Supersonic Air Jet at 60 lb./in.² Tank Pressure*, Navord Report 69-46, April 17, 1946. *Part II, The Gas Flow Around Various Objects in a Free, Homogeneous Supersonic Air Stream*, Navord Report 93-46, September 2, 1946. *Part III, Boundary Layer and Shock Wave Interactions Observed Along Probes and Wires in Supersonic Air Streams*, Navord Report 7-47, February 19, 1947.

[2] Ladenburg, Panofsky, Van Voorhis, and Winckler, *Study of Shock Waves by Interferometry*, NDRC Report No. A-332, OSRD No. 5204.

[3] Ladenburg, R., *Interferometric Analysis of Supersonic Jets*, Navord Report 74-46.

[4] Winckler, J., *The Mach Interferometer Applied to Studying an Axially Symmetric Supersonic Air Jet*, Review of Scientific Instruments, Vol. 19, No. 5, May, 1948.

[5] Ladenburg, Winckler, J., and Van Voorhis, C. C., *Interferometric Studies of Faster Than Sound Phenomena. Part I, The Gas Flow Around Various Objects in a Free, Homogeneous Supersonic Air Stream*, The Physical Review, Vol. 73, No. 11, June, 1948. *Part II, Analysis of Supersonic Air Jets*, The Physical Review, Vol. 76, No. 5, September 1, 1949.

[6] Bershader, D., *An Interferometric Study of Supersonic Channel Flow*, Review of Scientific Instruments, Vol. 20, No. 4, April, 1949.

[7] Ladenburg, R., and Wachtell, C. P., *Further Interferometric Studies of Boundary Layers Along a Flat Plate*, Palmer Physical Laboratory, Princeton University, December 15, 1949.

[8] Zobel, Th., *Fortschritte in Optischer Strömungsmessung*, Forschungsbericht, 1934.

[9] Zobel, Th., *Verwendung von Lichtinterferenzen in der Technischen Messung.*, Zeitschrift für Vereines Deutschen Ingenieru, Vol. 81, p. 619, 1937.

[10] Zobel, Th., *Development and Construction of an Interferometer for Optical Measurements of Density Fields*, N.A.C.A. T.N. No. 1184.

[11] Zobel, Th., *Strömungsmessung durch Lichtinterferenz*, Forschungsbericht 1167; Translation, N.A.C.A. T.M. No. 1253, August, 1949. (Also Wright Field Air Document Div. T-2 and ATI 26165.)

[12] Hutton, S. P., *The Use of Interferometers in Aerodynamics*, T.N. No. Aero. 1808 (Restricted), Royal Aircraft Establishment.

[13] Groth, E., *Evaluation of Density Fields Around Airfoils in Wind Tunnels by Means of Optical Interference*, N.A.A. Report N.A. 8776, November 21, 1945.

[14] Groth, E., *Measurement of Flow Around the Airfoil by Means of a Mach-Zehnder Interferometer*, January 9, 1946. Joint Intelligence Objectives Agency, Washington, August 21, 1946, BIGS-94 ADG 1011. (Also R. & T. No. 127, January, 1946.)

[15] Groth, E., *Evaluation of Interferometer Measurements of an Airfoil in the 250 × 250 mm. High Speed Tunnel A7*. J 10 A-BIGS-98 AGD 1027, February, 1946. (Also R. & T. No. 128, February, 1946.)

[16] Groth, E., *Evaluation of Density Fields at High Subsonic Velocities by Means of Optical Interference Measurements*, N.A.A. Report N.A. 8783, November 26, 1945.

[17] Groth, E., *Sensitivity and Accuracy of the Interference Method Applied to Pressure Measurements in Wind Tunnels*, ATI-36783, AGD 1042.

[18] Edelman, G. M., *The Design, Development and Testing of Two-Dimensional Sharp Cornered Nozzles*, Meteor Report No. 22.

[19] Gooderum, P. B., Wood, G. P., and Brevoort, M. J., *Investigation with an Interferometer of the Turbulent Mixing of a Free Supersonic Jet*, N.A.C.A. T.N. No. 1857, April, 1949.

[20] Heberle, J. W., Wood, G. P., and Gooderum, P. B., *Data on Shape and Location of Detached Shock Waves on Cones and Spheres*, N.A.C.A. T.N. No. 2000, January, 1950.

[21] Strong, J., *Procedures in Experimental Physics;* Prentice-Hall, New York, 1938.

[22] Zehnder, *Ein Neuer Interferenzrefraktor*, Zeitschrift für Instrumentenkunde, Vol. 11, pp. 275–285, 1891.

[23] Mach, L., *Über ein Interferenzrefraktometer*, Weiner Berichet, Vol. 101, pp. 5–10, 1892; Vol. 102, pp. 1035–1056, 1893.

[24] Mach, L., *Über Einige Verbesserung an Interferenzapparaten*, Wiener Berichte, Vol. 107, pp. 851–859, 1898.

[25] Hansen, G., *Über ein Interferometer Nach Zehnder-Mach*, Zeitschr. f. Tech. Physik, Vol. 12, No. 9, pp. 436–440, 1931.

[26] Kennard, R. B., *An Optical Method for Measuring Temperature Distribution and Convective Heat Transfer*, Bureau of Standards Journal of Research, Vol. 8, pp. 787–805, 1932.

[27] Schardin, H., *Theorie und Anwendung des Mach-Zehnderschen Interferenz-Refraktometers*, Zeitschrift für Instrumentenkunde, Vol. 53, pp. 396, 424, 1933. (R.A.E. Translation No. 79.)

[28] Hansen, G., *Über die Ausrichtung der Spiegel bei einem Interferometer nach Zehnder-Mach*, Zeitschrift für Instrumentenkunde, Vol. 60, p. 325, 1940.

[29] Lamla, E., *Concerning the Light Path in a Mach-Zehnder Interferometer*, Jahrbuch 1941 der Deutschen Luftfahrtforschung, pp. 727–736. (R.A.E. Translation No. 80.)

[30] Lamla, E., *Über die Justierung des Mach-Zehnderschen Interferometer*, Forschungs bericht Nr. 1924, LFA, Braunschweig, December 31, 1943.

[31] Hottenroth, *Über Einige Erfahrungen am Mach-Zehnderschen Interferometer*, Forschungs bericht Nr. 1924, LFA, Braunschweig, December 31, 1943. [Translated Air Doc. Div. T-2, Ame, Wright Field, RC-1081, F-26635 (ATI 26635).]

[32] Clippinger, R. F., *Comparison Between the Jamin-Mach Interferometer and the Williams Interferometer as Applied to the Study of Airflow Around a Supersonic Projectile of Revolution*, Ballistic Research Laboratory, Aberdeen Proving Ground, Report No. 567, September 21, 1945.

[33] Weyl, F. J., *Analytical Methods in Optical Examination of Supersonic Flow*, Navord Report 211-45, December 11, 1945.

[34] Kinder, W., *Theorie des Mach-Zehnder Interferometers und Beschreibung eines Gerätes mit Einspiegeleinstellung*, Optik, Vol. 1, p. 413, 1946.

[35] Winckler, E. H., *Analytical Studies of the Mach-Zehnder Interferometer*, N.O.L. Report No. 1077, December, 1947.

[36] Eckert, E. R. G., Drake, R. M., Jr., and Soehngen, E., *Manufacture of a Zehnder-Mach Interferometer*, U.S.A.A.F. T.R. No. 5721, August, 1948.

[37] Olsen, H. L., *An Interferometric Method of Gas Analysis*, University of Wisconsin, CM-514 NORD 9938, Task Wis-1-I, November, 1948.

[38] Eckert, E. R. G., and Soehngen, E. E., *Studies on Heat Transfer in Laminar Free Convection with the Zehnder-Mach Interferometer*, U.S.A.A.F. T.R. No. 5747, December, 1948.

[39] Winckler, Jordan, *A Mechanical Evaluation Method for Interferometer Photographs*, ATI No. 1964.

[40] Bleakney, W., Weimer, D. K., and Fletcher, C. H., *Shock Tube; A Facility for Investigation in Fluid Mechanics Research*, Review of Scientific Instruments, Vol. 20, No. 11, pp. 807–816, November, 1949.

[41] Johnson, E. R., and Scholes, J. F. M., *A New Interferometer*, Australian Jour. Sci. Research, A, 1, pp. 464–471, December, 1948. (No. 5367 Phys. Abstracts, Vol. 52, No. 622, October, 1949.)

[42] Ashkenas, Harry I., *The Design and Construction of a Mach-Zehnder Interferometer for Use with the GALCIT Transonic Wind Tunnel*, Thesis 1949, California Institute of Technology.

[43] Liepmann, H. W., *The 2" × 20" Transonic Wind Tunnel*, Final Report for Supplement Agreement No. 1 (S-4843) to Contract No. W 33-038 ac-1717 (11592) with A.T.S.C., Wright Field, 1945.

[44] Liepmann, H. W., *The Interaction Between Boundary Layer and Shock Waves in Transonic Flow*, Journal of the Aeronautical Sciences, Vol. 13, No. 12, p. 623, December, 1946.

First U. S. National Congress of Applied Mechanics

Plans have been formulated to hold the First U.S. National Congress of Applied Mechanics on June 11–16, 1951, at Chicago, Ill. The Illinois Institute of Technology will be host to the Congress.

Members of the Institute, one of the sponsoring societies, are cordially invited to submit papers, which should constitute original research in applied mechanics. (Their length must not exceed 5,000 words or the equivalent in equations, tables, and diagrams.) Abstracts must be submitted to the Chairman of the Editorial Committee before April 14, 1951; complete papers must be submitted prior to June 11, 1951.

Additional information about the Congress may be obtained by writing to N. M. Newmark, Secretary of the Congress, University of Illinois, Urbana, Ill. All members are invited to attend.

Remarks on Low-Aspect-Ratio Configurations in Supersonic Flow*

P. A. LAGERSTROM† AND M. E. GRAHAM‡
Douglas Aircraft Company, Inc.

SUMMARY

Simple low-aspect-ratio configurations are examined to obtain a qualitative understanding of wing-fuselage interference and "afterbody" effect of a missile. Slender-body theory gives for a wing-body combination a value of lift which does not depend upon afterbody length. This value of lift is compared with that given by the more exact linearized three-dimensional theory. Nonlinear and viscous effects are not considered.

A theorem is proved concerning the lift of certain wings (or wing-fuselage combinations) with a long afterbody of span equal to the maximum span of the wing. It states that at any supersonic Mach Number the value of lift according to linear theory tends to that predicted by slender-body theory as the length of the afterbody tends to infinity. The effect of a finite afterbody can also be determined by linear theory, and a comparison can be made with slender-body theory for certain planar systems.

These results may be applied qualitatively to wing-body combinations. They indicate that, for no afterbody, slender-body theory overestimates the lift of the combination and that, for a short afterbody, it may equal or even underestimate the lift. For an infinitely long afterbody, it agrees exactly with linear theory if the afterbody span equals the maximum wing span; if the afterbody is narrower, it overestimates the lift.

NOTATION

a	=	radius or half-width of body
A	=	aspect ratio
A_r	=	βA, reduced aspect ratio
c	=	chord
C_p	=	pressure coefficient
E	=	$E(\sqrt{1-\Omega^2})$, complete elliptic integral of second kind
k	=	a/s, ratio of body radius (or half width) to maximum semispan of wing-body combination
l	=	lift per unit span of wing
L	=	lift
M	=	free-stream Mach Number
q	=	$(1/2)\rho U^2$
s	=	maximum semispan of wing-body combination
s'	=	$s + x_3 \tan \omega$, local semispan of wing-body combination
u_2	=	component of flow velocity in x_2 direction
U	=	free-stream velocity
x_1, x_2, x_3	=	Cartesian coordinates, directed in spanwise, vertical, and streamwise directions, respectively. Origin is at intersection of body axis and wing trailing edge
α	=	angle of attack (rad.)
α_a	=	apparent angle of attack (geometrical plus that induced by upwash field)
β	=	$\sqrt{M^2-1}$
ω	=	half apex angle of delta wing
Ω	=	$\beta \tan \omega$

Subscripts

A	=	afterbody
B	=	total body
W	=	wing

Received May 25, 1950.

* This paper is nearly identical in content with the first part of reference 1.

† Consultant, Santa Monica Plant. Also, Associate Professor of Aeronautics, California Institute of Technology.

‡ Aerodynamicist, Santa Monica Plant.

INTRODUCTION

CONSIDER A TYPICAL MISSILE such as shown in Fig. 1. It will be assumed that the fuselage has a circular cross section and is cylindrical except near the nose. The lifting surfaces are flat plates of some simple plan form like a delta wing; the wings are set at zero incidence to the body. A solution for this missile as a whole may be obtained formally by slender-body theory.[2–4] From this solution it would appear that the tail is completely ineffective; its geometrical angle of attack (assuming zero incidence to body) is completely canceled by the upwash field induced by the wing and the fuselage. However, this is a highly unrealistic result obtained by using slender-body theory beyond its intended application.

To analyze this situation, the missile will first be considered without the tail. Even in this case there is an unrealistic consequence of slender-body theory—namely, that the afterbody carries no lift and, hence, that its length is unimportant. This is connected with the fact that slender-body theory shows no Mach Number effect. Therefore, a critical discussion of the relation between slender-body theory and the more exact linearized theory is given.

The question of the lift of the tail requires a study of the development of the vortex sheet. This problem will not be discussed here. However, once the upwash field in the tail region has been found by some method, the problem of wing-tail-fuselage interference reduces to a study of tail-fuselage interference. The tail is a lifting surface like the wing, although its apparent

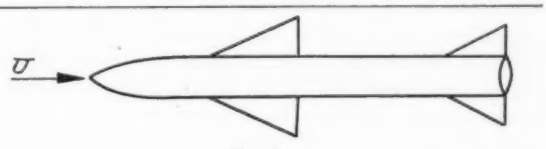

FIG. 1.

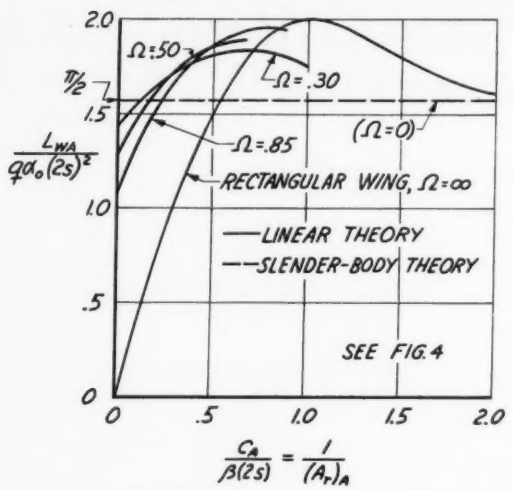

FIG. 2. Variation of lift with afterbody length, delta wing with flat afterbody.

angle of attack may vary spanwise in some complicated manner. In general, the tail-fuselage combination has no afterbody. Because of this, a different estimate may have to be used for tail-fuselage interference than for wing-fuselage interference.

WING-FUSELAGE INTERFERENCE, AFTERBODY EFFECTS

In treating the lift of a wing by linear theory, it is always possible to use a superposition principle. First, the upwash field of the fuselage alone is computed. Let the apparent angle of attack of the wing be defined as the geometrical angle of attack plus the angle of attack induced by this upwash field. The problem then reduces to the study of a wing with this apparent angle of attack in the presence of a fuselage at zero angle of attack. This reformulation of the problem is convenient for wings of high aspect ratio and with a high ratio of span to body diameter. In this case, the fuselage at zero angle of attack influences only a small part of the wing, and its influence may be understood and estimated with the aid of the idea of preservation of lift.[5]

However, a different approach to the problem is advantageous for the cases considered in this paper, especially when the leading edges are subsonic. Since slender-body theory[3, 4] gives directly a solution for the original combination of the wing and fuselage, it has been selected as the basis of the investigations. Corrections and comparisons to this theory are presented in the discussions. Slender-body theory does not show that the lift has a dependence on Mach Number or the length of the afterbody. A linearized theory would show these effects, but a complete treatment with the linearized theory would be cumbersome. Therefore, these effects will first be studied for planar systems (wings) for which the two methods may be directly compared.

(I) *Low-Aspect-Ratio Rectangular Wing*

Linearized Theory.—Equations for the lift and center of pressure of a rectangular wing for a reduced aspect ratio varying between 1 and ∞ are easily computed—e.g., by the method of conical flow.[6] For lower aspect ratios, the method of cancellation of lift[6, 7] or Evvard's method[8] may be used. Near the leading edge the pressure distribution is two-dimensional, while further downstream there is a complicated system of expansion and compression waves which eventually decreases the pressure distribution to a small fraction of its two-dimensional value. (This is discussed in detail in reference 7.)

The lift of a rectangular wing for which $\frac{1}{2} \leqslant A_r \leqslant \infty$ is shown in Fig. 2. It is interesting to note that, if the span is held constant, the lift has its maximum value for a reduced aspect ratio of one; for lower reduced aspect ratios the lift decreases. This means that, if an additional strip (ABCD of Fig. 3) is added to a wing of reduced aspect ratio smaller than 1, at a positive angle of attack, the lift carried by this strip must be negative. The addition of this strip thus has the effect of decreasing the lift and forcing the center of pressure forward.

Slender-Body Theory.—It is convenient to treat the rectangular wing as a limiting case of a delta wing with a flat-plate afterbody (Fig. 4). (By "afterbody" is meant the flat plate downstream of AB in Fig. 4.) According to slender-body theory, all the lift is carried upstream of AB; the afterbody has zero perturbation pressure if it is at the same angle of attack as the forward delta wing. Furthermore, the lift is independent of the opening angle ω; it depends only on the maximum span according to the formula

$$L = (\pi/2)q\alpha_0(2s)^2 \qquad (1)$$

The rectangular wing is then obtained as a limiting case by letting the angle ω tend to $\pi/2$. Since Eq. (1) is independent of ω, it is still valid for the rectangular wing. Thus, for the rectangular wing all the lift would be concentrated at the leading edge, the rest of the

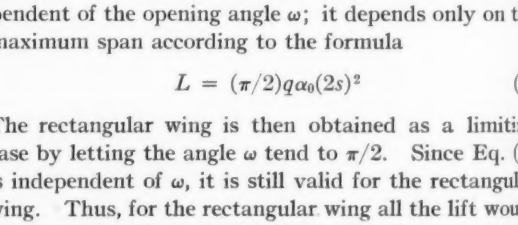

FIG. 3.

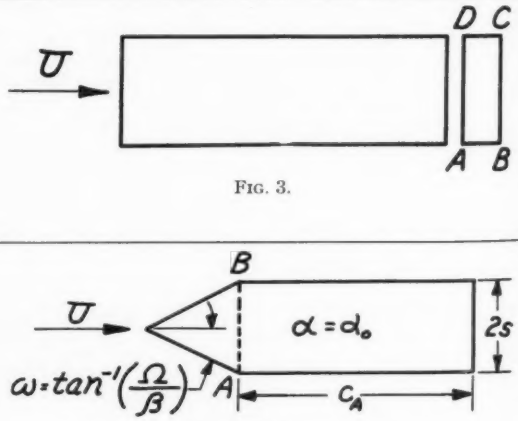

FIG. 4.

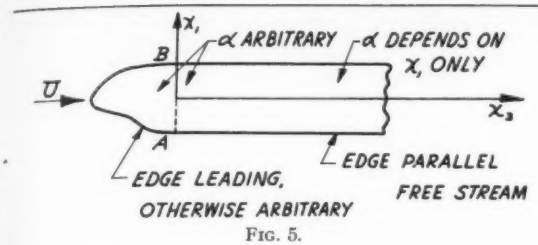

FIG. 5.

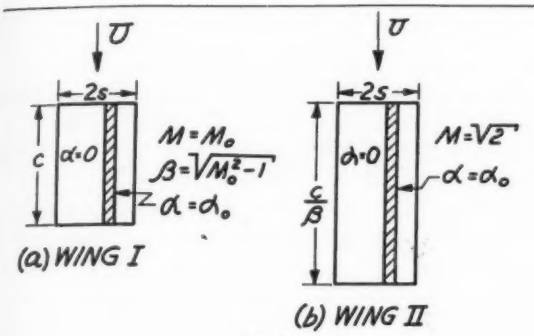

FIG. 6.

wing would have zero perturbation pressure, and the lift would be independent of the aspect ratio. This result is plotted in Fig. 2.

Comparison of the Two Theories.—Fig. 2 indicates that, as the aspect ratio approaches zero, the lift, according to linearized theory, tends to the value predicted by slender-body theory. It appears that slender-body theory anticipates the value of lift which would be obtained if the wing were of a sufficiently small aspect ratio. Note that, as the Mach Number M approaches 1, more and more of the reflections, in the system of compression and expansion waves which occurs according to linearized theory, are compressed toward the leading edge. According to slender-body theory (which corresponds to the limiting case $M = 1$), this whole wave system is, so to speak, concentrated at the leading edge. In the following section it will be shown that the asymptotic result indicated by Fig. 2 is actually correct not only for the rectangular wing but for a large class of plan forms.

(2) *General Theorem About Lift of Zero-Aspect-Ratio Wings**

Consider the wing shown in Fig. 5. The following assumptions are made:

Plan Form.—No part of an edge is trailing. Downstream of a certain chordwise station (AB in Fig. 5), the side edges become parallel to the free stream. The wing extends infinitely far downstream; its aspect ratio is thus zero.

Angle of Attack α.—α may be arbitrary everywhere except sufficiently far downstream where (for any fixed spanwise location x_1) α becomes a constant, $\alpha_0(x_1)$.†

Theorem: For the wing described above at supersonic speeds, linear theory gives the following results:

(2)
- (a) The lift is independent of Mach Number.
- (b) The angle-of-attack distribution on the forward part of the wing contributes nothing to the lift. The lift is determined exclusively by the values of $\alpha_0(x_1)$.
- (c) The value of the lift is identical with the one that would be obtained by slender-body theory (which corresponds to $M = 1$).

It can easily be seen that the proof given below will also be valid for appropriate nonplanar systems. Use of this will be made in Section (4).

Proof of (a).—Consider a rectangular wing (Fig. 6a) of finite aspect ratio for which the angle of attack is zero, except along a streamwise strip of differential width where it is α_0. Let the Mach Number M equal M_0. With the aid of the Prandtl-Glauert transformation, it is shown that wing I at $M = M_0$ has the same lift as the equivalent wing II at $M = \sqrt{2}$. (The equivalent wing has the dimensions and angle-of-attack distribution shown in Fig. 6b.) Now let the chord c grow to infinite length (Fig. 7); then wings I and II become identical. Hence, the lift of the wing of Fig. 7 is the same for $M = M_0$ as for $M = \sqrt{2}$—i.e., it is the same for all supersonic Mach Numbers. Thus, (a) of the theorem is proved for a special type of zero-aspect-ratio wing.

Next, consider a wing, like that in Fig. 8, which has a deflected square of infinitesimal area but which is otherwise at zero angle of attack. For this wing the lift is zero and, in particular, is independent of Mach Number. (This result follows if one wing of the type of Fig. 7 is subtracted from another such wing, since a supersonic wing has no upstream influence.) By

* A special case of this theorem is stated (without proof) in reference 10.

† It would be sufficient to require that $\alpha(x_1, 0, x_3)$ converges to a finite value $\alpha_0(x_1)$ as x_3 approaches infinity and that the side edges become asymptotically parallel to the free stream. We shall not be concerned with such mathematical refinements.

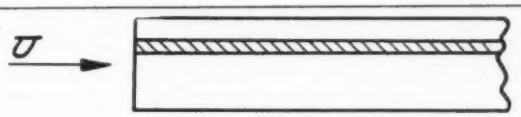

FIG. 7.

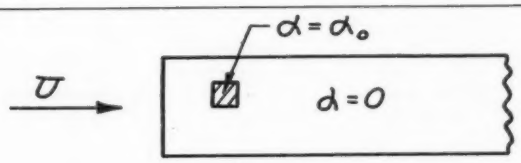

FIG. 8.

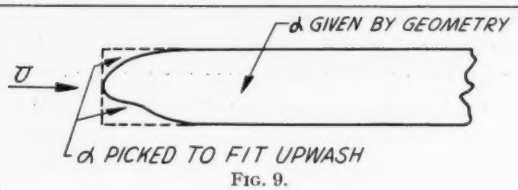

FIG. 9.

application of the superposition principle to the above results, it follows immediately that parts (a) and (b) of the theorem are true for any wing of rectangular plan form which satisfies the hypotheses of the theorem.

Finally, any wing of the type depicted in Fig. 5 may be considered as a rectangular wing by completing its plan form as in Fig. 9, giving to the added parts an angle-of-attack distribution that corresponds to the upwash of the original wing.

This completes the proof of parts (a) and (b). Part (c) follows from the fact that, since the lift is the same for all Mach Numbers, its value may as well be computed for the particular Mach Number of 1. The value is then the one that slender-body theory gives.

(3) *Narrow Delta Wing with Flat Afterbody*

Full-Span Afterbody.—Consider first the wing and afterbody of Fig. 10a. As was shown in the previous section, when the afterbody becomes extremely long, the lift as given by linear theory is very nearly that predicted by slender-body theory. For this particular wing this result will be studied in more detail.

It is of interest to check the consistency of theorem (2) by the following argument: The lift of wing (a) (Fig. 10) equals that of (b) plus that of the afterbody (c) at its apparent angle of attack. The lift of (b) is

$$L_W = \pi q \alpha_0 (2s)^2 / 2E(\sqrt{1 - \Omega^2}) \qquad (3)$$

For an afterbody of infinite chord, only the apparent angle of attack at the trailing edge is significant. The induced part of the apparent angle of attack is directly proportional to the upwash in the Trefftz-plane.

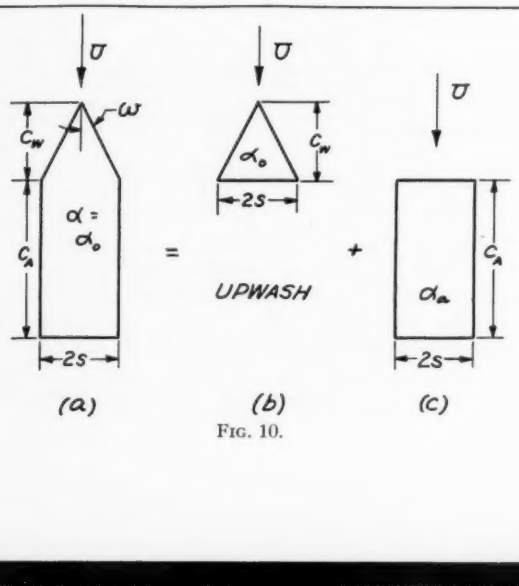

FIG. 10.

$$\alpha_a - \alpha_0 = u_2/U = -\alpha_0/E(\sqrt{1 - \Omega^2}) \qquad (4)$$

The lift of the afterbody is then

$$L_A = \frac{\pi}{2} q \alpha_a (2s)^2 = \frac{\pi}{2} q \alpha_0 (2s)^2 \left(1 - \frac{1}{E}\right) \qquad (5)$$

(For simplicity, the modulus of E, a complete elliptic integral of the second kind, is omitted.) Thus, adding L_A to L_W gives the slender-body result

$$L_{WA} = L_W + L_A = (\pi/2) q \alpha_0 (2s)^2 \qquad (6)$$

Since theorem (2) actually was used in the above argument, it cannot be said that the theorem has been checked by this argument even for this particular wing. However, at least the consistency of various methods has been verified.

Furthermore, for this plan form, as well as for the rectangular wing, it is possible to obtain linear theory results with the afterbody of finite length. Hence, for this case also, the validity of applying theorem (2) (i.e., slender-body theory) to a wing of low but nonzero aspect ratio may be checked. The linear theory results have been obtained from the charts of reference 9. The lift is plotted in Fig. 2 as a function of the reciprocal aspect ratio of the afterbody for three wings with different apex angles. These values are compared with the slender-body results. For no afterbody, slender-body theory predicts too much lift; as the afterbody first grows from zero to a finite length, it recovers more lift than slender-body theory predicts; finally, the lift appears to drop and, according to the previous section, would approach asymptotically the slender-body value if the curves were continued far enough. These curves are similar to that for the limiting case of a wing with a 90° half apex angle, the rectangular wing, which is shown on the same graph and was discussed previously.

Note that as $\omega \to 0$ the pressure distribution as given by linearized theory approaches that given by slender-body theory. This is one aspect of slender-body theory. The aspect of this theory emphasized in this paper is that for any value of ω (even for supersonic leading edges) the total lift, but not the pressure distribution, approaches that predicted by slender-body theory as the length of the afterbody increases. In the first case the relevant parameter is actually $\beta \tan \omega$; in the second case, $c_A/\beta(2s)$.

Narrow-Span Afterbody.—For the applications it is desirable to know what happens when the span of the afterbody is smaller than the maximum span of the delta wing (Fig. 11). Theorem (2) does not apply directly to this configuration, but it may be applied separately to the afterbody as was done at the beginning of this section. Slender-body results are not realized as the chord of the afterbody tends to infinity. As it is to be expected, the lift is smaller than for the combination with a full-span afterbody (Fig. 10). It

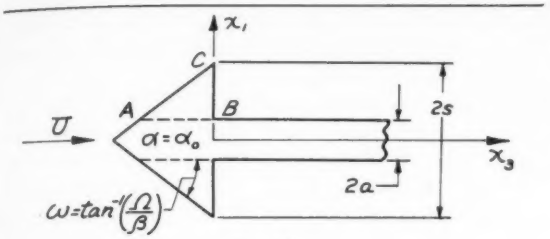

FIG. 11.

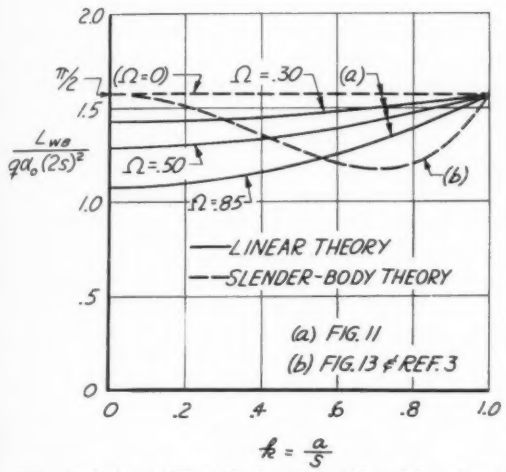

FIG. 12. Variation of lift with afterbody width, delta wing with infinitely long afterbody.

may be expressed by the equations for that case [Eqs. (3), (5)] by introducing a factor dependent upon the ratio of body span to wing span.

$$L_{WA} = \frac{\pi q\alpha_0(2s)^2}{2E} + \frac{\pi q\alpha_0(2a)^2}{2}\left(1 - \frac{1}{E}\right) = L_W + k^2 L_A \tag{7}$$

where $k = a/s$ and L_W, L_A refer to configuration of Fig. 10.

This plan form displays more of the characteristics of an actual wing-body combination than did the previous examples, but only the lift for the limiting case of an infinitely long afterbody may readily be found.* This is plotted in Fig. 12 as a function of k.

(4) *Delta-Wing Fuselage Combination with Cylindrical Afterbody*

The wing-body combinations considered in the previous section had flat bodies. These were discussed because they do contribute to the understanding of the wing-body problem and because solutions for such cases are more easily obtained than for a combination with a more realistic fuselage shape. Spreiter[3] and Ward[4] have both obtained the slender-body results for a combination with a circular-cylinder body (Fig. 13). Their results for the total lift of such a configuration are given in Eq. (8) and Fig. 12.

$$L_{WB} = (\pi/2)q\alpha_0(2s)^2\,(1 - k^2 + k^4) \tag{8}$$

For this more realistic configuration, various results for the pressure distribution on the wing will also be examined. Spreiter[3] has found the theoretical pressure distribution for various slender wing-body combinations. The pressure distribution on the wings of the combination of Fig. 13 is

$$(C_P)_W = \frac{-2\alpha_0 \tan\omega\left[1 - \left(\frac{a}{s'}\right)^4\right]}{\sqrt{\left[1 + \left(\frac{a}{s'}\right)^4\right] - \left(\frac{x_1}{s'}\right)^2\left[1 + \left(\frac{a}{x_1}\right)^4\right]}} \tag{9}$$

$s' = s + x_3 \tan\omega$ is the local semispan. The spanwise lift is then

$$l_W = -2q\int_{(x_1 - s)/\tan\omega}^{0} C_P\,dx_3 = 4q\alpha_0 a \times \sqrt{\left(1 - \frac{x_1^2}{s^2}\right)\left(\frac{s^2}{a^2} - \frac{a^2}{x_1^2}\right)} \tag{10}$$

and the total lift carried on the exposed wing area is

$$L_W = 2\int_a^s l\,dx_1 = 4q\alpha_0 a^2\left[\left(\frac{s}{a} + \frac{a}{s}\right)^2 \times \tan^{-1}\frac{s}{a} - \pi - \left(\frac{s}{a} - \frac{a}{s}\right)\right] \tag{11}$$

It is interesting to compare this loading with that on the corresponding portion of a slender delta wing (Fig. 11). The pressure is

$$(C_p)_W = -2\alpha_0 \tan\omega/\sqrt{1 - (x_1/s')^2} \tag{12}$$

the spanwise lift is

$$l_W = 4q\alpha_0\sqrt{s^2 - x_1^2} \tag{13}$$

and the total lift carried on the region ABC is

$$L_W = 2q\alpha_0 a^2\left[\left(\frac{s}{a}\right)^2 \cos^{-1}\frac{a}{s} - \sqrt{\left(\frac{s}{a}\right)^2 - 1}\right] \tag{14}$$

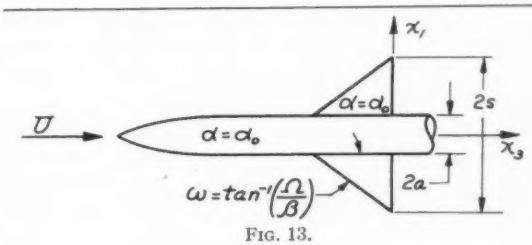

FIG. 13.

* Linearized calculations for the case of a short afterbody may be found by the method of cancellation of lift.[7] These cumbersome calculations have not been carried out. However, from the behavior of the corresponding curves for $k = 1$, it is to be expected that, for k values that are not too small, the full slender-body value of the lift may be realized for certain moderate values of the length of the afterbody.

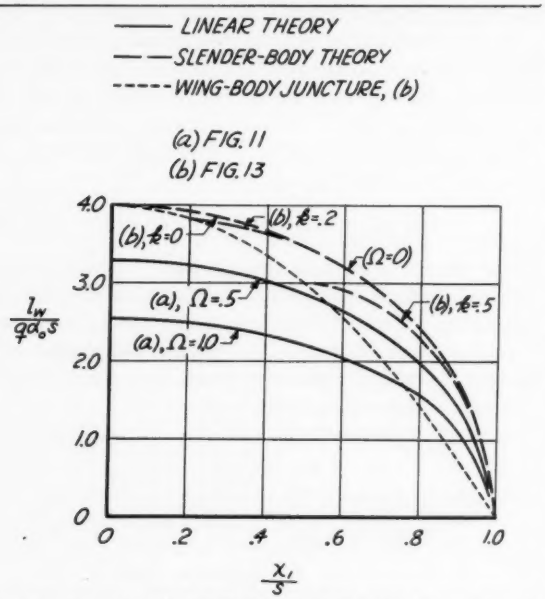

FIG. 14. Spanwise lift distribution on delta wing in presence of body.

In Fig. 14 the spanwise lift as given by Eq. (13) is compared with that given by Eq. (10). For a small value of a/s there is little difference between the two curves. Linear theory values corresponding to Eq. (13) are also shown. It is possible that, for configurations in which the Mach Number effect cannot be neglected, there is similarly not too much difference between the lift distribution on the outer region of a delta wing and the lift distribution on the wing of a combination with a circular-cylinder fuselage.

Thus, for zero afterbody, the linearized theory will undoubtedly give less lift than will the slender-body theory. A similar difference between linear theory and slender-body theory may be illustrated by a wing-body combination for which the wing area has shrunk nearly to zero ($s \doteq a$) though the wing apex angle ω remains fixed (Fig. 15). For this tiny wing the body acts as a vertical wall. Then, linear theory predicts that the lift carried by the wing-body combination is just *twice* the lift that the wing alone would carry. (The angle of attack induced by the body upwash equals the geometrical angle of attack.) None of the wing lift is carried on the body. Slender-body theory, on the other hand, predicts that, for a wing of vanishing size, the lift of the wing-body combination is *four* times the lift that the wing would carry if it were alone in the free stream. This is shown by Ward in reference 4.

According to both theories, the lift carried on the wing is doubled by the presence of the body. However, according to slender-body theory, an equal amount of lift is also carried on the body. If, on the other hand, one decreased the wing span by letting $\omega \to 0$ while keeping the wing area fixed, the theories would give the same result, since the combination is approaching more nearly a "slender" configuration.

Theorem (2) may be proved just as easily for nonplanar as for planar systems; hence, for the configuration in Fig. 16 slender-body values will be realized as the length becomes infinite. The examples of the triangular wings suggest that, for a finite length, even more lift than is predicted by slender-body theory may be realized. Finally, the case for which the afterbody is finite and has only a cylindrical part (Fig. 1 without tail surfaces) may be compared with the corresponding flat-plate wing discussed in Section (3). It is to be expected that, for zero afterbody, the lift is lower than that predicted by slender-body theory. Then, with increasing afterbody length the lift will increase and possibly exceed the slender-body value. Beyond a certain optimum length, added afterbody will be detrimental to the lift. Although quantitative estimates are not obtained this way, wind-tunnel measurements may be studied in the light of these qualitative arguments. Of course, these arguments neglect nonlinear effects and viscosity.

REFERENCES

[1] Lagerstrom, P. A., and Graham, M. E., *Aerodynamic Interference in Supersonic Missiles*, Douglas Aircraft Company Report No. SM-13743, July, 1950.

[2] Jones, R. T., *Properties of Low-Aspect-Ratio Pointed Wings at Speeds Below and Above the Speed of Sound*, N.A.C.A. T.N. No. 1032, March, 1946.

(*Continued on page 100*)

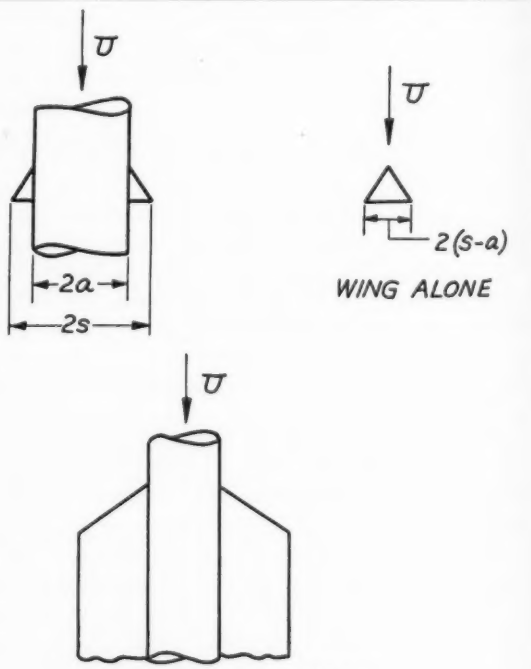

FIG. 15 (*top*). Fig. 16 (*bottom*).

Wind-Tunnel Tests for Temperature Recovery Factors at Supersonic Velocities

W. F. HILTON*

The Johns Hopkins University

(I) SUMMARY

Temperatures were measured on the surface of a tangential ogive attached to a 4-in. diameter cylinder. The tests were made at Mach Numbers of 1.73 and 2.00 in the Ordnance Aerophysics Laboratory wind tunnel in Texas. The model was made of Lucite, a thermal insulator, and the tests showed that the surface temperature experienced 88.0 per cent of the adiabatic stagnation temperature rise of the airflow just clear of the boundary layer. The experimental scatter amounted to about ½ per cent. These results compare with Squire's theory, which gives 89.42 per cent for a turbulent, and 84.56 per cent for a laminar, boundary layer.

The observed temperatures gave no indication of the position of transition, which is thus at variance with the work of Hilton and Wingham at high subsonic speeds.

(II) INTRODUCTION

IN ATTEMPTING TO FLY at progressively higher speeds, we have so far been limited mainly by the aerodynamic drag exceeding the thrust of the propulsion unit. However, it would appear that we shall be able to increase the speed of aircraft and missiles by attention to detail, and the question arises as to what will ultimately determine the greatest speed at which we can move through the air. Undoubtedly, the answer to this question lies in the aerodynamic heating due to skin friction and adiabatic compression that occurs on the surface of all vehicles moving at high speeds through air.

This problem breaks down into two main divisions: (1) The temperature attained by an unheated body, and (2) the temperature attained by a heated body and the rate of heat transfer to the airstream. Only the first of these is treated in the present note.

(III) PHYSICAL NATURE OF AERODYNAMIC HEATING

The air in contact with a moving body will experience a temperature rise even if brought to rest isentropically. In addition, the boundary layer will generate extra frictional heat by the rubbing of one layer upon another. This is offset by the direct conduction of heat from the boundary layer to the free stream across the narrow boundary layer. In the steady state there will be zero heat flow into the surface, which will take up an energy level higher than the free stream and thus be hotter than the free stream. The nondimensional parameter that expresses the balance between a frictional heating and the conductive cooling is called the Prandtl Number (σ) and is given by

$$\sigma = \mu c_p / K \tag{1}$$

where μ and K are the coefficients of viscosity and thermal conductivity and c_p is the specific heat.

If the Prandtl Number is unity, the frictional effect just balances the heat-conduction effect, so that the heating of the surface would correspond exactly to the isentropic stagnation heating obtained when air is retarded from a velocity V to zero velocity on the surface. This isentropic temperature rise is given by the equation

$$T_0 - T = (1/2)\,(V^2/c_p) \tag{2}$$

In the case of air, c_p has the value 6,002 ft.^{2} sec.$^{-2}$ per °F. and the Prandtl Number = 0.715, indicating that the thermal conductivity of air is of greater relative importance than the frictional effects. Thus, we should expect to find that a body placed in an air stream would not experience the full isentropic rise of temperature because of this extra thermal conductivity.

For large temperature differences, the effect of heat radiation from the hot surface should also be considered. No attempt has been made to allow for this in the analysis given below.

The rise of temperature δT through a laminar boundary layer has been shown by theory[2] to be given by

$$\delta T_{\text{lam.}} = (1/2)\,V^2\sigma^{1/2}/c_p = (1/2)\,(\gamma - 1)\,M^2 T\sigma^{1/2} \tag{3}$$

or

$$2\delta T_{\text{lam.}} c_p / V^2 = \sigma^{1/2} = 0.8456 \text{ for air} \tag{4}$$

where δT is the difference of temperature between the surface and the airflow just clear of the boundary layer and M is the Mach Number just clear of the surface at a point where the absolute temperature is T.

For a turbulent boundary layer, the temperature rise is shown by

$$\delta T_{\text{turb.}} = \frac{(1/2)\,V^2\sigma^{1/3}}{c_p} = \frac{1}{2}\,(\gamma - 1)M^2 T\sigma^{1/3} \tag{5}$$

or

$$2\delta T_{\text{turb.}}\, c_p / V^2 = \sigma^{1/3} = 0.8942 \tag{6}$$

Presented at the Bumblebee Aerodynamics Symposium held at the Applied Physics Laboratory, November 4–5, 1948. Received May 3, 1950.

* Applied Physics Laboratory. Now, Armaments Division, Armstrong Whitworth Aircraft Ltd., England.

Thus, we expect to recover at the surface 89.4 per cent (or 84.6 per cent if laminar) of the temperature rise that would be experienced by the air just clear of the boundary layer if brought to rest adiabatically.

(IV) Experimental Work in the O.A.L. Wind Tunnel

An accurate determination of the temperature taken up by a solid surface under conditions of supersonic airflow will be essential if we are to fly vehicles at or near the point where the skin of the vehicle will be on the point of thermal failure. Accordingly, an unheated model was made and tested in the O.A.L. Daingerfield wind tunnel. The model was constructed from a single piece of Lucite (part of a sheet 4 in. thick), and its exact shape is given in Fig. 1. Lucite (Perspex) was used in the construction of the model to reduce the effects of the thermal conductivity through the model itself. The temperature was measured at 23 stations along the surface of the model by means of small silver studs to which thermocouples were attached at the rear. Tests were conducted at a Mach Number of 2 and angles of yaw of $-2°$, $-1°$, $0°$, $1°$, $2°$, and $4°$. Angles of yaw of $4°$, $2°$, $0°$, $-2°$, and $-4°$ were tested at $M = 1.73$. The thermocouples were connected in series so that the difference between one thermocouple and the next was measured directly on the instrument. This reduced fluctuations due to slight variations of conditions from time to time in the tunnel.

It was found that painting a bright silver stud with dull black paint did not produce a measurable change in reading. Hence, the effects of radiation were negligibly small.

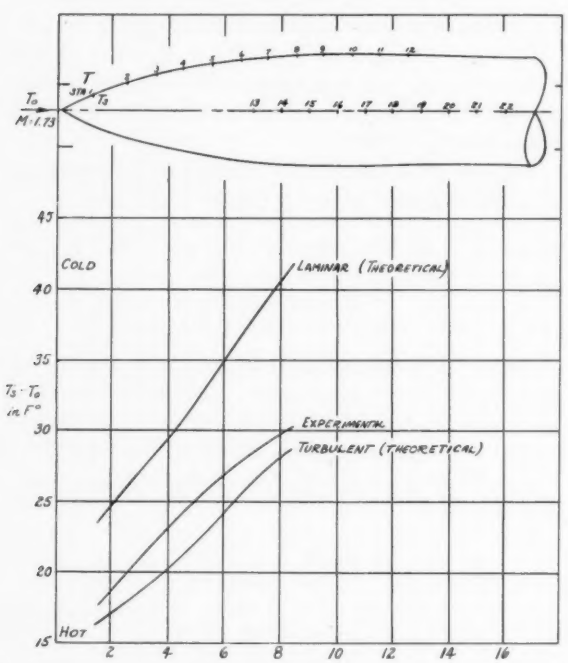

Fig. 1a. Comparison of experimental temperature with theory; $\alpha = 0°$ and $M = 1.73$.

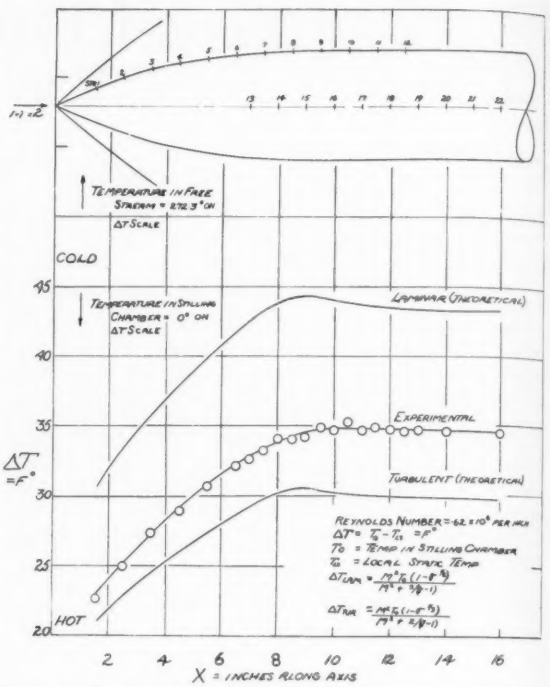

Fig. 1b. Comparison of experimental temperatures with theory; $\alpha = 0°$ and $M = 2.0$.

(V) Reduction of Experimental Results

The flow over the unyawed model is axially symmetric and was calculated by the method of characteristics as applied to axially symmetric flow.[3] Accordingly, the readings on the unyawed model were reduced in much greater detail than was possible when the model was yawed.

Two methods of presenting the observations have been adopted. In the lower part of Fig. 1, the raw data are plotted to show measured temperature difference against axial position of thermocouple button. The theoretical curves for both laminar and turbulent flow, calculated from Squire's theory as given in Eqs. (3) and (5), are also shown in Fig. 1.

Put in the more useful forms

$$\Delta T_{\text{lam.}} = T_0 - T_s = \frac{M^2 T_0 (1 - \sigma^{1/2})}{M^2 + 2/(\gamma - 1)}$$

and

$$\Delta T_{\text{turb.}} = T_0 - T = \frac{M^2 T_0 (1 - \sigma^{1/3})}{M^2 + 2/(\gamma - 1)}$$

In Fig. 2, the experiment and theory have been reduced to the form of a nondimensional temperature recovery factor C_θ, which is defined below in Eq. (7). It was defined in this way because it reduces theories of the type of Squire's to the form C_θ = constant and

is thus convenient to use and to remember. We define

$$C_\theta = (T_s - T)/(T_0 - T) \tag{7}$$

where

T_0 = stilling chamber temperature or "total" adiabatic compression temperature (invariant even through a shock wave)

T = "static" temperature just clear of the boundary layer, as shown by thermometer moving with the air

T_s = surface temperature as measured

This definition of temperature recovery factor is different from that used by Eber,[4] who defined a coefficient C given by

$$C = (T_s - T_1)/(T_0 - T_1)$$

where T_1 is the "static" temperature of the free stream ahead of the body.

Continuing with the definition given in Eq. (7), we know from fundamental thermodynamic relations that

$$a^2 = \gamma RT = (\gamma - 1)\, c_p\, T$$

and we may thus rewrite Eq. (2) to read

$$T_0 - T = (1/2)\, V^2/c_p = (1/2)\, V^2(\gamma - 1)\, T/a^2 = (1/2)\,(\gamma - 1)\, M^2\, T \tag{8}$$

Since the free-stream temperature T cannot be measured by any known device, we eliminate it between Eqs. (7) and (8) and rearrange to find

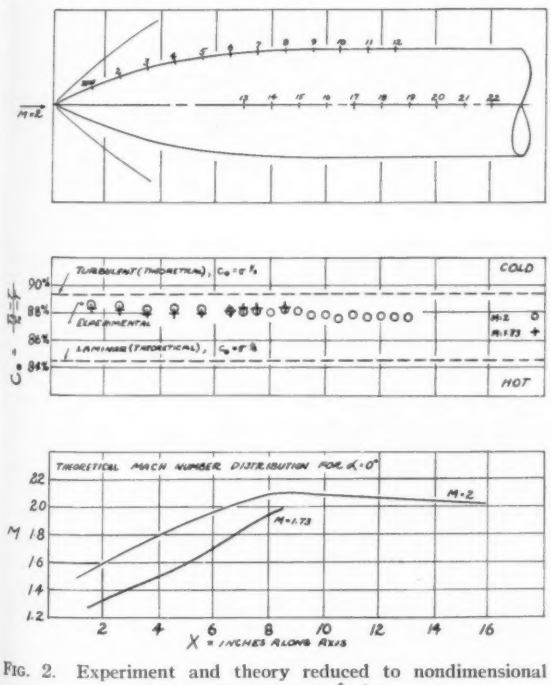

FIG. 2. Experiment and theory reduced to nondimensional temperature recovery factor.

FIG. 3. Direct shadow spark photograph of flow pattern at $\alpha = 0°$, $M = 2$. Note apparent transition about halfway along ogive.

$$C_\theta = 1 - \left(\frac{2}{\gamma - 1}\right)\frac{T_0 - T_s\,[1 + (1/2)\,(\gamma - 1)M^2]}{T_0\, M^2}$$

$$= 1 - \frac{(T_0 - T_s)\,[M^2 + 2/(\gamma - 1)]}{T_0 M^2} \tag{9}$$

Eq. (9) expresses the temperature coefficient in terms of M (which may be calculated), the observed temperature T_0, and the observed temperature difference $(T_0 - T_s)$. This equation was used in reducing the observations to the nondimensional coefficient form. The Mach Number distribution around the model was obtained by the method of axially symmetric characteristics mentioned above. The reduced readings are shown in Fig. 2 in the form of temperature recovery factor against axial distance along the model.

In order to reproduce Squire's theory on Fig. 2, we take Eq. (3) for a laminar boundary layer and write it in the form

$$\delta T = T_s - T = (1/2)\, V^2 \sigma^{1/3}/c_p$$

But from Eq. (7), defining the temperature recovery factor,

$$C_{\theta_{\text{lam.}}} = \frac{T_s - T}{T_0 - T} = \frac{(1/2)\, V^2 \sigma^{1/3}/c_p}{(1/2)\, V^2/c_p} = \sigma^{1/3} \tag{10}$$

Similarly, the theoretical expression for a turbulent boundary layer may be written

$$C_{\theta_{\text{turb.}}} = \sigma^{1/3} \tag{11}$$

(VI) Discussion of Results

It is at once apparent from a study of Fig. 1 that the readings are consistent to about 0.2°F. and, hence, from Fig. 2, that the uncertainty in temperature recovery

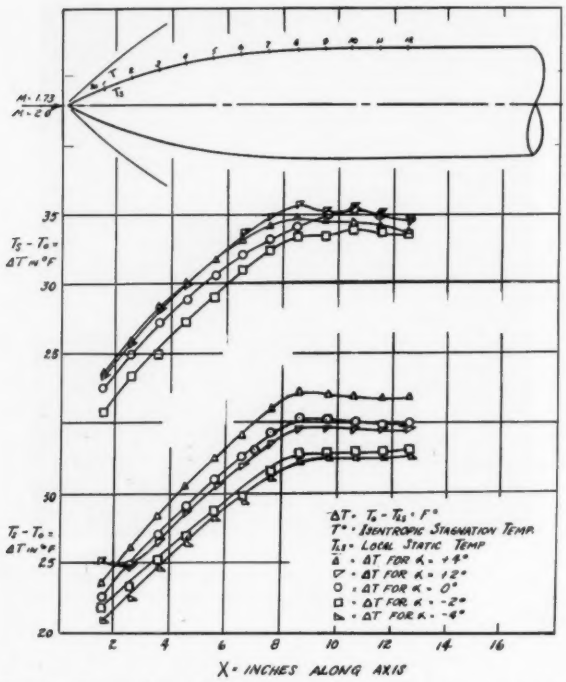
M-1.73
M-2.0
$T_s - T_0$ = ΔT in °F
$T_s - T_0$ = ΔT in °F
ΔT = $T_s - T_{s_1}$ = F°
T° = Isentropic Stagnation Temp.
T_{s_1} = Local Static Temp
Δ = ΔT for α = +4°
▽ = ΔT for α = 2°
○ = ΔT for α = 0°
□ = ΔT for α = -2°
▷ = ΔT for α = -4°
X = INCHES ALONG AXIS

FIG. 4. Comparison of experimental temperatures with angle of attack.

factor C_θ is only of the order of $^1/_2$ per cent. This is regarded as extremely satisfactory.

The value of the temperature recovery factor is 88.0 per cent for these experiments. This is a little cooler than Squire's theoretical value of 89.42 per cent for a turbulent boundary layer but much warmer than the theoretical figure of 84.56 per cent for a laminar boundary layer.

Fig. 3 shows a photograph by the direct shadow method of the flow at $M = 2$ over the cone at $\alpha = 0°$ and taken at the same time as the temperature measurements on which Fig. 2 is based. It was discovered independently by H. H. Pearcey at N.P.L., England, by workers in Germany during World War II, and by Moffett Field, N.A.C.A., that it is usually possible to determine where transition occurs from laminar to turbulent boundary layer by inspection of flow photographs by the direct shadow method. There is a white line parallel to the surface of the body which is characteristic of a laminar boundary layer, and this white line disappears or becomes confused in nature in the case of a turbulent boundary layer. A study of the photograph shown in Fig. 3 indicates that such a transition appears to occur on the ogive about 4 in. back from the pointed nose.

This is not consistent with the temperature observations, which do not exhibit a fluctuation at this position, but is mentioned for the sake of completeness.

(VII) Conclusion

It would appear that on an ogive of initial half angle 24.91° at a Mach Number of 1.73 or 2, we can expect a temperature recovery factor (temperature coefficient) of 88 per cent of the adiabatic temperature rise calculated on the basis of the velocity just clear of the boundary layer at the point in question. This nondimensional recovery factor defined in Eq. (7) appears to be a useful concept.

References

[1] Hilton, W. F., and Wingham, P. J., *Surface Temperatures on an Aerofoil at Subsonic Speeds*, British R. & M. 2230, January, 1946.

[2] Squire, H. B., *Heat Transfer Calculation by Aerofoils*, British R. & M. 1986, 1942.

[3] Cronvich, L. L., *A Numerical-Graphical Method of Characteristics for Axially Symmetric Isentropic Flow Problems*, Journal of the Aeronautical Sciences, Vol. 15, No. 3, March, 1948.

[4] Eber, G., *Experimental Research on Friction, Temperature and Heat Transfer for Simple Bodies at Supersonic Speeds*, Archiv., Kochel, Vol. 66, p. 57, November, 1941.

Remarks on Low-Aspect-Ratio Configurations in Supersonic Flow

(*Continued from page 96*)

[3] Spreiter, J. R., *Aerodynamic Properties of Slender Wing-Body Combinations at Subsonic, Transonic and Supersonic Speeds*, N.A.C.A. T.N. No. 1662, July, 1948

[4] Ward, G. N., *Supersonic Flow Past Slender Pointed Bodies*, Quart. Jour. Mech. & Applied Math., Vol. II, Pt. 1, pp. 75–97, March, 1949.

[5] Lagerstrom, P. A., and Van Dyke, M. D., *General Considerations About Planar and Non-Planar Lifting Systems*, Douglas Aircraft Company Report No. SM-13432, June, 1949.

[6] Lagerstrom, P. A., *Linearized Supersonic Theory of Conical Wings*, N.A.C.A. T.N. No. 1685, January, 1950.

[7] Lagerstrom, P. A., and Graham, M. E., *Low Aspect Ratio Rectangular Wings in Supersonic Flow*, Douglas Aircraft Company Report No. SM-13110, December, 1947.

[8] Evvard, J. C., *Distribution of Wave Drag and Lift in the Vicinity of Wing Tips at Supersonic Speeds*, N.A.C.A. T.N. No. 1382, July, 1947.

[9] Lapin, E., *Charts for the Computation of Lift and Drag of Finite Wings at Supersonic Speeds*, Douglas Aircraft Company Report No. SM-13480, October, 1949.

[10] Munk, M. M., *The Reversal Theorem of Linearized Supersonic Airfoil Theory*, Jour. Appl. Phys., Vol. 21, pp. 159–161, February, 1950.

Structural Load Measurements on Complex Aircraft Components Using Strain-Gage Summation Circuits

MAURICE A. WALTER*

Naval Air Experimental Station, Philadelphia

SUMMARY

A method for the measurement of incremental structural loads on complex aircraft surfaces without previous knowledge of load distribution is presented. The judicious location of electric strain gages and a suitable electric circuit with a single channel output to a recording mechanism are the means of effecting the measurement. Since the output of the strain-gage circuit is generally fed into an amplifier and then to a recorder, equations for a bridge looking into a high impedance are developed for measuring loads in a complex surface, and application of the equations is illustrated. Both design and experimental data are shown. The electrical equipment used is described. An approach similar to the one presented can be used for other types of strain-gage circuits.

Static test calibrations using the method have indicated a maximum error of 3.7 per cent in a complex surface, such as a horizontal stabilizer of a fighter airplane.

NOMENCLATURE

g	=	gain factor
K	=	electric strain-gage factor
K	=	(with subscript) a structural-electrical constant to relate mechanical load input with voltage output
L	=	lower strain gage
M	=	bending moment
P	=	shear load
T	=	torque
U	=	upper strain gage
V	=	output voltage of summation circuit
V_{AB}	=	bridge input voltage
V_{CD}	=	bridge output voltage
X	=	torque arm
x	=	interaction factor
Y	=	moment arm

Subscripts

L	=	left side of horizontal stabilizer
R	=	right side of horizontal stabilizer

NOTE: Other symbols and subscripts are defined in the text.

INTRODUCTION

IN THE TEXT THAT FOLLOWS, it is shown how electric strain gages are used to enable simple measurement of net loads on an airfoil surface of complex structure without previous knowledge of the load distribution. The development of the technique was carried out at the Cornell Aeronautical Laboratory, Inc., as part of a dynamic stability flight-test program on B-25J and F-80A airplanes under contract to the Aircraft Laboratory, Air Materiel Command, U.S.A.F.[2, 4]

Measurements of incremental vertical tail, horizontal tail, rudder, and elevator air loads were desired in connection with the above programs. Space limitations, particularly in the F-80A, ruled out a pressure-survey installation. In addition, some method that would eliminate the laborious data-reduction procedure of a pressure survey was desired.

The problems were solved by means of a summation electric strain-gage circuit, which enabled the measurement of the net incremental load on an airfoil surface through a single electrical output signal. Air load was then obtained by correcting the net load for inertia effects.

The technique stems from a method developed by I. G. Ross† for determining shear from a single electrical output of a strain-gage rosette in a bridge circuit.[1] Further developments enabled determination of shear and bending moments with a single measurement on a structure consisting of more than one load-carrying component. Properly located strain gages were electrically combined into a single bridge circuit, using fixed resistors as weighting factors to make the signal output independent of load distribution.[5] The technique was further improved when I. G. Ross and W. Hirtreiter‡ developed an electronic device to replace the fixed resistors.[2]

The following text carries the development of the technique to measurement of loads in complex surfaces.

SHEAR-LOAD MEASUREMENT IN A COMPLEX SURFACE

If, for example, it is desired to measure the incremental shear load on the horizontal stabilizer and it is only possible to mount gages in the surface itself, the most logical points to mount the strain gages would be the webs of the beams. However, the strain in the web is a function not only of shear load but of torsion, relief due to bending of a tapered beam, and secondary effects such as interaction between right- and left-hand stabilizer.

Received December 16, 1949. Revised and received June 9, 1950.

* Project Test Engineer. Formerly with the Flight Research Department, Cornell Aeronautical Laboratory, Inc.

† Chief of Wind Tunnel Department, Cornell Aeronautical Laboratory, Inc.

‡ Chief of Instrumentation Section, Flight Research Department, Cornell Aeronautical Laboratory, Inc.

No general equations can be written which will satisfy all cases for a complex structure. Each installation must be considered as an individual problem. The factors to be considered in writing the equations should be determined from static tests of the proposed installation. However, the method of attack will be similar for all cases. Therefore, an example will suffice to illustrate the method.

A measurement of the incremental shear load on the horizontal tail of a F-80A was desired. Static tests of strain-gage installations in the aft fuselage section and horizontal stabilizer indicated the most suitable locations for measuring the desired shear load were the two beam webs of the horizontal stabilizer. Since it is known from stress-analysis theory that the strain in the web is a function of torsion and bending in addition to shear, strain gages were installed on the flanges to measure bending in the same area as the web gages. Unfortunately, it was not possible to install gages that would respond to torsion only.

The characteristics of each gage pair are then determined by selecting several points on each side of the stabilizer and applying a series of loads at each point, first each side separately and then both sides symmetrically. A minimum of two gages are generally mounted on the structure forming two arms of a bridge to compensate for temperature effects. The response of each gage pair is measured separately, but all pairs are read in sequence under a steady load with a multiple-selector strain reader. From these data, plots of strain vs. load are drawn and the slopes determined. Other tests are made to determine the degree of superposition when two loads are applied at points on the same side of the stabilizer, the effect of fin loads on horizontal stabilizer strain gages, and the scatter of data. For the F-80A, tests showed that superposition occurred within ± 2 per cent; fin loads had no appreciable effects on the stabilizer gages except the front beam flanges, and data scatter was small.

The results of the main test showed that:

(1) All strain-gage signal responses were directly proportional to load with the exception of loads applied at the trailing edge of an inboard station.

(2) A shear and moment applied on one side of the stabilizer produced linear signal responses in web and flange gages, respectively, on both sides of the stabilizer.

(3) Though gages were symmetrically located on both sides as nearly as possible, sensitivities of corresponding gage pairs were not identical.

(4) Flange and web gages responded appreciably to torsion.

Equation of Bridge Output Voltage

The active strain gages generally form two arms of a Wheatstone bridge. In flight-test work, the flexibility of an amplifier system with an injected carrier voltage is of great advantage. The other two arms are usually the source of power for the bridge, and bridge output is fed to an amplifier. Consequently, the bridge looks into a high impedance. For small changes in bridge resistance, the case in strain-gage work, it can be shown that

$$V_{CD} = K_n \text{ (load)} \tag{1}$$

where the load can be shear, moment, or torque.

Method of Measuring Shear Load

The method for measuring the incremental load is to cancel out all components of the strain signals in the web gages not due to shear load. Flange gages are used for canceling out effects of bending. Since no gages could be mounted to measure torsion directly, an assumption must be made—namely, it is assumed the shear loads carried in the front and rear spars are in a constant proportion except for the shear due to torsion. This is based on the theory that no twist takes place when load is applied on the surface; the beams carry all the bending loads, and the shear boxes carry all the torsion. In an actual structure, twist does take place, but the assumption is close enough for our purposes. It is now possible to set up the equations of the load-measuring circuit, called a summation circuit. The simplifying assumptions used in the equations yield approximate results, which are further refined by experimental techniques. Therefore, these equations will serve to indicate the direction for experimental techniques of setting up a suitable summation circuit.

Setting Up of Equations and Solutions for Gain Factors

The signal outputs of the strain gages mounted on the beams without amplification are expressed as follows:

Right front beam web—

$$V_{CD1R} = K_{1R}M_R + K_{2R}(P_R + P_L x_{1R}) + K_{3R}T_R \tag{2}$$

Right rear beam web—

$$V_{CD2R} = K_{4R}M_R + K_{5R}(P_R + P_L x_{2R}) + K_{6R}T_R \tag{3}$$

Right rear beam flange—

$$V_{CD3R} = K_{7R}(M_R + x_{3R}M_L) + K_{8R}T_R \tag{4}$$

No equation is written for the front beam flanges, since static tests of the F-80A horizontal tail indicated that these gages would not be reliable; this may not be true for other cases.

Equations for the left side are identical in form. The constant coefficients (K's) are functions of the electrical circuit and structural properties of the member. These are determined from static tests by a method shown later in the text.

The term $K_{8R}T_R$ of Eq. (4) presents a problem, since no provisions are available to correct for this term. A preliminary study of the static-test data indicated that

a maximum error of 3 per cent would result from neglecting this term and $K_{8L}T_L$. Consequently, errors in experimental results may be partially explained by this neglect.

If the six pairs of gages are connected in the circuit of Fig. 1 and are modified to equalize signals on both sides of the stabilizer, the resulting voltage output will be

$$V = (V_{CD1R}g_{1R} + V_{CD2R}g_{2R} + V_{CD3R}g_{3R})g_R + (V_{CD1L}g_{1L} + V_{CD2L}g_{2L} + V_{CD3L}g_{3L})g_L \quad (5)$$

The gain factors, g_{1R}, g_{2R}, g_{3R}, and g_{1L}, g_{2L}, g_{3L} are to be related so that the voltage output of each side is proportional to the shear load on each side. The gain factors, g_R and g_L, equalize the signal output of each side to a given load, thereby enabling direct addition of the signals electrically.

The right-hand terms of Eqs. (2), (3), and (4) for left and right sides of the airplane, neglecting K_8T terms, are substituted. In the right side of Eq. (5), all terms are collected as factors of P_R, P_L, M_R, M_L, T_R, and T_L. The coefficients of the M_R, M_L, T_R, and T_L must equal zero in order that circuit signal output be proportional to shear load ($P = P_R + P_L$). It can then be shown that, in order to satisfy the above conditions,

$$g_{2R} = -(K_{3R}/K_{6R})g_{1R} \quad (6)$$

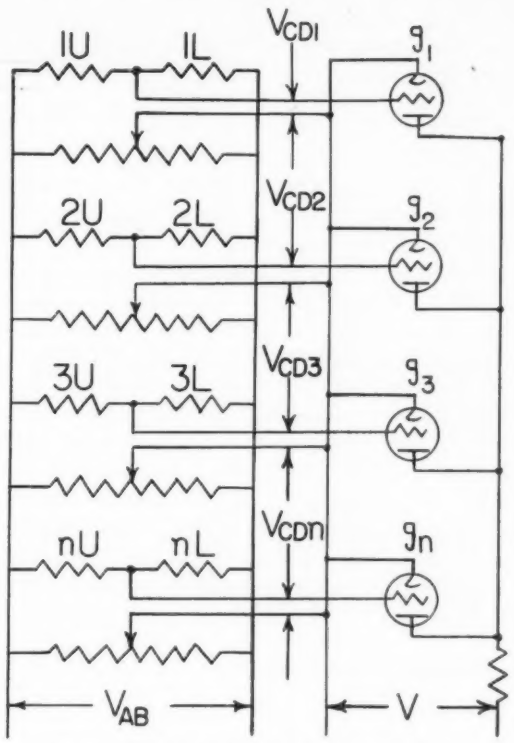

FIG. 1. Basic electrical circuit for summation.

Similarly,

$$g_{2L} = -(K_{3L}/K_{6L})g_{1L} \quad (7)$$

$$g_{3L} = \frac{g_R x_{3R}(K_{1R}g_{1R} + K_{4R}g_{2R}) - g_L(K_{1L}g_{1L} + K_{4L}g_{2L})}{K_{7L}g_L(1 - x_{3R}x_{3L})} \quad (8)$$

$$g_{3R} = -\frac{K_{1R}g_{1R}g_R + K_{4R}g_{2R}g_R + K_{7L}x_{3L}g_{3L}g_L}{K_{7R}g_R} \quad (9)$$

$$g_L = \frac{K_{2R}g_{1R} + K_{5R}g_{2R} - K_{2R}x_{1R}g_{1R} - K_{5R}x_{2R}g_{2R}}{K_{2L}g_{1L} + K_{5L}g_{2L} - K_{2L}x_{1L}g_{1L} - K_{5L}x_{2L}g_{2L}}\, g_R \quad (10)$$

For simplification, let

$$g_{1R} = g_{1L} = g_R = 1 \quad (11)$$

All the required gain factors have now been obtained and are expressed in terms of structural characteristics and electrical circuit constants, the K and x values, of the horizontal stabilizer. If it is desired to measure the shear loads on each side separately, Eq. (5) is written as two separate equations, one for the right side and one for the left. In this case, g_L and g_R are dropped. Eqs. (2) through (4) are then substituted in the equation for each side, and the g values are determined as for the case illustrated.

In the following paragraphs, methods for determining the K and x factors are presented.

Determination of K_1, K_2, K_3, K_4, K_5, K_6 *L & R*

Eqs. (2) and (3) are utilized in determining K_1 to K_6 for the left and right sides. The method for solving K_{1R}, K_{2R}, and K_{3R} only is developed here; the other values are determined in identical fashion.

Let us apply loads at n locations, separately, on the right horizontal stabilizer. From the results of these tests the slopes $(V_{CD1R}/P_R)_1$, $(V_{CD1R}/P_R)_2$, . . . , $(V_{CD1R}/P_R)_n$ are determined. The subscripts outside the parentheses represent the different locations. First, Eq. (2) is modified so that the output per unit shear load is expressed. $P_L = 0$, and, dividing by P_R, the following is obtained:

$$\left(\frac{V_{CD1R}}{P_R}\right)_n = K_{1R}\frac{(M_R)_n}{(P_R)_n} + K_{2R} + K_{3R}\frac{(T_R)_n}{(P_R)_n} \quad (12)$$

But $(M_R)_n = (P_R)_n Y_n$, where Y_n is the moment arm at station n and $(T_R)_n = (P_R)_n X_n$, where X_n is the torque arm at station n. Therefore, Eq. (12) becomes

$$(V_{CD1R}/P_R)_n = K_{1R}(Y_R)_n + K_{2R} + K_{3R}(X_R)_n \quad (13)$$

With n equations of the form of Eq. (13), values of K_{1R}, K_{2R}, and K_{3R} can be determined using the method of least squares. These K values are used for computing the gain factors.

In order to know the X distances, the elastic axis must be determined, either experimentally or analytically. As used here, the elastic axis is defined as that line on which a load may be applied without causing twist of the stabilizer at the station of load application. The X distance is measured parallel to the airplane's centerline from the point of load application to a line passing through the elastic axis at the gage installation station and perpendicular to the airplane's centerline.

Similar equations can be written to solve K_{4R}, K_{5R}, K_{6R}, K_{1L}, K_{2L}, K_{3L}, K_{4L}, K_{5L}, and K_{6L}.

K_{7R} and K_{7L} are determined in like manner from Eq. (4).

Determination of x Factors

Because of redundancy of fuselage and tail structure, a load applied on the right side of the horizontal tail produces a response on both sides of the tail, including that part of the left side of the horizontal tail outboard of the fuselage attachment fittings.

The interaction factor, x, is defined as the fraction of the signal sensitivity of a gage pair (K_2, K_5, K_7) due to a load placed on the opposite side of the tail. By this definition,

$$x_{1R} = K_{2RL}/K_{2R} \quad (14)$$

and

$$K_{2RL} = V_{CD1R}/P_L \quad (15)$$

where the RL subscript signifies a response on the right side of the stabilizer due to a load on the left side.

Similar equations are written for x_{2R}, x_{3R}, and x factors for the left side.

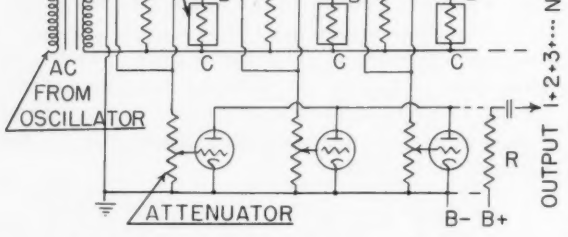

FIG. 2. Electronic strain-gage summation circuit.

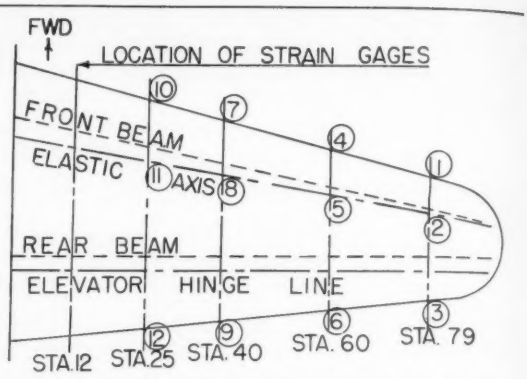

FIG. 3. Horizontal stabilizer loading point schedule, strain-gage installation location, and elastic axis.

Data for calculating the x factors are obtained by applying loads to the stabilizer on one side of the airplane and recording the responses of the gages on the other side.

The development of the circuit equations and the methods for determining the constants of these equations enable the actual design of a summation circuit for measuring horizontal tail load. However, before taking up the actual design of such a circuit, the equipment used will be described.

Description of Equipment

The basic circuit of the instrument enabling measurement of load on a complicated structure with a single channel output is shown in Fig. 1. The circuit diagram for a simple electronic summation unit constructed by the Cornell Aeronautical Laboratory, Inc., is shown in Fig. 2.[3] As shown, the strain gages are connected at points A, B, and C, where they compose two arms of a Wheatstone bridge. The other two arms, consisting of an adjustable resistor, are used for initial balancing of the bridge. The output signal of each bridge is fed to an attenuator that is connected to ground. The attenuator will pass any desired fraction of the output signal to the grid of the isolating amplifier. Each amplifier tube plate feeds the common load resistance, R; therefore, the voltage drop across R will be proportional to the algebraic sum of the signals across the grids of the six tubes. The voltage across R is then fed to the amplifier immediately preceding the recording device.

The settings of the attenuators are governed by the gain factors calculated from the preceding equations. In setting attenuators, the highest gain factor is arbitrarily given the value of 1. The other gain factors are then given proportional values. These decimal values are then set into the attenuators of the proper channels.

In practice, it is common to supply the bridges with an injected carrier voltage of 1,000 cycles per sec. With such a system, compensating condensers are re-

quired to enable bridge balance, even if all wiring is shielded. To minimize electrical "hash," tubes should be shock-mounted.

Design and Experimental Data

Static tests were carried out on the horizontal stabilizer in order to calculate the summation circuit gain factors defined by Eqs. (6) to (10). During the tests, the output of each strain-gage circuit was recorded individually for a given load. Plots of electrical output vs. load input were made, and the slopes (V_{CD}/P) were determined. The load application test points on the surface of the stabilizer are shown in Fig. 3. The elastic axis was determined experimentally and is also shown in Fig. 3, together with the station location of the electric strain gages.

An analysis indicated that it would be sufficiently accurate to measure torque and moment arms parallel and perpendicular to the plane of symmetry of the airplane.

Computation of Summation Circuit Output

The gain factors were computed according to the equations already developed and static tests. The resulting gain factors are listed in Table 1.

Table 1
Comparison of Experimentally Determined and Calculated Gain Factors

Gain Factor	Determined from Test	Calculated
g_{1R}'	0.73	0.74
g_{2R}'	0.34	0.40
g_{3R}'	0.17	0.10
g_{1L}'	1.00	1.00
g_{2L}'	0.34	0.42
g_{3L}'	0.22	0.16

The data of Table 1 can now be used to predict the output of the summation circuit for loads applied at each point. Only the symmetrical case is shown here. Eq. (5) can be rewritten in a more convenient form by dividing through by P, multiplying all right-hand gain factors by g_R, and similarly for g_L. The equation then becomes

$$\frac{V}{P} = \frac{V_{CD1R}}{P} g_{1R}' + \frac{V_{CD2R}}{P} g_{2R}' + \frac{V_{CD3R}}{P} g_{3R}' + \frac{V_{CD1L}}{P} g_{1L}' + \frac{V_{CD2L}}{P} g_{2L}' + \frac{V_{CD3L}}{P} g_{3L}' \quad (16)$$

Substituting the values of the calculated gain factors in Table 1 and the values of V_{CDnR}/P and V_{CDnL}/P determined from static tests into Eq. (16), the resulting signal outputs of the circuit are plotted in Fig. 4. The points are plotted on a plan-view diagram of the horizontail tail at the points corresponding to the load application points. Lines of constant sensitivity are then drawn—therefore, the name "contour plots."

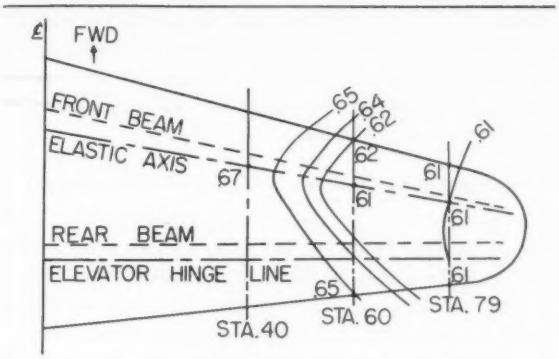

Fig. 4. Horizontal tail contour plot of sensitivities.

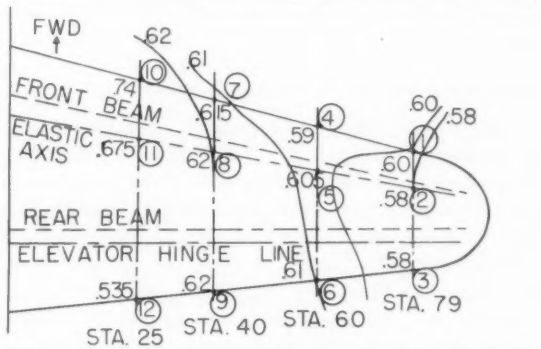

Fig. 5. Contour plot of sensitivities from test data for horizontal tail using calculated gain factors.

An inspection of the figure reveals that a 10 per cent variation in sensitivity is evident with sensitivity decreasing as the load moves outboard. This characteristic indicates insufficient correction for the effects of bending moment. The gains of the strain gages were adjusted experimentally to give improved results as explained below.

Experimental Check and Adjustment of Summation Circuits

First, a preliminary analysis of the effect of varying each gain setting on the entire summation circuit was made in order to minimize the number of trials and indicate the most logical way of adjusting the gain settings. It can be shown that a change in sensitivity, (V/P), of the summation circuit for changes in the gain factors can be expressed as follows:

$$d\left(\frac{V}{P}\right) = \frac{V_{CD1R}}{P} dg_{1R}' + \frac{V_{CD2R}}{P} dg_{2R}' + \frac{V_{CD3R}}{P} dg_{3R}' + \frac{V_{CD1L}}{P} dg_{1L}' + \frac{V_{CD2L}}{P} dg_{2L}' + \frac{V_{CD3L}}{P} dg_{3L}' \quad (17)$$

Eq. (17) shows the effect of varying the gain settings can easily be investigated using the unamplified channel sensitivities (V_{CD}/P) determined in the static tests for each loading point. Subsequent tests justified the results of the investigation and materially cut down the

guesswork in adjusting the gain setting of the circuit. The final gain factors giving the best results are listed in Table 1, together with the calculated gain factors. This table shows that calculations yield a reasonable approximation of the final values.

Comparison of Calculations with Experimental Results

A contour plot of the measured sensitivities using the experimentally adjusted gain factors is shown in Fig. 6, while a plot of the measured sensitivities using the calculated gain factors is shown in Fig. 5. A distinct improvement in uniformity of sensitivity is evident in Fig. 6 outboard of station 40. Although the sensitivities at station 25 depart considerably from those outboard of station 40, the average over the chord at station 25 is in line with results outboard of station 40.

Effects of Load Distribution on Accuracy

Fig. 6 shows that the summation circuit is somewhat sensitive to load position. The effect of this characteristic on accuracy of measurement was investigated for two extreme air-load distributions and was computed at ±2.4 per cent. This error is probably due to the neglect of torsion in the flange gages, as was brought out earlier in this paper. The only other major source of error detected was imperfect superposition, measured as ±1.9 per cent. Probable error was estimated to be ±3.1 per cent. Actual static tests indicated a maximum error of ±3.7 per cent, reasonably substantiating the estimated error.

Fortunately, in dynamic test work, incremental loads of short time duration are generally of interest; consequently, drift of electronic equipment does not affect data accuracy. However, where loads above a fixed datum are desired, drift can introduce large errors into the data. Therefore, equipment must be designed to maintain drift at a minimum.

Conclusions

A method has been developed for measuring structural loads on a complex airfoil surface without previous knowledge of load distribution through one channel of intelligence, which is particularly useful in the measurement of net loads in flight under dynamic conditions. In the specific case illustrated, a maximum error of ±3.7 per cent, determined in static tests, was incurred in the measurement of loads using this method.

The method eliminates laborious data reduction, and the equipment necessary to effect the summation of all electrical outputs into a single channel of information, requires little space.

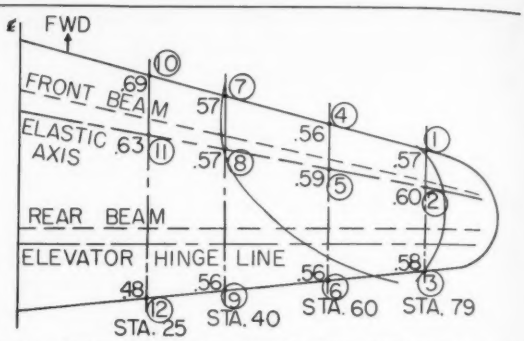

Fig. 6. Contour plot of sensitivities from test data for horizontal tail using experimentally adjusted gain factors.

References

[1] Ross, Ira G., *Bridge Circuit for Direct Reading of Shear from a Strain Gauge Rosette*, Curtiss Research Laboratory Report No. SG-105-S-2, September 1, 1943 (not available for general distribution).

[2] Milliken, Wm. F., Jr., *Progress in Dynamic Stability and Control Research*, Journal of the Aeronautical Sciences, Vol. 14, No. 9, pp. 493–519, September, 1947.

[3] Flight Research Department, *B-25J Progress Report, Proposal Covering Flight Testing Methods Using Automatic Control for the Measurement of Stability and Control Characteristics*, Curtiss-Wright Research Laboratory Report No. RLM-10, p. 16, December 21, 1945 (not available for general distribution).

[4] Walter, Maurice, *Instrumentation of an F-80A Airplane for Dynamic Stability and Tail Load Flight Tests. Part II—Method for Direct Measurement of Horizontal Tail and Elevator Shear Loads*, Cornell Aeronautical Laboratory Report No. TB-495-F-8, pp. 50, 60, 70, 72, 97, March 15, 1949 (not available for general distribution).

[5] Ross, Ira G., and Walter, Maurice, *Bridge Circuit for Direct Summation of Shear or Bending Moment Strain Gage Signals*, Cornell Aeronautical Laboratory FRM No. 37, January 6, 1948 (not available for general distribution).

Conical Flow Methods Applied to Uniformly Loaded Wings in Subsonic Flow*

SEYMOUR LAMPERT†

Ames Aeronautical Laboratory, N.A.C.A.

SUMMARY

Conical flow solutions for Laplace's equation are employed which yield expressions for the contour of uniformly loaded lifting surfaces at subsonic speeds. By properly superposing these conical flow fields, it is possible to determine the twist and camber for uniformly loaded wings having various aspect ratios, taper ratio, and sweepback. The solutions derived may also be used to investigate wing contours necessary for various types of spanwise and chordwise load distributions.

INTRODUCTION

IN A PREVIOUS PAPER,[1] Jones has demonstrated the possibility of extending the methods of conical flow analysis to wing problems at subsonic speeds. Jones derived expressions that give the subsonic pressure distribution over airfoils having various thickness distribution at zero lift. The method used is applied in the present paper to the calculation of the twist and camber of lifting surfaces of zero thickness. The usefulness of these conical flow solutions lies in the fact that they are well suited for treating problems involving sweptback wings.

SYMBOLS

x, y, z = Cartesian coordinates in the stream direction, across the stream, and in the vertical direction, respectively

x', y', z' = transformed coordinates correspond to $x \div \sqrt{1 - M^2}$, y, z, respectively

u, v, w = perturbation velocities in the stream direction, across the stream, and in the vertical direction, respectively

V = free-stream velocity

M = free-stream Mach Number

A.R. = aspect ratio (b^2/S)

b = wing span

c_0 = root chord

λ = taper ratio

Λ = angle of sweep of the leading edge

m = slope of leading edge (cot Λ)

m_t = slope of the trailing edge

m_s = slope of side edge

t = slope of any ray from the origin (y/x)

x_n, y_n = coordinates of the apex of a uniformly loaded sector

t_n = slope of a ray through the apex of a uniformly loaded sector, $(y - y_n)/(x - x_n)$

t_{nB} = slope of a ray through the apex of the uniformly loaded sector B, $(y - y_{nB})/(x - x_{nB})$

t_{nC} = slope of a ray through the apex of the uniformly loaded sector C, $(y - y_{nC})/(x - x_{nC})$

u_0 = value of streamwise perturbation velocity corresponding to the design lift coefficient, $4u_0/V = C_{L_0}$

u_1 = value of the streamwise perturbation velocity for a uniformly loaded sector of semi-infinite extent

u_2 = value of the streamwise perturbation velocity for the uniformly loaded triangular sector extending to infinity

u_3 = value of the streamwise perturbation velocity of the uniformly loaded sector for $0 \leq t \leq m$

u_4 = value of the streamwise perturbation velocity of the uniformly loaded sector for $m_s \leq t \leq m_t$

u_5 = value of the streamwise perturbation velocity of the uniformly loaded sector for $m \leq t \leq 1$

u_5' = image of u_5 reflected in the xz plane

w_j = the vertical perturbation velocity associated with u_j, where $j = 1, 2, 3, 4, 5$

w_T = vertical perturbation velocity for a sweptback tapered lifting surface

w_B, w_C = vertical perturbation velocities for sectors B and C of the tapered wing

z_j = contour associated with the vertical perturbation velocity w_j

z_T = contour associated with the vertical perturbation velocity w_T

ϵ = $(y + iz)/(x + \sqrt{x^2 + y^2 + z^2})$ conical variable

$\bar{\epsilon}$ = $(y - iz)/(x + \sqrt{x^2 + y^2 + z^2})$ complex conjugate of ϵ

ϵ_0 = value of ϵ which corresponds to m in the plane of the wing

ϵ_s = value of ϵ which corresponds to m_s in the plane of the wing

ξ = a variable used in the analysis, $2\epsilon/(1 - \epsilon^2)$

$Q_n(x)$ = Legendre function of the second kind,

$$Q_0(x) = \frac{1}{2} \log \frac{x + 1}{|x - 1|}$$

$$Q_1(x) = \frac{x}{2} \log \frac{x + 1}{|x - 1|} - 1$$

A_0 = $m(1 + \sqrt{1 + m^2})^{-1}$

A_s = $m_s(1 + \sqrt{1 + m_s})^{-1}$

ANALYSIS

If it is assumed that the stream lines deviate only slightly from rectilinear flow and that the rate of change of the area of the stream tube in the flow direction is small, problems of steady-state incompressible flow of a perfect fluid resolve themselves into finding solutions that satisfy Laplace's equation

$$S_{xx} + S_{yy} + S_{zz} = 0 \qquad (1)$$

Received January 10, 1950.

* The problem was suggested to the author by R. T. Jones, who also supplied helpful criticism.

† Aeronautical Research Scientist, 6- by 6-Ft. Supersonic Wind Tunnel, High Speed Research Division.

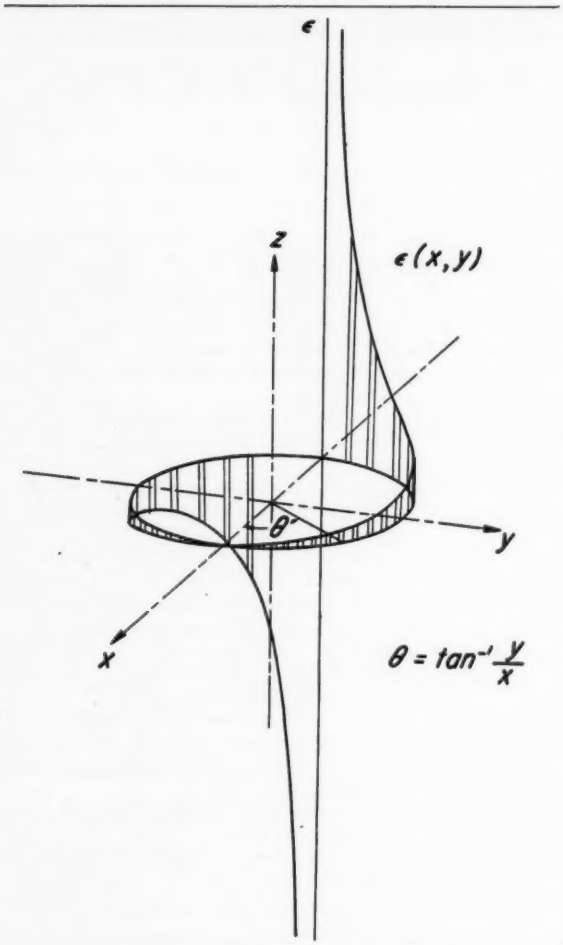

FIG. 1. Variation of ϵ with x and y in the chord plane of the wing ($z \to 0$).

where S is an analytic function of x, y, z, which describes any physical characteristic of a perfect fluid. It has been shown by Donkin[2] that, if S is homogeneous of degree zero—namely, constant along rays emanating from a fixed point in space—it may be expressed, in general, as

$$S = f\left(\frac{y + iz}{x + \sqrt{x^2 + y^2 + z^2}}\right) + g\left(\frac{y - iz}{x + \sqrt{x^2 + y^2 + z^2}}\right) \quad (2)$$

where f and g are each analytic functions of a single complex variable.

For the purposes of this paper, S has been chosen as the perturbation velocity in the x direction and may be expressed as

$$S = u = f(\epsilon) + g(\bar{\epsilon}) \quad (3)$$

where ϵ and $\bar{\epsilon}$ are the arguments of f and g in Eq. (2). Since f and g are both linearly independent solutions of Eq. (1), it is necessary only to work with $f(\epsilon)$ in this paper.

The Variable ϵ

Before entering the problem of finding the functions of ϵ which define a uniformly loaded lifting surface, it will be useful to investigate first the properties of the variable ϵ itself. We are concerned primarily with the variable near the chord plane of the wing ($z \to 0$). At $z = 0$, the value of ϵ is given by the relation

$$\epsilon = y/(x + \sqrt{x^2 + y^2}) \quad (4)$$

where ϵ is seen to be a pure real number constant along rays from the origin. In Fig. 1, the real value of ϵ as given in Eq. (4) is plotted vertically above the xy plane for all values of y/x.

An analytic transformation that will be useful in many cases for prescribing boundary conditions is

$$1/\xi = (1 - \epsilon^2)/2\epsilon \quad (5)$$

Since, in the plane of the wing where $\epsilon \to \bar{\epsilon}$ as $z \to 0$,

$$\frac{1}{\xi} \to \frac{1 - \epsilon\bar{\epsilon}}{2\epsilon} \to \frac{x}{y} \quad (6)$$

for all z

$$(1 - \epsilon\bar{\epsilon})/2\epsilon = x/(y + iz) \quad (7)$$

It is of interest to note here that the graphical construction relating ϵ and x, y, z as given in Fig. 2 is the subsonic analog of the Tschaplygin transformation given by Busemann[3] for the supersonic case. In Fig. 2, the center of the circle is chosen at the origin of the coordinate system, where ϵ and $1/\bar{\epsilon}$ are projected onto the xy plane in the same manner as shown by Busemann.

In the present paper, the variables ξ or ϵ will be employed interchangeably, depending on the problem. The variable ξ may be more convenient to use in most cases since the real part of ξ is just $y/x = t$, making it easier to prescribe boundary conditions in the plane of the wing.

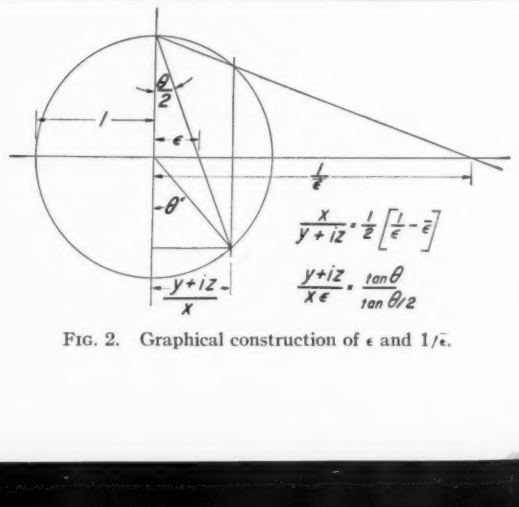

FIG. 2. Graphical construction of ϵ and $1/\bar{\epsilon}$.

Derivation of Uniformly Loaded Sectors

From the foregoing analysis, it is possible to define a conical flow field in the plane of the wing so that the loading prescribed will be uniform.

The boundary conditions that must be satisfied for a uniformly loaded surface extending over all values of y and positive x are:

(1) $u = 0$ for $x < 0$, which corresponds to $-1 > \epsilon > 1$ $(z \to 0)$.

(2) $u = u_0$ for $x \geq 0$ which corresponds to $-1 \leq \epsilon \leq 1$ $(z \to 0)$.

A function satisfying these conditions takes the form

$$u_1(\epsilon) = -\frac{u_0}{\pi}\text{R.P. } i \log \frac{\epsilon - 1}{\epsilon + 1} = 2\frac{u_0}{\pi}\text{R.P. } i\, Q_0(\epsilon) \tag{8}$$

where $Q_0(\epsilon)$ is the Legendre function of the second kind. The region over which the uniform load extends is shown in Fig. 3a for $z \to 0$, while the loading plotted against ϵ is given in Fig. 3b.

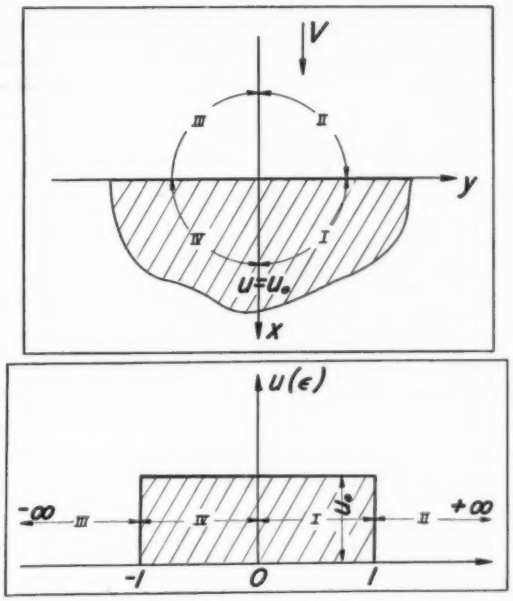

FIG. 3a (*top*). Uniformly loaded surface of semi-infinite extent $-\infty \leq t \leq \infty$. FIG. 3b (*bottom*). Plot of semi-infinite uniform load as a function of ϵ $(-1 \leq \epsilon \leq 1)$.

If the condition of irrotationality is utilized—namely,

$$\partial w/\partial x = \partial u/\partial z \tag{9}$$

the vertical velocity component that determines the shape of the lifting surface may be expressed in terms of ϵ as

$$dw = -(i/2)[(\epsilon^2 + 1)/\epsilon]\, du\ (\epsilon) \tag{10}$$

or

$$w = -\frac{i}{2}\int \frac{\epsilon^2 + 1}{\epsilon}\frac{du}{d\epsilon}\, d\epsilon + \text{constant} \tag{11}$$

Substituting Eq. (8) into Eq. (11), the vertical velocity distribution may be calculated as

$$w_1(\epsilon) = -\frac{u_0}{\pi}\log\frac{1 - \epsilon^2}{\epsilon} + \text{constant} \tag{12}$$

or

$$w_1(\xi) = (u_0/\pi)\log\xi + \text{constant} \tag{13}$$

The real part of Eq. (13) evaluated in the plane of the wing becomes simply

$$w_1(t) = (u_0/\pi)\log|t| + \text{constant} \tag{14}$$

The constant as given in Eq. (14) is allowed to remain arbitrary, since the boundary conditions will be satisfied by the superposition of solutions of the type given in Eq. (8).

The vertical velocity as given in Eq. (14) is seen to be infinite along both the x and y axis. The infinity along the y axis $(x = 0)$ is of the type normally associated with the two-dimensional camber shape of uniformly loaded wings. The infinity along the positive x axis, however, is not characteristic of cylindrical flow. From the very nature of the solution, though, there must exist a singularity of this form along the x axis, which leads one to believe that the solution for the shape of a uniformly loaded lifting surface covering half the xy plane is not unique. However, it can be shown that, by the proper superposition of the solutions given by Eq. (8), the two-dimensional or cylindrical vertical velocity field corresponding to a wing of finite chord may be realized. If one lifting sector of the type given in Eq. (8) is placed along the line $x = -1$ and another of equal and opposite strength is placed at $x = +1$, the result is a uniformly loaded infinite wing of chord 2. The distance and position of the lifting elements along the x axis is arbitrary, and the values of x were taken at ± 1 for convenience in evaluating the vertical velocity distribution. The resultant distribution for the vertical component becomes

$$w = -\frac{u_0}{\pi}\log\left|\frac{x + 1}{x - 1}\right| = -2\frac{u_0}{\pi}Q_0(x) \tag{15}$$

which is the well-known two-dimensional solution for a uniformly loaded thin lifting wing. It might be pointed out that, by keeping the leading edge fixed at $x = -1$ and allowing the trailing edge to move off a large distance downstream, the nature of the solution remains cylindrical. The contour resulting from Eq. (15) may be obtained by the following relation:

$$V\left(\frac{dz}{dx}\right) = [w(x)]_{z \to 0} = -2\frac{u_0}{\pi}Q_0(x) \tag{16}$$

which requires that the flow be parallel to the surface at the surface. Integrating Eq. (16) with respect to x gives the contour as

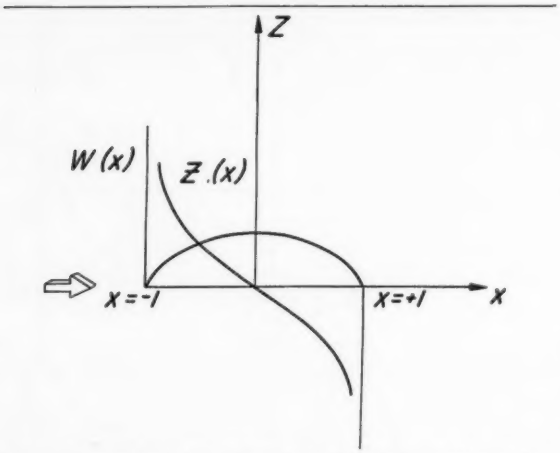

FIG. 4. Camber and slope of a uniformly loaded two-dimensional lifting surface for $2u_0/V = 0.04\pi$.

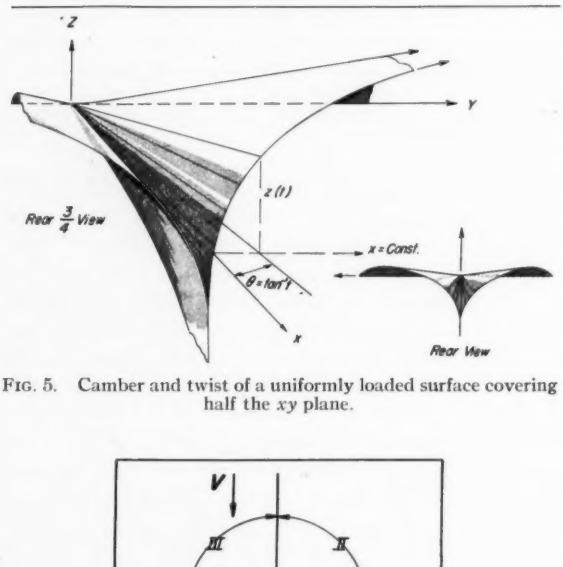

FIG. 5. Camber and twist of a uniformly loaded surface covering half the xy plane.

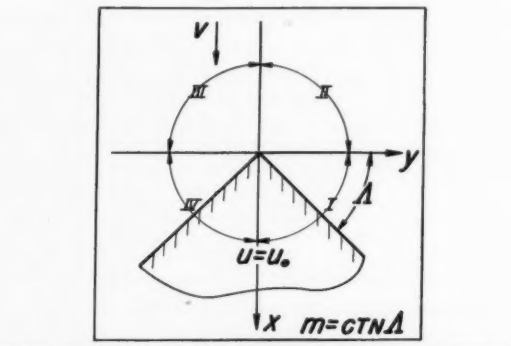

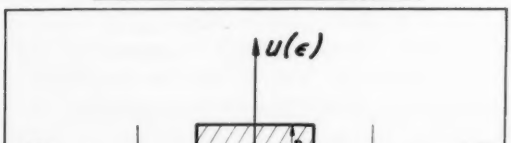

FIG. 6a (*top*). Uniformly loaded surface for $-m \leq t \leq m$. FIG. 6b (*bottom*). Plot of uniform load in the ϵ plane for $-\epsilon_0 \leq \epsilon \leq \epsilon_0$.

$$z(x) = -\frac{u_0}{\pi V}[2Q_1(x) + \log|x^2 - 1|] \qquad (17)$$

which is shown in Fig. 4a plotted against x. It is of interest to compare the cylindrical nature of the contour as given in Eq. (17) for the finite chord wing with the conical-type contour

$$z_1(x, t) = -\frac{u_0 x}{\pi V}\left(\log\frac{1}{|t|} + \text{constant}\right) \qquad (18)$$

resulting from integrating the vertical velocity distribution given in Eq. (14) for a uniformly loaded surface covering half the xy plane. The contour as given in Eq. (18) is shown in Fig. 5 and is seen to be a linearly increasing function of x along conical rays emanating from the origin.

It will be noted that Eq. (15) gives an infinite vertical velocity at the leading and trailing edges as a consequence of the fact that a finite load is carried at the airfoil leading and trailing edges. The flow experiences theoretical infinite accelerations at the leading and trailing edges which are, of course, impossible in a real fluid. It is to be expected, therefore, that the theoretical loading will not be realized in the immediate vicinity of the leading and trailing edges.

Uniformly Loaded Sweptback Wing

Infinite Span.—In a manner similar to that employed for finding the shape of the two-dimensional wing, it is possible to determine the proper shape of a sweptback wing of infinite span supporting a uniform load.

The boundary conditions for a uniformly loaded infinite triangular sector are

(1) $u = 0$ for $-m > t > m$, where m is the slope of the leading edge. In the ϵ plane, this boundary condition is $-\epsilon_0 > \epsilon > \epsilon_0$ $(z \to 0)$.

(2) $u = u_0$ for $-m \leq t \leq m$, which corresponds to $-\epsilon_0 \leq \epsilon \leq \epsilon_0$ $(z \to 0)$.

The function satisfying these boundary conditions is

$$u_2(\epsilon, \epsilon_0) = -\frac{u_0}{\pi}\,\text{R.P.}\; i \log\frac{\epsilon - \epsilon_0}{\epsilon + \epsilon_0}$$

$$= -2\frac{u_0}{\pi}\,\text{R.P.}\; i\, Q_0\left(\frac{\epsilon}{\epsilon_0}\right) \qquad (19)$$

The regions over which this function is uniform are shown in Fig. 6a, and the distribution as a function of ϵ is plotted in Fig. 6b.

It can be seen that Eq. (8) is merely a special case of Eq. (19), where the sweepback angle Λ approaches zero. The vertical velocity distribution resulting from Eq. (19) obtained by integrating Eq. (11) is

$$w_2(\epsilon, \epsilon_0) = -\frac{u_0}{\pi}\left[\frac{1+\epsilon_0^2}{2\epsilon_0}\log(\epsilon_0^2-\epsilon^2) - \frac{1}{\epsilon_0}\log\epsilon\right] + \text{constant} \tag{20}$$

The real part of Eq. (20) evaluated in the plane of the wing becomes

$$w_2(t, m) = -\frac{u_0}{\pi}\left[\frac{\sqrt{1+m^2}}{m}\log\left|\frac{m^2}{(1+\sqrt{1+m^2})^2} - \frac{t^2}{(1+\sqrt{1+t^2})^2}\right| + \frac{1+\sqrt{1+m^2}}{m}\sinh^{-1}\frac{1}{|t|}\right] + \text{constant} \tag{21}$$

where $m = \cot\Lambda$ is the slope of the leading edge and $t = y/x$ is any ray from the apex. The vertical velocity distribution has a logarithmic infinity along the leading edge and along the x axis as was anticipated. These conditions are similar to those obtained previously for a straight leading edge. However, in this case, the infinity along the x axis does not disappear under superposition of solutions.

The result conforms with previous results obtained at supersonic speeds for a uniformly loaded sweptback wing with subsonic leading edges.[4] It is possible, however, to eliminate the impractically high twist near the root chord if the loading is allowed to reduce slightly from the uniform character in the region of the root. Baldwin[5] has demonstrated how this can be done for triangular wings with subsonic leading edges in supersonic flow.

If the apices of two lifting surfaces of equal loading but of opposite sign are placed at $x = \pm 1$, $y = 0$, the result will be a sweptback wing of infinite span with chord 2 supporting a uniform load. The solution may be characterized as

$$w = -[w_2(t_1, m) - w_2(t_2, m)] \tag{22}$$

The values for t_1 and t_2 to be substituted in Eq. (22) are

$$t_1 = y/(x+1); \quad t_2 = y/(x-1) \tag{23}$$

For a tapered lifting surface Eq. (22) may be rewritten as

$$w_T = -[w_2(t_1, m) - w_2(t_2, m_t)] \tag{24}$$

where m_t is the slope of the trailing edge.

The contour corresponding to Eq. (21) may be given as

$$z_2(t, m, x) = -\frac{u_0 x}{V\pi}\left[\frac{1+\sqrt{1+m^2}}{m}\left(\sinh^{-1}\frac{1}{|t|} - \sqrt{1+t^2}\right) + \frac{\sqrt{1+m^2}}{m}\left\{\log\left|A_0^2 - \frac{t^2}{(1+\sqrt{1+t^2})^2}\right| + \frac{t^2}{1+\sqrt{1+t^2}} + \frac{2t}{m}Q_0\left[\frac{A_0}{t}(1+\sqrt{1+t^2})\right]\right\} + \text{constant}\right] \tag{25}$$

where $A_0 = m(1+\sqrt{1+m^2})^{-1}$ and the contour of the sweptback wing of constant chord is given by

$$z = -[z_2(t_1, m) - z_2(t_2, m)] \tag{26}$$

and the contour of the tapered wing is given by

$$z_T = -[z_2(t_1, m) - z_2(t_2, m_t)] \tag{27}$$

Eq. (26) is plotted in Fig. 7 for a 45° sweptback wing of constant chord.

Finite Plan Forms.—The method outlined above may be used to solve for the shape of tapered wings of finite span. The treatment consists of superimposing uniformly loaded surfaces so as to cancel all lift outside the confines of the wing plan form so that the correct boundary conditions are met. For example, a finite sweptback wing of given span may be obtained from the uniformly loaded wing of infinite span of the pre-

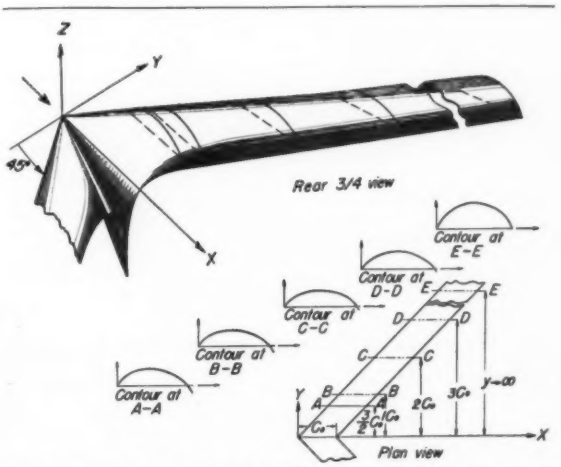

FIG. 7. Camber and twist of a uniformly loaded 45° sweptback wing for $2u_0/V = 0.04\pi$.

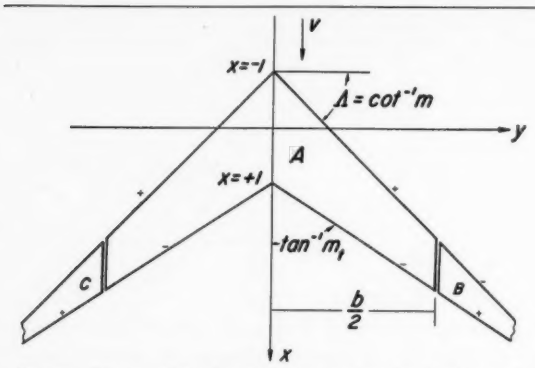

FIG. 8. Superposition for obtaining a sweptback wing of A.R. $= (b/2)[1 + (1/2)(\lambda - 1)]^{-1}$ and $\lambda = 1 - (b/4)[(1/m) - (1/m_1)]$.

vious section by canceling the loading beyond the wing tips as shown in Fig. 8.

The vertical velocity component for region A in Fig. 8 corresponds to the value given in Eq. (24). It remains now to find the vertical velocity components that result from superimposing constant load sectors of equal and opposite sign, respectively, at the leading and trailing edges of the tip station.

The solution for these sectors, which satisfies the following boundary conditions (1) $u = 0$ for $0 > t > m$ or $0 > \epsilon > \epsilon_0$ $(z \to 0)$ and (2) $u = u_0$ for $0 \leq t \leq m$ or $0 \leq \epsilon \leq \epsilon_0$ $(z \to 0)$, takes the form

$$u_3(\epsilon, \epsilon_0) = -\frac{u_0}{\pi} \text{R.P. } i \log \frac{\epsilon - \epsilon_0}{\epsilon} \tag{28}$$

The region over which this function is a constant is shown in Fig. 9. The corresponding vertical velocity component is given as

$$w_3(t, m) = -\frac{u_0}{2\pi}\left(\frac{2\sqrt{1+m^2}}{m}\log\left|A_0 - \frac{t}{1+\sqrt{1+t^2}}\right| - \frac{1+\sqrt{1+m^2}}{m}\log\left|\frac{t}{1+\sqrt{1+t^2}}\right| + \frac{1+\sqrt{1+t^2}}{t}\right) + \text{constant} \tag{29}$$

and the contour resulting from integrating Eq. (29) with respect to x is given by

$$z_3(t, m, x) = -\frac{u_0 x}{2\pi V}\left[\frac{2\sqrt{1+m^2}}{m^2}(m-t)\log\left|A_0 - \frac{t}{1+\sqrt{1+t^2}}\right| + \left(\frac{t}{2} + \frac{1}{A_0} + \frac{t}{m}\frac{\sqrt{1+m^2}}{A_0}\right)\sinh^{-1}\times \frac{1}{|t|} + \frac{(1+\sqrt{1+t^2})^2}{4t} - \frac{\sqrt{1+t^2}}{A_0} + \frac{t^2}{m}\frac{\sqrt{1+m^2}}{1+\sqrt{1+t^2}} + \text{constant}\right] \tag{30}$$

In sectors B and C, respectively, the vertical velocity components are given in the form

$$w_B = -[w_3(t_{1B}, m) - w_3(t_{2B}, m_1)] \tag{31}$$

where

$$t_{1B} = \frac{y - (b/2)}{x - (b/2m) + 1}; \quad t_{2B} = \frac{y - (b/2)}{x - (b/2m_1) - 1} \tag{32}$$

and

$$w_C = -[w_3(t_{1C}, -m) - w_3(t_{2C}, -m_1)] \tag{33}$$

where

$$t_{1C} = \frac{y + (b/2)}{x - (b/2m) + 1}; \quad t_{2C} = \frac{y + (b/2)}{x - (b/2m_1) - 1} \tag{34}$$

The contours corresponding to the vertical velocities in Eqs. (31) and (33) are

$$z_B = -[z_3(t_{1B}, m) - z_3(t_{2B}, m_1)] \tag{35}$$

and

$$z_C = -[z_3(t_{1C}, -m) - z_3(t_{2C}, -m_1)] \tag{36}$$

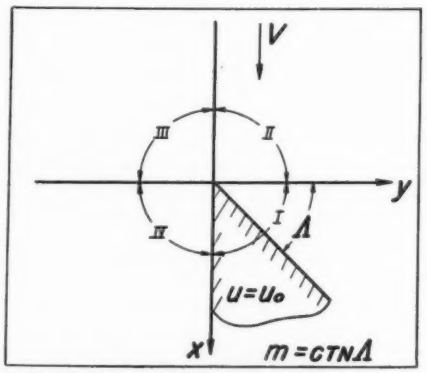

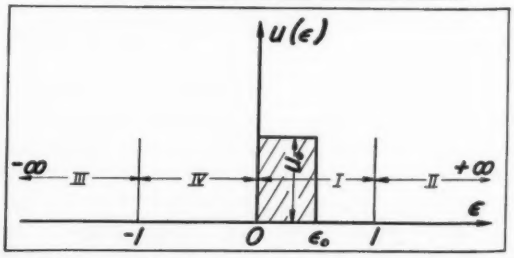

FIG. 9a (*top*). Uniformly loaded sector for $0 \leq t \leq m$. FIG. 9b (*bottom*). Plot of uniform load in the ϵ plane for $0 \leq \epsilon \leq \epsilon_0$

The slope of the surface for the complete wing may therefore be written as

$$V(dz/dx) = w_T - (w_B - w_C) \tag{37}$$

where the contour will be

$$z = z_T - (z_B - z_C) \tag{38}$$

It should be pointed out here that in actual design practice it will not be possible to maintain a uniform loading all the way to a streamwise tip, and it is therefore desirable to allow the loading to be rounded off at the tip in such a way that impractical wing twist near the tip may be avoided.

This treatment of uniformly loaded wings may be used to obtain the twist and camber for a variety of wings of different aspect ratios, taper ratios, and sweepback. The rectangular wing, for example, is the limiting case of the sweptback wing described above. It can be shown that, if the sweepback of the leading edge be allowed to approach zero ($m \to \infty$), then Eq. (38) describes the contour of the surface of a rectangular wing of aspect ratio $b/2$.

Wings with Raked Tips.—In order to obtain the contour of a wing having a raked tip, it is necessary, as before, to define a uniformly loaded sector that describes a uniform load over the region shown in Fig. 10, where $u = u_0$ for $m_s \leq t \leq m$ or $\epsilon_s \leq \epsilon \leq \epsilon_0$. The function describing these conditions is

$$u_4(\epsilon, \epsilon_0, \epsilon_s) = -\frac{u_0}{\pi}\,\text{R.P.}\; i \log \frac{\epsilon - \epsilon_0}{\epsilon - \epsilon_s} \tag{39}$$

If sectors of the form given in Eq. (39) are superposed at the tip station in the same way as previously outlined for the streamwise tips, it is possible then to find the vertical velocity corresponding to the resultant streamwise component as

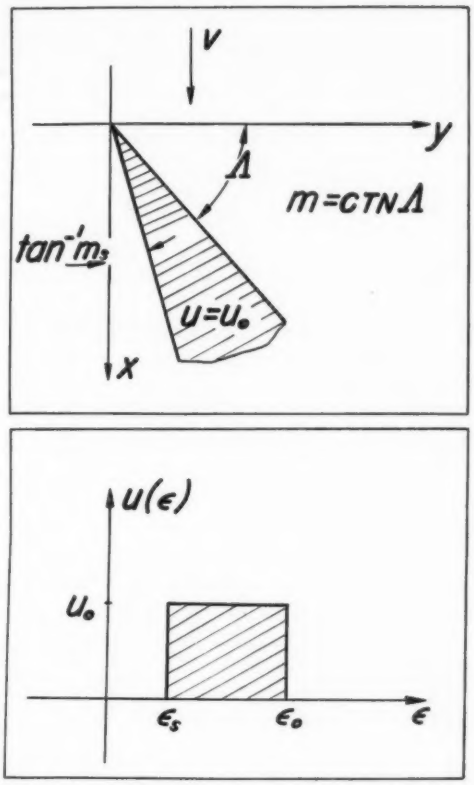

FIG. 10a (*top*). Uniformly loaded sector for $m_s \leq t \leq m$. FIG. 10b (*bottom*). Uniform load in the ϵ plane for $\epsilon_s \leq \epsilon \leq \epsilon_0$.

$$w_4(t, m_s, m) = \frac{u_0}{2\pi}\left(\frac{2\sqrt{1+m^2}}{m}\log\left|A_0 - \frac{t}{1+\sqrt{1+t^2}}\right| - \frac{2\sqrt{1+m_s^2}}{m_s}\log\left|\frac{t}{1+\sqrt{1+t^2}} - A_s\right| + \left|\frac{1}{A_s} - \frac{1}{A_0}\right|\sinh^{-1}\frac{1}{|t|}\right) + \text{constant} \tag{40}$$

and the contour associated with Eq. (39) will be

$$z_4(t, m_s, m) = -\frac{u_0 x}{4\pi V}\left\{-\frac{2\sqrt{1+m^2}}{m^2}(m-t)\log\left|A_0 - \frac{t}{1+\sqrt{1+t^2}}\right| + \frac{2\sqrt{1+m_s^2}}{m_s^2}(t-m_s)\times \log\left|\frac{1}{1+\sqrt{1+t^2}} - A_s\right| + \left[t\left(\frac{\sqrt{1+m^2}}{mA_0} + \frac{\sqrt{1+m_s^2}}{m_s A_s}\right) - \left(\frac{1}{A_s} - \frac{1}{A_0}\right)\right]\sinh^{-1}\frac{1}{|t|} + \left(\frac{1}{m_s} - \frac{1}{m}\right)\sqrt{1+t^2} + \left(\frac{\sqrt{1+m^2}}{m} + \frac{\sqrt{1+m_s^2}}{m_s}\right) + \text{constant}\right\} \tag{41}$$

Triangular Plan Form.—The triangular plan form may be achieved without much difficulty by canceling the lift behind a uniformly loaded triangular sector described in Eq. (19). The uniformly loaded sectors necessary for canceling the loads, behind the triangular sector, take the form

$$u_5(\epsilon, \epsilon_0) = -\frac{u_0}{\pi}\,\text{R.P.}\; i \log \frac{\epsilon - 1}{\epsilon - \epsilon_0} \tag{42}$$

where $u = u_0$ for $\epsilon_0 \leq \epsilon \leq 1$ or $m \leq t \leq \infty$. In Fig. 11a,

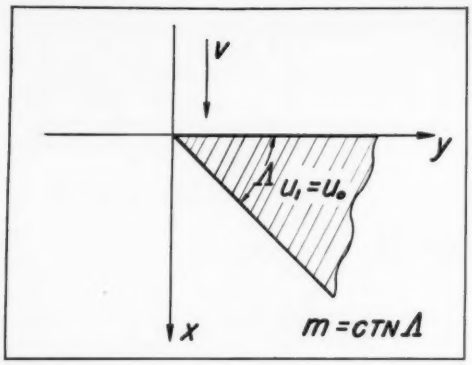

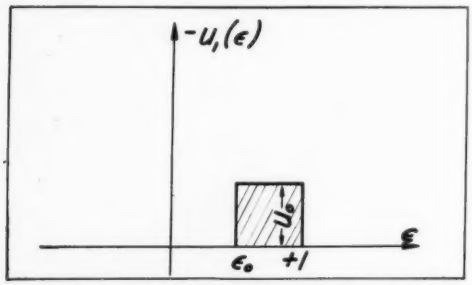

FIG. 11a (*top*). Uniformly loaded wing for $m \leq t \leq \infty$. FIG. 11b (*bottom*). Plot of uniform load in ϵ plane for $\epsilon_0 \leq \epsilon \leq 1$.

Eq. (42) is shown in the physical plane, and, in Fig. 11b, it is given in the ϵ plane. The vertical velocities and the contours associated with Eq. (42) may be obtained from Eqs. (40) and (41), respectively, if m_s is allowed to approach infinity and A_s to approach unity.

The required superposition for the triangular wing may be characterized as

$$u = u_2(x, y) - u_1(x - c_0, y) + u_5[x - c_0, y - b/2)] + u_5'[x - c_0, y + (b/2)] \quad (43)$$

where u_5' is the mirror image of u_5. Its formula is given by

$$u_5' = \frac{u_0}{\pi} \text{ R.P. } i \log \frac{\epsilon + 1}{\epsilon + \epsilon_0} \quad (44)$$

The vertical velocity component corresponding to Eq. (43) is given as

$$w = w_2(x, y) - w_1(x - c_0, y) + w_5[x - c_0, y - (b/2)] + w_5'[x - c_0, y + (b/2)] \quad (45)$$

and the contour will then be

$$z = z_2(x, y) - z_1(x - c_0, y) + z_5[x - c_0, y - (b/2)] + z_5'[x - c_0, y + (b/2)] \quad (46)$$

The superposition described in Eqs. (43), (45), and (46) is shown in Fig. 12.

PRANDTL-GLAUERT TRANSFORMATION

The solutions derived in the previous sections are those that satisfy Laplace's equation [Eq. (1)], a well-known linear differential equation of mathematical physics. Solutions of this equation are of special interest to aerodynamicists, because it can be shown to be a special form of the linearized potential equation for compressible flow given as

$$(1 - M^2)S_{xx} + S_{yy} + S_{zz} = 0 \quad (47)$$

Eq. (47) reduces to Laplace's equation if the Mach Number of the flow is zero or if, in the case where the Mach Number is greater than zero and less than unity, the following transformation is applied to the coordinate system:

$$x' = -x/\sqrt{1 - M^2}; \quad y' = y; \quad z' = z$$

in which case Eq. (47) becomes

$$S_{x'x'} + S_{y'y'} + S_{z'z'} = 0 \quad (48)$$

The solutions for S are now harmonic functions of the variables x', y', z'. It is evident, therefore, that the solutions obtained in the preceding sections for $M = 0$ can be used to find solutions at Mach Number M. In order to find the vertical coordinates z of a cambered wing to support a specified uniform load at M, the procedure is to stretch the x coordinate in the equations for $M = 0$ by the factor $1/\sqrt{1 - M^2}$. If the value of the slopes (i.e., w/V) for the wing in incompressible flow ($M = 0$) are transferred unchanged to the corresponding points on the wing for Mach Number M, then the streamwise component of the velocity u (pressure) is increased by the factor $1 \div \sqrt{1 - M^2}$. On the other hand, if it is desired to maintain a given u (i.e., pressure) at corresponding points of the two wings, then the slopes of the wing at Mach Number M are to be decreased by the factor $\sqrt{1 - M^2}$ of the values of the slopes of the $M = 0$ wing.

To illustrate, Eq. (17) given for $M = 0$ will be transformed to give the camber of a wing at Mach Number M to support a specified uniform load u_0.

(*Continued on page 138*)

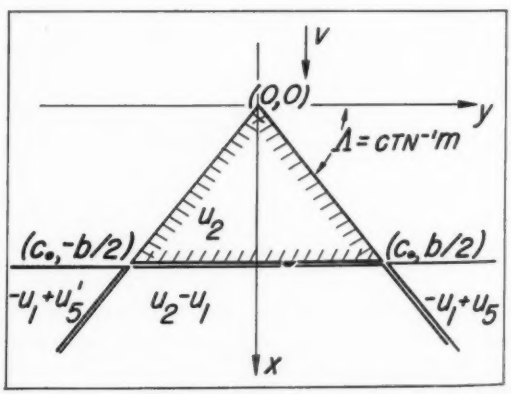

FIG. 12. Superposition for obtaining a triangular wing of A.R. = $2b/c_0$.

Calculation of Thermal Stresses in a Wedge-Shaped Wing*

GEORGE H. EISENHARDT† AND WARREN M. ROHSENOW‡

Massachusetts Institute of Technology

SUMMARY

A method for calculating thermal stresses is presented and applied to a solid symmetrical double-wedge steel wing flying at an altitude of 50,000 ft. The wing, after flying steadily at a Mach Number of 1.4 and having a uniform temperature distribution of 531.6°F. absolute, is accelerated at a constant rate of one Mach Number per 30 sec. until a Mach Number of 6.0 is reached. Thermal stresses at the instant the wing reaches a Mach Number of 6.0 are calculated using the elastic properties of steel at room temperature. An interpolation method is presented for estimating the thermal stress during the acceleration.

NOMENCLATURE

A	=	area, sq.in.
C_0, C_1, C_2	=	arbitrary constants
E	=	Young's modulus lbs. per sq.in.
E'	=	$E/(1-\nu^2)$
F_n	=	$A_n(T-T_m)_n$
I_x	=	moment of inertia of wing cross-sectional area about the x-axis
I_y	=	moment of inertia of wing cross-sectional area about the y-axis
K	=	$-(\alpha E+\nu'\alpha' E')$
M	=	Mach Number, wing velocity ÷ sound velocity in main stream
T	=	actual temperature at a point
T_i	=	initial temperature of the wing = 531.6°F. abs.
T_m	=	mean temperature of the wing = $(1/A)\int_A T\,dA$
$T_{max.}$	=	temperature at a point at $M = 6.0$ immediately following the acceleration
α	=	linear thermal coefficient of expansion, in. per in. °F.
α'	=	$(1+\nu)\alpha$
∇^2	=	$(\partial^2/\partial x^2)+(\partial^2/\partial y^2)$
ν	=	Poisson's ratio
σ	=	normal stress, lbs./in.²
$\sum$	=	$(T-T_i)/(T_{max.}-T_i)$, stress parameter
$\sum_0^n$	=	summation of terms from 0 to n
τ	=	shear stress, lbs./in.²
θ_a	=	time from $M = 1.4$, sec.
$\theta_{max.}$	=	total time from $M = 1.4$ to 6.0, sec.
θ	=	$\theta_a/\theta_{max.}$

INTRODUCTION

CURRENT TRENDS IN AIRCRAFT and guided-missile flight indicate an ever increasing interest in high-speed performance. At extremely high flight speeds, frictional effects in the boundary layer produce extremely high temperatures and temperature gradients within the aircraft structure. In order to appraise the severity of the problem, an investigation of the resulting thermal stresses was undertaken. Although a specific example is presented, the method of attack used is applicable to a wide variety of such problems. The specific case treated here is a diamond airfoil for which the time-space temperature distribution is known.[1] The numerical procedure utilized, although cumbersome, readily yields interpretable results and can be applied to bodies with boundary curves that are ill-suited for analytic analysis. No attempt was made to consider plastic flow in the wing, although the stresses computed in some portions of the wing on an assumption of perfect elasticity are beyond the elastic limit of any suitable material.

EXAMPLE TREATED

The specific case considered was that of a solid symmetrical double-wedge wing shown in Fig. 1 of the following size:

Chord length = 5.5 ft. and thickness/chord ratio = 8 per cent

The following assumptions are made concerning aerodynamic, thermal, and structural conditions:

(1) Acceleration is uniform and at a rate of one Mach Number per 30 sec. from $M = 1.4$ to 6.0.

(2) The supersonic flow of air by the wing is assumed to be two-dimensional, independent of the span. Fig. 2 shows the flow pattern around the wing, with shock waves at the leading and trailing edges and an expansion wave at the mid-chord.

(3) The wing is made of steel with constant values of the thermal conductivity, specific heat, density,

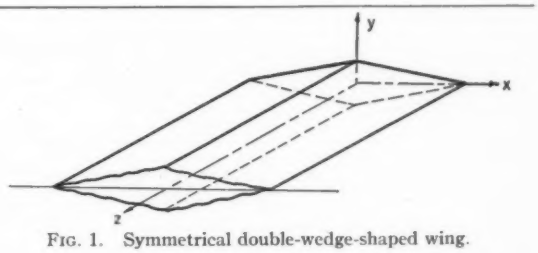

FIG. 1. Symmetrical double-wedge-shaped wing.

Received January, 1950.

* This paper represents a portion of the work carried out for the U.S. Air Force under Contract No. W33-038 ac-17239 and is an advance release of a portion of U.S.A.F. Technical Report No. 5786.

† Teaching Assistant.

‡ Assistant Professor of Mechanical Engineering.

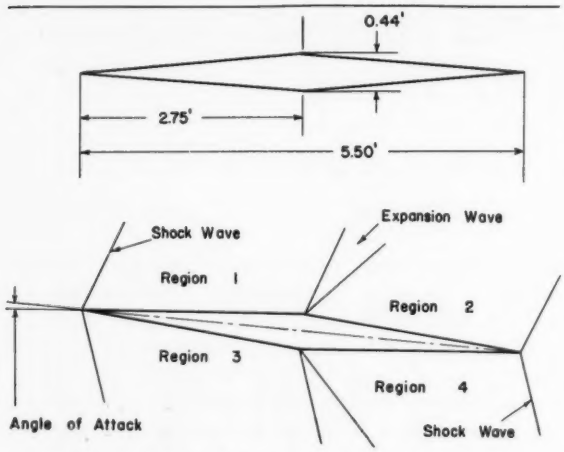

FIG. 2. Airfoil and flow pattern of wedge-shaped wing.

modulus of elasticity, thermal expansion coefficient, and Poisson's ratio.

(4) Spanwise heat transfer is negligible.

(5) Heat transfer by radiation to or from the wing surface is neglected.

(6) The flight of the wing is at a fixed altitude of 50,000 ft.

(7) The flight of the wing begins with a uniform wing temperature of 531.6°F. absolute at a Mach Number of 1.4.

(8) The root of the wing is rigidly built into the fuselage so that the root section is at all times plane.

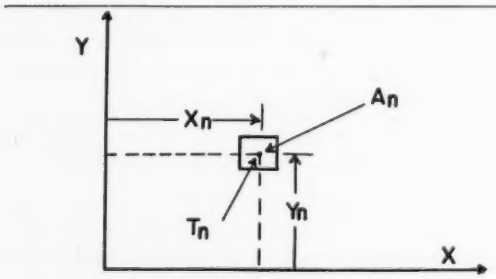

FIG. 3. Notation for increment procedure.

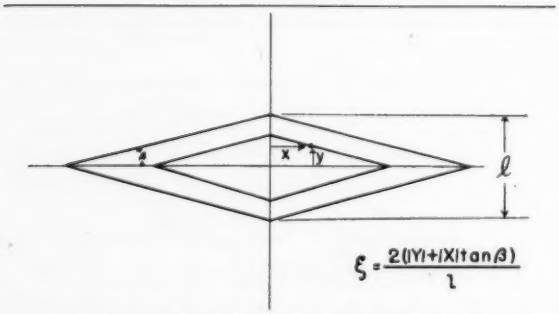

FIG. 4. Definition of coordinates for interior points in the wing.

(9) The span of the wing is reasonably large with respect to the chord.

Assumptions (8) and (9) permit computation of thermal stresses at the root of the wing which correspond to those at a large distance from the free end of a semi-infinite wing.

Temperature Distribution

The resulting temperature distribution immediately after acceleration to a Mach Number of 6 is contained in reference 1 and is reproduced here in Chart A of Fig. 5. The solution for the two-dimensional temperature distribution was accomplished by a stepwise procedure. Attempts to obtain an exact analytic solution failed. It was found that a good empirical approximation of the temperature distribution could be obtained by means of a product series that converged slowly; hence, an analytic solution for the thermal stress distribution became impractical.

Analysis

Consider a section of the infinite wing with axes defined as shown in Fig. 1. Although the temperature distribution exists only in numerical form, let us consider the function $T(x, y)$ as representing that distribution. It will be treated mathematically as a continuous function with continuous first and second derivatives. Since the problem under consideration is one of plane strain, the following quantities are zero, ϵ_z, τ_{xz}, τ_{yz}, and the equilibrium and Hookian equations become[2]

$$\left.\begin{aligned} &(\partial\sigma_x/\partial x) + (\partial\tau_{xy}/\partial y) = 0 \\ &(\partial\sigma_y/\partial y) + (\partial\tau_{xy}/\partial x) = 0 \\ &\partial\sigma_z/\partial z = 0 \\ &\epsilon_x = (1/E')\,(\sigma_x - \nu'\sigma_y) + \alpha' T \\ &\epsilon_y = (1/E')\,(\sigma_y - \nu'\sigma_x) + \alpha' T \\ &0 = \sigma_z - \nu(\sigma_x + \sigma_y) + E\alpha T \end{aligned}\right\} \quad (1)$$

Utilizing the condition of derivative continuity the following compatability equation is obtained:

$$\frac{\partial^2(\sigma_x + \sigma_y)}{\partial x^2} + \frac{\partial^2(\sigma_x + \sigma_y)}{\partial y^2} = \nabla^2(\sigma_x + \sigma_y) = -\alpha' E' \nabla^2 T \quad (2)$$

Combining this with the third of the Hookian equations results in the following equation for the stresses in the z direction:

$$\nabla^2\sigma_z = (-\alpha E - \nu'\alpha' E')\nabla^2 T = K\nabla^2 T \quad (3)$$

where

$$K = -(\alpha E + \nu'\alpha' E')$$

The solution of this equation has two parts; the first, or particular, solution is simply

$$\sigma_z = KT \quad (4)$$

The second, or homogeneous, solution is one that satisfies the equation

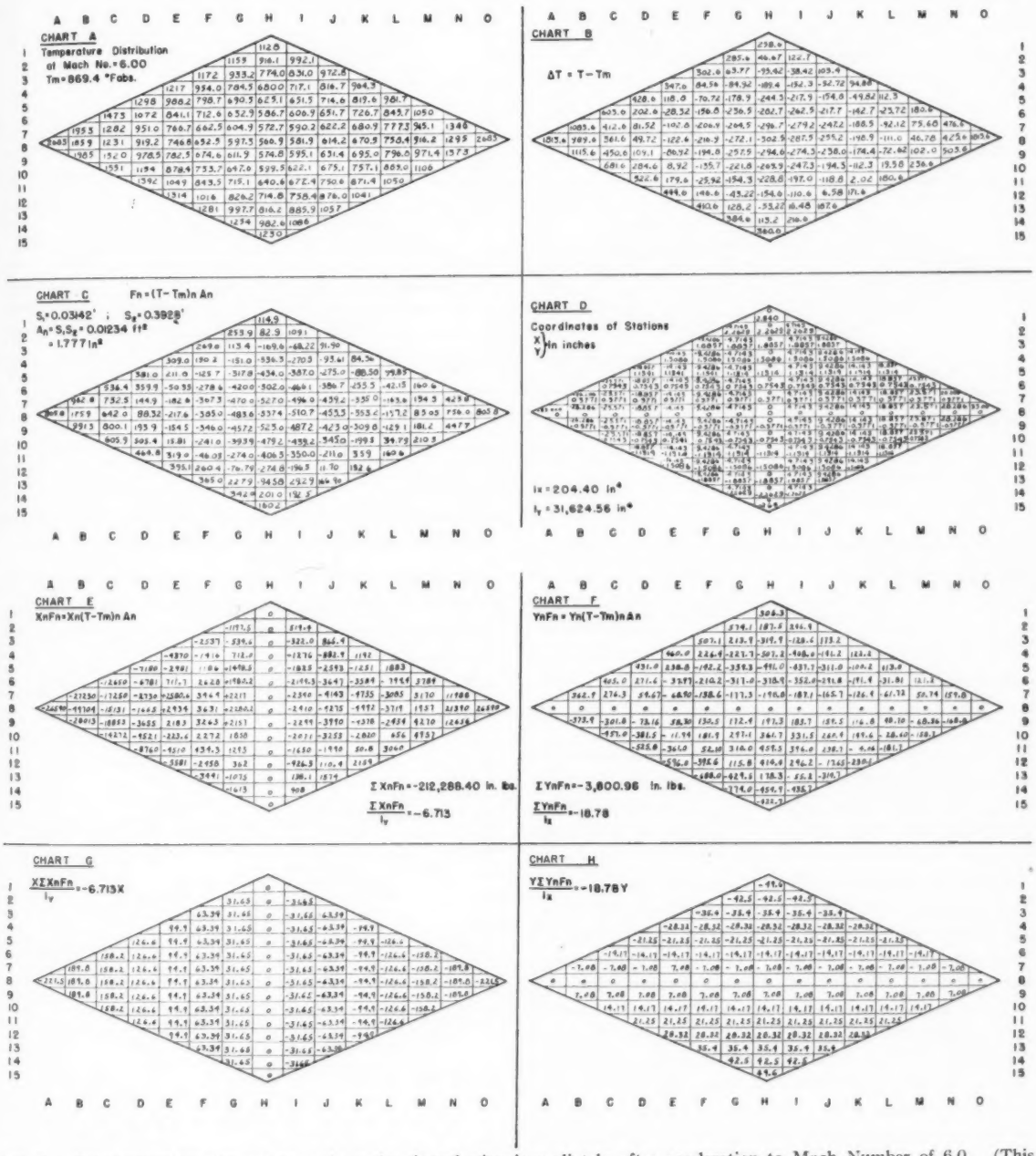
CHART A
Temperature Distribution
at Mach No. = 6.00
Tm = 869.4 °Fabs.
CHART B
ΔT = T − Tm
CHART C
Fn = (T − Tm) n An
S1 = 0.03462' ; S2 = 0.3928'
An = S1S2 = 0.01294 ft²
= 1.777 in²
CHART D
Coordinates of Stations
(X, Y) in inches
Ix = 204.40 in⁴
Iy = 31,624.56 in⁴
CHART E
XnFn = Xn(T − Tm) n An
ΣXnFn = −212,288.40 in. lbs.
ΣXnFn / Iy = −6.713
CHART F
YnFn = Yn(T − Tm) n An
ΣYnFn = −3,800.96 in. lbs.
ΣYnFn / Ix = −18.78
CHART G
XΣXnFn / Iy = −6.713X
CHART H
YΣYnFn / Ix = −18.78Y

FIG. 5. Calculations for thermal stress in wedge-shaped wing immediately after acceleration to Mach Number of 6.0. (This figure is concluded on page 118.)

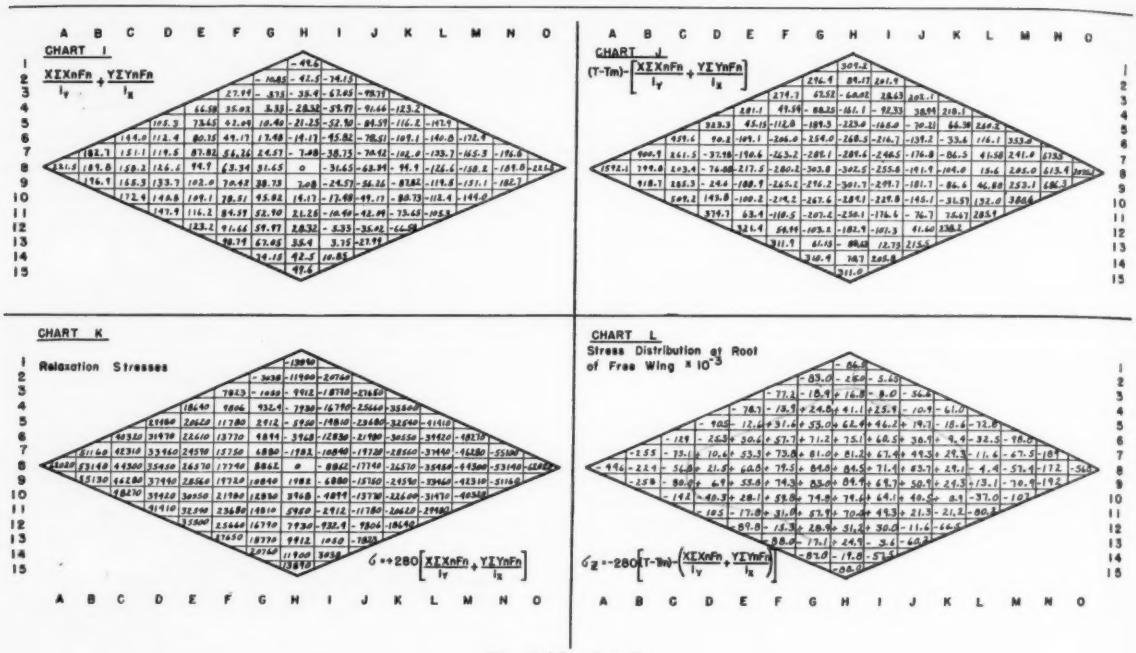

FIG. 5 (*Concluded*).

$$\nabla^2 \sigma_z = 0 \tag{5}$$

As a first approximation, the following form was chosen as a solution of Eq. (5):

$$\sigma_z = C_0 + C_1 x + C_2 y \tag{6}$$

Thus we have, as a complete solution to the stress equation,

$$\sigma_z = KT + C_0 + C_1 x + C_2 y \tag{7}$$

Before determining the coefficients in the solution, one more step must be taken. We have, up to this point, taken the wing to be infinite. This includes the assumption that the wing sections remain plane and parallel. An examination of the curves of temperature distribution shows that there exists a certain amount of antisymmetry about both x and y axes. Under actual conditions similar to a semi-infinite wing, this will result in a curvature of the wing, thus reducing a certain amount of the spanwise stress. If the infinite wing of the original assumption were to be cut, this curvature would result. In this case the change in the stress distribution would be numerically equal to the stress created by the application to the wing of a bending moment great enough to produce the same curvature. When the infinite beam is cut, there is an accompanying phenomenon that must be taken into consideration. Since there no longer exists a spanwise restraint on the now free end of the wing, the section will no longer be plane. However, as previously mentioned, the conditions at the end of the wing are of minor importance; therefore, we are interested only in the effect of the free end on the root of the wing. If the assumptions previously stated are valid, the effect on the stresses at the root of the nonplane end will be negligible.

Returning to the solution of the stress equation, the undetermined coefficients may now be evaluated by applying the necessary conditions of equilibrium for the free wing. These are:

(1) The resultant spanwise force on any section must be zero.

$$\int_A \sigma_z \, dA = 0 \tag{8}$$

(2) The resultant moment about the x axis must be zero.

$$\int_A y\sigma_z \, dA = 0 \tag{9}$$

(3) The resultant moment about the y axis must be zero.

$$\int_A x\sigma_z \, dA = 0 \tag{10}$$

Applying condition No. (1)

$$\int_A \sigma_z \, dA = 0 = K \int_A T \, dA + C_0 \int_A dA + C_1 \int_A x \, dA + C_2 \int_A y \, dA$$

Since the area is symmetric with respect to the x and the y axes, we have

$$\int_A x \, dA = \int_A y \, dA = 0$$

Hence,

$$C_0 = -K\left[(1/A)\int_A T\,dA\right]$$

It is seen that the expression $(1/A)\int_A T\,dA$ is simply the area mean temperature, which we shall define as T_m; hence,

$$\sigma_z = K(T - T_m) + C_1 x + C_2 y$$

Applying condition No. (2),

$$\int_A y\sigma_z\,dA = 0 = K\int_A y(T - T_m)\,dA + C_1\int_A xy\,dA + C_2\int_A y^2\,dA$$

Since the x and y axes are also the principle axes of inertia, the expression $\int_A xy\,dA$, being the product of inertia, is zero. Defining $\int_A y^2\,dA$, the moment of inertia of the area about the x axis, as I_x, we have

$$C_2 = -K\frac{1}{I_x}\int_A y(T - T_m)\,dA$$

In a similar manner condition No. (3) yields, for C_1,

$$C_1 = -K\frac{1}{I_y}\int_A x(T - T_m)\,dA$$

and the final expression for the spanwise stress is

$$\sigma_z = K\left[(T - T_m) - \frac{1}{I_x}\int_A y(T - T_m)\,dA - \frac{1}{I_y}\int_A x(T - T_m)\,dA\right] \quad (11)$$

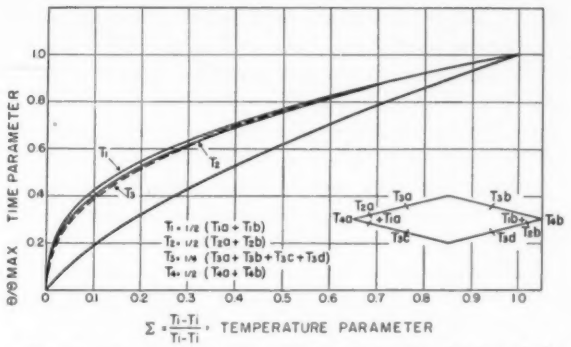

FIG. 6. Temperature-time relationship in the vicinity of the leading and trailing edges during acceleration from $M = 1.4$ to 6.0.

There now remains the numerical evaluation of the above equation.

METHOD OF SOLUTION

In computing the temperature distribution, the cross-sectional area of the wing was subdivided into small areas, and the temperature of each of these subdivisions was assumed constant over the area. If this assumption is continued, the computation of stress is made relatively simple. Defining T_n as the temperature at any particular point and A_n as the area corresponding to that point, Fig. 3, then the expression for the mean temperature becomes

$$T_m = (1/A)\sum_0^n T_n A_n \quad (12)$$

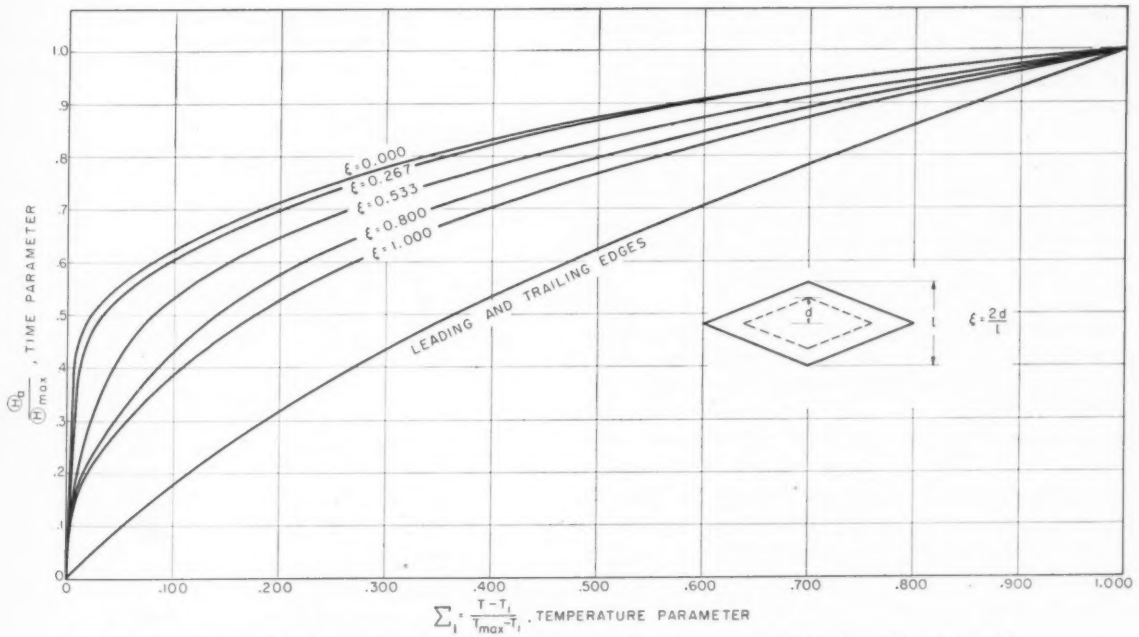

FIG. 7. Temperature-time relationship at any point in the wing during acceleration from $M = 1.4$ to 6.0.

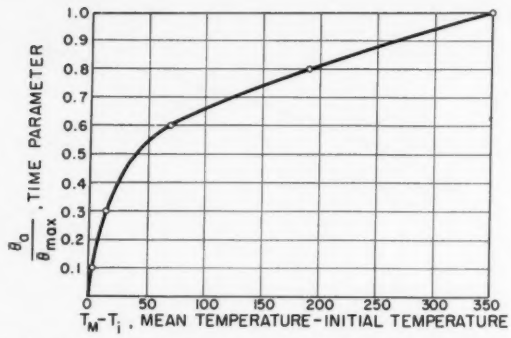

FIG. 8. Mean temperature of wing during acceleration from $M = 1.4$ to 6.0 at the rate of 1g.

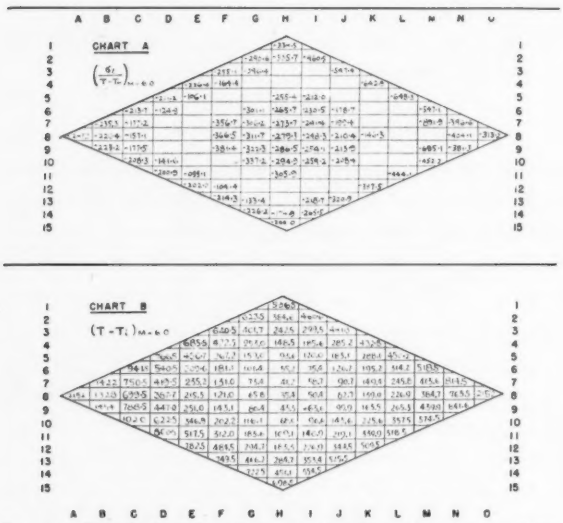

FIG 9. Calculations for thermal stress in wedge-shaped wing during acceleration from $M = 1.4$ to 6.0 at the rate of 1g.

Now defining $F_n = [(T - T_m)_n A_n]$, the final result is an expression for σ_z in the form

$$\sigma_z = K\left[(T - T_m) - \frac{1}{I_y}\sum_0^n x_n F_n - \frac{1}{I_z}\sum_0^n y_n F_n\right] \tag{13}$$

NUMERICAL SOLUTION

In order to obtain numerical results for the existing stresses, values for E, ν, and α must be chosen. Since data were not available for a material that would serve satisfactorily at the elevated temperatures computed, the constants for steel at room temperature were chosen. The resulting stress values are therefore rather meaningless on an absolute basis, but they do serve as a means of studying the relative distribution of the existing stresses. Using the values $E = 30 \times 10^6$ lbs. per sq.in., $\nu = 0.30$, and $\alpha = 6.5 \times 10^{-6}$ in. per in. °F., we get

$$E' = 33 \times 10^6; \quad \nu' = 0.428; \quad \alpha' = 8.45 \times 10^{-6}$$

Hence,

$$K = -(\alpha E + \nu'\alpha' E') = -280 \text{ lbs. per in. per in. °F.}$$

The actual numerical calculations have been carried out on Fig. 5. Chart K shows the evaluation of the stresses introduced by cutting the infinite wing. As determined by the form of the homogeneous solution, Eq. (6), to the stress equation, these stresses vary linearly across the wing. It will also be noted that their magnitude is about 12 per cent of the stresses given by the particular solution. In view of the small influence of the homogeneous solution on the final stress distribution, it is logical to assume that the solution chosen, although simple, provides adequate accuracy. Hence, Chart L, Fig. 5, represents the distribution of thermal stresses in the wing at the instant it has reached a Mach Number of 6.0. Values from this chart are shown graphically in Figs. 10 through 16 for various concentric diamonds in the interior of the wing.

Only σ_z stresses are shown, because in preliminary calculations it was found that the σ_x and σ_y are much smaller than these. Fig. 16 is a schematic diagram showing the stresses at Mach Number 6.0. The dotted line represents the *region* of zero stress. The stresses inside the dotted line are tension stresses, and the stresses outside the dotted line are compressive stresses.

STRESSES DURING ACCELERATION

Inspection of Eq. (13) shows σ_z to vary nearly proportionally to $(T - T_m)$ at any point, since the last two terms decrease in magnitude when the first term does. Although the actual variation may not be linear, the assumption is fairly good, since the last two

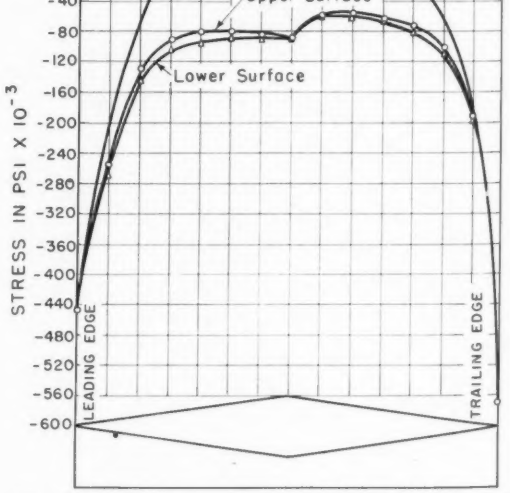

FIG. 10. Stress distribution along upper and lower surfaces of wing.

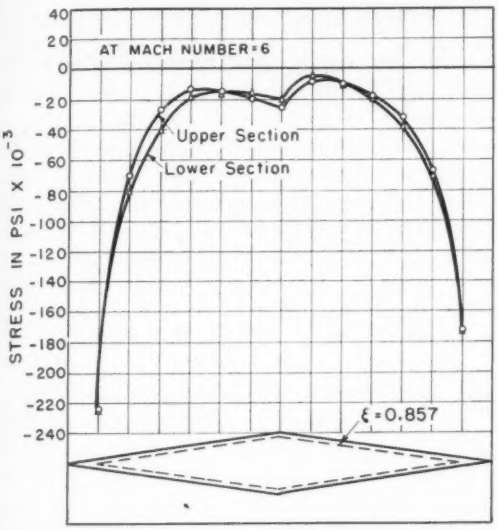

Fig. 11. Stress distribution on diamond with parameter $\xi = 0.857$.

terms account for only about 10 per cent of the stress. As a good approximation, the stress during acceleration may then be calculated by the following equation:

$$\sigma_z = (T - T_m)\,[(\sigma_z)_{M=6.0}/(T - T_m)_{M=6.0}] \quad (14)$$

Plots of temperature as a function of time were made for a series of points on the surface of the wing. It was found that the dispersion of all the points with exception of the leading and trailing edges was less than 5 per cent. Fig. 6 shows the distribution in the immediate vicinity of the leading edge. It is seen that the final chart is applicable at all points except the leading edge and trailing edge. Therefore, one curve would be sufficient for the temperature-time function on the surface of the wing. To make the curve useful, it was reduced to dimensionless parameters, which are

$$\theta = \frac{\theta_a}{\theta_{max.}} = \frac{\text{actual time}}{\text{time from } M = 1.4 \text{ to } 6.0}$$

$$\sum = (T - T_i)/(T_{max.} - T_i)$$

where

T = actual temperature at a point
T_i = initial temperature, 531.6°F. abs.
$T_{max.}$ = temperature at a point at $M = 6.0$

Further investigation of the temperature distributions showed that, for any diamond concentric with the surface, the time-temperature function was the same. The parameter ξ was used to define a particular diamond as follows (Fig. 4):

$$\xi = \frac{2d}{l} = \frac{2(|y| + |x| \tan \beta)}{l}$$

The resulting family of curves, showing the variation of the parameter $\sum$ as a function of θ for various values of ξ, is shown on Fig. 7.

Fig. 8 is a plot showing the mean temperature of the wing cross section as a function of the time parameter. Chart A of Fig. 9 presents values of $[\sigma_z/(T - T_m)]$ at a Mach Number of 6 immediately after the constant acceleration. This function becomes infinite when $(T - T_m)$ is zero. The omitted values on Chart A, Fig. 12, are in this region. This region is of little interest, since the extremes of thermal stress occur near the center and at the outer edges.

To obtain the thermal stress at some point in the wing at some time during the acceleration, determine $\sum$ from Fig. 7; $T_m - T_i$ from Fig. 8; $[\sigma_z/(T_{max.} - T_m)]$ at $M = 6$ from Fig. 9, Chart A; and $(T_{max.} - T_i)$ from Fig. 9, Chart B.

Then get $T - T_m$ from

$$T - T_m = (T_{max.} - T_i)\sum - (T_m - T_i) \quad (15)$$

and σ_z from Eq. (14).

Sample Calculation

Suppose the stress at the point $x = -14.143$ in., $y = 1.1314$ in., and $\theta_a = 103$ sec. were desired. For this point the time parameter would be

$$\theta = \theta_a/\theta_{max.} = 103/138 = 0.75$$

and the diamond parameter would be

$$\xi = \frac{2(|y| + |x| \tan \beta)}{l} = \frac{2[1.1314 + 14.134(0.08)]}{5.380} = \frac{4.524}{5.380} = 0.840$$

To find the stress, the following procedure is used: The parameters θ and ξ are taken to the Fig. 7, and the constant $\sum = 0.45$ is found. From Fig. 8, $(T_m - T_i) = 152$°F.; from Chart B, Fig. 9, $(T_{max.} - T_i) = 456.7$°F. From Eq. (15),

$$T - T_m = (456.7)\,(0.45) - 152 = 54$$

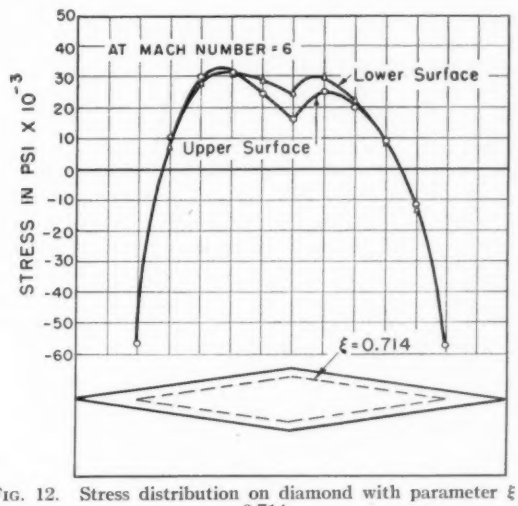

Fig. 12. Stress distribution on diamond with parameter $\xi = 0.714$.

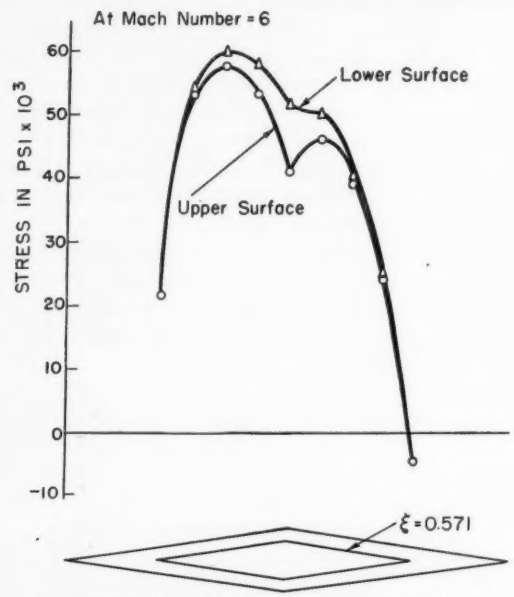

FIG. 13. Stress distribution on diamond with parameter $\xi = 0.571$.

From Chart A, Fig. 9,

$$[\sigma_z/(T_{max.} - T_m)]_{M=6} = -106.1$$

therefore, from Eq. (14),

$$\sigma_z = (-106.1)\ (54) = 5{,}730 \text{ lbs. per sq.in.}$$

At $M = 6$ the stress at this point is 12,600 lbs. per sq.in. as read from Chart L of Fig. 5.

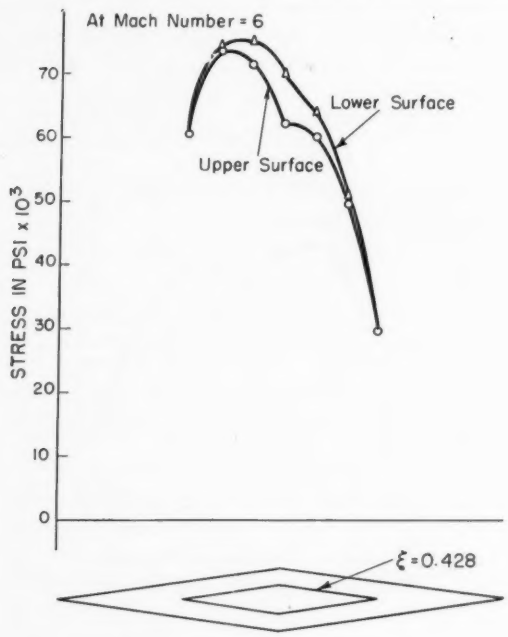

FIG. 14. Stress distribution on diamond with parameter $\xi = 0.428$.

DISCUSSION OF ASSUMPTIONS AND METHOD

Under actual conditions the wing might be tapered from the fuselage to the tip, both in thickness and chord. It will be recalled that the temperature distribution was computed on the basis of an infinite wing having the section of the root of the actual wing; therefore, the temperatures as computed are probably valid only in the immediate vicinity of the root. Because of the continual decrease in cross-sectional area as the tapered wing tip is approached, it is a logical assumption that the heating of the wing will occur more and more uniformly, thus reducing the gradients. Since the stresses and temperature gradients are closely related, it is seen that the maximum stresses will occur at the root of the wing. It was thus decided that a method of computation that would give the root stresses would be sufficient. These assumptions permitted the computations to be made for a semi-infinite wing with a section identical to that at the root of the wing. This assumption also serves to reduce the stress problem from a three-dimensional problem to one of plane strain.

The problem of determining the stress distribution throughout the wing as a function of time was resolved into two sections for simplicity. First, the stresses corresponding to the temperature distribution at the completion of acceleration were computed. Then, rather than repeat the necessary computations for all time intervals from $M = 1.4$ to 6.0, a parametric method, based on the temperature distribution, was evolved. From Eq. (13) it is seen that the stresses are nearly proportional to the difference between the actual temperature and the mean temperature at any given time, the digression from proportionality being caused by the nonlinear nature of the antisymmetry of the temperature distribution. However, since the relaxation stresses are, in themselves, of small magnitude, the variations in these stresses will be negligible, and the assumption of a proportional relation between the stresses and the temperature difference is a valid one. Unfortunately, the use of the parametric method described involves the distribution of four variables—the two-dimensional location of a point in the wing, the value of the temperature difference at that point, and the time from $M = 1.4$. In order to reduce the computation of stresses to its simplest possible terms, the construction of a family of curves was necessary; however, since four variables existed, it was necessary to determine a constant relationship between two of them. It was for these reasons that the seemingly complex procedure set forth was derived.

At the present time there exists no information on the possible materials for the construction of a wing such as has been analyzed. Therefore, the computation of actual stresses is out of the question. In order to obtain a concept of the relative magnitudes of the stresses involved, sample calculations were made using

the properties of steel at room temperatures. An entire calculation was carried out on this basis as a demonstration of the method of application of the computation procedure. The numerical values presented are meaningless and should be considered only as representing the range and distribution of stress in the wing. The calculation procedure as described is applicable to any material and temperature distribution, provided the stated assumptions may be made.

Discussion of Results

Assuming that the stresses as found are valid for the conditions, an analysis of the stress results is in order. Of primary importance are the leading and trailing edges. It will be noticed that the values of stresses presented for these locations are beyond the range of credibility. This is a direct result of the assumptions of elasticity. Obviously, plastic flow would have taken place long before the stresses computed were reached. The existence of this flow is, in effect, a stress relief. When the condition of high temperature gradient has been removed, either by stabilization of speed at $M = 6.0$ or by return to a lower speed, the compressive flow that took place will reverse sign and become a residual tensile stress. The following cycles of stress will then be forced to overcome this tension before the compressive stresses can be produced. The combination of the high stress gradient and the thinness of the section at the leading and trailing edges would result in a buckling of the edges, since the ability of a thin section of that nature to sustain a high compressive load is limited.

To validate the buckling of the edges, a prototype of the first 4 in. of the leading edge was made, and a compressive stress was induced by bending. The addition of a heavy base moved the neutral axis of the wedge below the wing section so that the whole section was subject to a linearly increasing compressive stress. It was found that buckling occurred along the edge simultaneously with the commencement of plastic flow. Waves were formed having a length of a little over 1 in., and, as the loading was increased, the buckling waves increased in amplitude and extended further from the edge of the section. Because of the symmetry of the buckling pattern, it was felt that its effect on the aerodynamic conditions would be small.

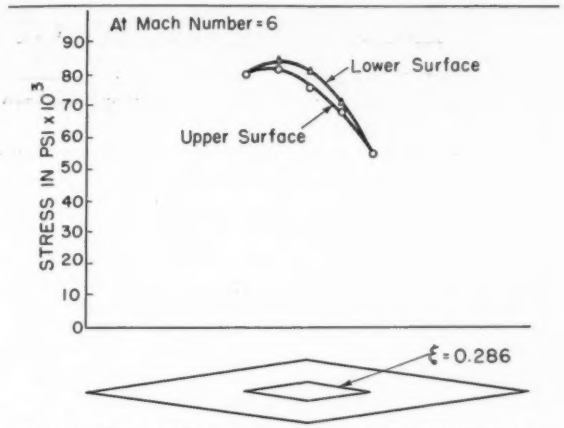

Fig. 15. Stress distribution on diamond with parameter $\xi = 0.286$.

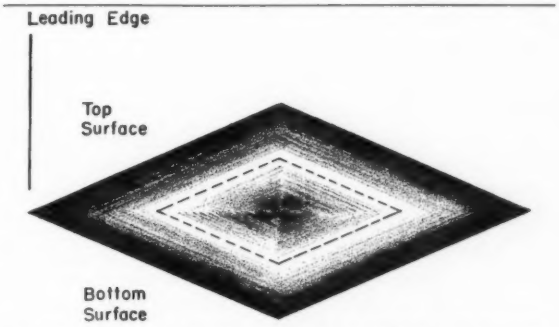

Fig. 16. Schematic diagram showing distribution of intensity of stress in the wing at $M = 6$.

References

[1] Kaye, J., *The Transient Temperature Distribution in a Wing Flying at Supersonic Speeds*, Journal of the Aeronautical Sciences, Vol. 17, No. 12, p. 787, December, 1950.

[2] Timoshenko, S., *Theory of Elasticity*, Chapt. 7; McGraw-Hill Book Company, Inc., New York, 1934.

Buckling Load of a Stepped Column

FREDERIC M. HOBLIT*
Lockheed Aircraft Corporation

Abstract

A procedure is developed for computing the critical buckling load of a column having a finite number of steps with constant EI within each step. The procedure is applicable to columns with any end conditions and with loads applied within the span, as well as at the ends.

Notation

The ith station is at the right-hand, or "far," end of the ith segment.

- L = length of the column
- λ_i = length of the ith segment
- E_i = modulus of elasticity of the ith segment
- I_i = moment of inertia of the ith segment
- P_i = axial compressive load carried within the ith segment (Fig. 2)
- β_i = $\sqrt{P_i/E_iI_i}$
- x, y = coordinates shown in Fig. 2 (x is measured from the beginning of each segment)
- y_i = deflection at the ith station
- y_i' = slope at the ith station
- M_i = bending moment at the ith station
- Q_i = external axial load applied to the column at the ith station. (When load is applied only at the ends, $Q = P = P_i$)
- S = shear force in the column (Fig. 2)
- ω = spring constant, moment per unit angle, for the end restraints or for a rotational spring joint in the column
- 0 = subscript denoting left, or "near," end of the column
- n = number of segments and, hence, as a subscript denotes the right-hand, or "far," end of the column

Introduction

In reference 1, Thomson develops a method for obtaining the critical buckling load of a column having a finite number of steps with different EI in the various steps. Thomson's solution, however, does not include the effect of the shear force that is present in a single-span column whenever the two end moments are unequal and, hence, is applicable only when the conditions of end restraint are such as to make this shear force zero. It is not applicable, for example, to the column fixed at one end and simply supported at the other or to a column fixed at both ends unless the member is symmetrical. It is, of course, applicable to a column simply supported at both ends and to a cantilever column.

In the present paper, the basic equations of reference 1 are rederived to include this shear force, and methods of applying the resulting equations to obtain the critical load are given.

The present method applies not only to columns having any combination of pinned, fixed, and elastically restrained ends but also to columns having axial loads applied within the span, as well as at the ends. The column to be discussed is shown in Fig. 1; the Q_i's may act in either direction.

Derivation of Equations

Considering any point along the segment shown in Fig. 2, isolating the portion to the left of this point, and taking moments about the point, one obtains the following linear differential equation of the deflection curve:

$$E_iI_i\frac{d^2y}{dx^2} = -P_i(y - y_{i-1}) + M_{i-1} + Sx \qquad (1)$$

The solution of this differential equation, with boundary conditions $y = y_{i-1}$ and $y' = y_{i-1}'$ at $x = 0$, is

$$y = y_{i-1} + \frac{M_{i-1}}{P_i} - \frac{M_{i-1}}{P_i}\cos\beta_i x + \frac{y_{i-1}' - (S/P_i)}{\beta_i}\sin\beta_i x + \frac{Sx}{P_i} \qquad (2)$$

where $\beta_i = \sqrt{P_i/E_iI_i}$.

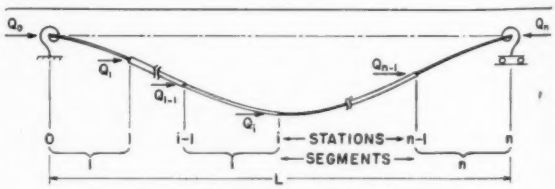

Fig. 1. Single span column of n segments.

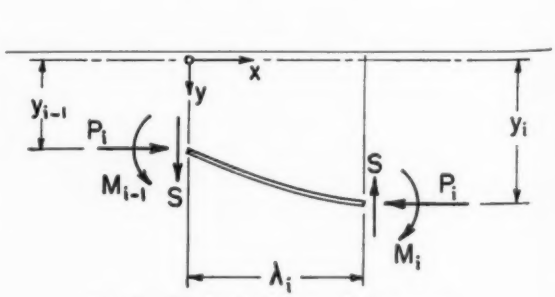

Fig. 2. Free body diagram of ith segment.

Received April 24, 1950.

* Stress Engineer.

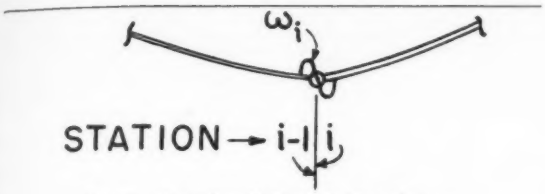

FIG. 3. Rotational hinge joint in column.

Setting $x = \lambda_i$ gives $y = y_i$:

$$y_i = y_{i-1} + \frac{M_{i-1}}{P_i} - \frac{M_{i-1}}{P_i}\cos\beta_i\lambda_i + \frac{y_{i-1}' - (S/P_i)}{\beta_i}\sin\beta_i\lambda_i + \frac{S\lambda_i}{P_i} \quad (3)$$

Differentiating Eq. (2) and again setting $x = \lambda_i$ gives

$$y_i' = \frac{M_{i-1}}{P_i}\beta_i\sin\beta_i\lambda_i + \left(y_{i-1}' - \frac{S}{P_i}\right)\cos\beta_i\lambda_i + \frac{S}{P_i} \quad (4)$$

and

$$M_i = E_iI_i\left(\frac{d^2y}{dx^2}\right)_i = M_{i-1}\cos\beta_i\lambda_i - \left(y_{i-1}' - \frac{S}{P_i}\right)\frac{P_i}{\beta_i}\sin\beta_i\lambda_i \quad (5)$$

If for any segment the axial load is zero, the differential equation becomes

$$E_iI_i(d^2y/dx^2) = M_{i-1} + Sx \quad (6)$$

Proceeding as before, one obtains the following equations, which replace Eqs. (3), (4), and (5) for the segment in question:

$$y_i = y_{i-1} + y_{i-1}'\lambda_i + \frac{M_{i-1}\lambda_i^2}{2E_iI_i} + \frac{S\lambda_i^3}{6E_iI_i} \quad (3a)$$

$$y_i' = y_{i-1}' + \frac{M_{i-1}\lambda_i}{E_iI_i} + \frac{S\lambda_i^2}{2E_iI_i} \quad (4a)$$

$$M_i = M_{i-1} + S\lambda_i \quad (5a)$$

If within any segment the axial load is tension, the equations given do not apply, but equations for this case can be derived similarly to Eqs. (3), (4), and (5). Such equations will be found to contain hyperbolic functions.

If a rotational spring joint is inserted in the column (a condition frequently approached in hydraulic actuators), as shown in Fig. 3, with a spring constant $M/\theta = \omega_i$, the following equations replace Eqs. (3), (4), and (5) for the joint:

$$y_i = y_{i-1} \quad (3b)$$

$$y_i' = y_{i-1}' + (M_{i-1}/\omega_i) \quad (4b)$$

$$M_i = M_{i-1} \quad (5b)$$

General Procedure for Computations

Eqs. (3), (4), and (5) give y, y', and M at the far end of any segment in terms of their values at the near end.

In using these equations to determine the critical load of a column, a trial-and-error procedure is followed. First, a value is chosen for the end load, Q; or if loads are applied within the span, as well as at the ends, a set of values is chosen for all the Q_i's. As successive trials are taken, all the Q_i's should ordinarily be varied in the same ratio. In the following discussion, all references to a value of Q apply equally to a set of values of the Q_i's.

Values are then chosen for y, y', and M at the near end of the column. The chosen values must, of course, be consistent with the end restraints (for a pinned end $y_0 = M_0 = 0$, for a fixed end $y_0 = y_0' = 0$, and for elastic restraint $y_0 = 0$ and $M_0/y_0' = \omega_0$). One of the three quantities y_0, y_0', and M_0 is always arbitrary and may be given any convenient value.

Using Eqs. (3), (4), and (5), one then proceeds segment by segment along the column until y, y', and M are obtained at the far end. Tabular forms can readily be devised to facilitate this numerical work.

If the values obtained for y_n, y_n', and M_n satisfy the end conditions at the far end, the column is in equilibrium in its deflected position under the action of the chosen end load, Q, and, consequently, this value is the critical load.

If the values obtained for y_n, y_n', and M_n do not satisfy the end conditions, then the trial value of Q was not correct and additional trials must be made. However, for any trial, the values of y_n, y_n', and M_n which are obtained may be regarded as defining some new column, with different end conditions, which does have the trial value of Q as its critical load. Usually, as discussed in the section on "Special Cases," it is clear from the values of y_n, y_n', and M_n obtained whether the new column is stiffer or less stiff than the given column and, hence, whether Q has been chosen too high or too low.

Varying the value assigned to whichever of the three starting quantities y_0, y_0', and M_0 is arbitrary will, of course, have no effect upon the value obtained for critical load. If a column is in equilibrium at one small deflection, it will be in equilibrium at any other, and the magnitude of the arbitrary starting quantity simply determines the magnitude of the deflection.

For each trial, all the constants in Eqs. (3), (4), and (5) are known except S, which requires special treatment depending upon the end conditions. Specific procedures for evaluating S and for determining from y_n, y_n', and M_n whether the trial value of Q is less than, equal to, or greater than the critical load are given in the section on "Special Cases."

It is always desirable to sketch the deflection curve for each trial value of end load, both to catch obvious errors and to assure that the critical load obtained is

the smallest one rather than a higher one associated with an unstable, multiple wave buckle form. If y_n, y_n', and M_n have been obtained by proceeding segment by segment along the column as described above (rather than directly in terms of y_0, y_0', and M_0 as by a matrix solution), then all the y_i's, y_i''s, and M_i's are known. The deflection curve can therefore be drawn quickly and with good accuracy simply by spotting in the location of the curve (y_i) at each station, drawing its tangent (slope y_i') at each station, and sketching a smooth curve between.

The method presented herein is applicable in the plastic, as well as the elastic, range if E_i is always taken as the tangent modulus corresponding to the axial load P_i in the segment.[2]

Special Cases

Fig. 4a, Span with Both Ends Pinned, End Loads Only.—$S = 0$. Since for this case $M_{i-1} = -Py_{i-1}$, Eqs. (3) and (4) can be simplified to

$$y_i = y_{i-1} \cos \beta_i\lambda_i + (y_{i-1}'/\beta_i) \sin \beta_i\lambda_i \qquad (3c)$$

$$y_i' = -y_{i-1}\beta_i \sin \beta_i\lambda_i + y_{i-1}' \cos \beta_i\lambda_i \qquad (4c)$$

Eq. (5) is then not needed.

Start with $y_0 = 0$; y_0' = arbitrary. For convenience, take $y_0' = \beta_1$.

The criterion for critical load is $y_n = 0$. If $y_n > 0$, a longer column would be in equilibrium under the same load, so the chosen P is too low. If $y_n < 0$, a shorter column would be in equilibrium, so the chosen P is too high.

Fig. 4b, Span with Left End Fixed or Elastically Restrained, Right End Pinned, End Loads Only.—Start with $y_0 = 0$; M_0 = arbitrary; $y_0' = 0$ if left end is fixed or $y_0' = M_0/\omega_0$ if left end is elastically restrained.

$S = -M_0/L$ in Eqs. (3), (4), and (5).

The criterion for critical load is $y_n = 0$ or $M_n = 0$.

If for convenience the arbitrary value of M_0 is taken as $M_0 = P$, then $S = -P/L$ and Eqs. (3), (4), and (5) become

$$y_i = y_{i-1} + \frac{M_{i-1}}{P} - \frac{M_{i-1}}{P} \cos \beta_i\lambda_i + \frac{y_{i-1}' + (1/L)}{\beta_i} \sin \beta_i\lambda_i - \frac{\lambda_i}{L} \qquad (3d)$$

$$y_i' = \frac{M_{i-1}}{P}\beta_i \sin \beta_i\lambda_i + \left(y_{i-1}' + \frac{1}{L}\right) \cos \beta_i\lambda_i - \frac{1}{L} \qquad (4d)$$

$$M_i = M_{i-1} \cos \beta_i\lambda_i - \left(y_{i-1}' + \frac{1}{L}\right)\frac{P}{\beta_i} \sin \beta_i\lambda_i \qquad (5d)$$

Fig. 4c, Span with Any End Restraints and Several Loads.—Start with $y_0 = 0$. When left end is fixed or has large elastic restraint, M_0 = arbitrary, $y_0' = 0$ if left end is fixed, and $y_0' = M_0/\omega_0$ if left end is elastically restrained. When left end is pinned or has small elastic restraint, y_0' = arbitrary, $M_0 = 0$ if left end is pinned, and $M_0 = y_0'\omega_0$ if left end is elastically restrained. For convenience, take arbitrary M_0 = any Q or P, arbitrary $y_0' = \beta_1$.

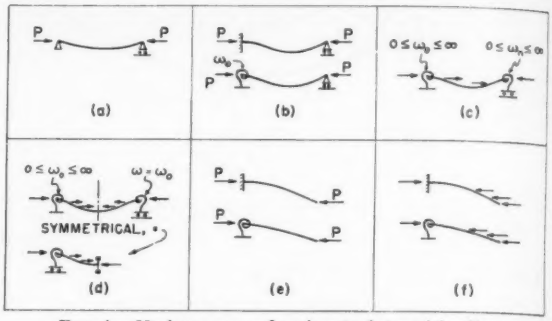

FIG. 4. Various cases of end restraint and loading.

Carry S in literal form through the tabulated calculations. Various quantities in the equations will then appear in the tabulation in the form $(a + bS)$, where a and b are the numbers tabulated.

Use all of Eqs. (3), (4), and (5). Use Eqs. (3a), (4a), and (5a) for any segments having $P_i = 0$.

At the far end of the column, y_n, y_n', and M_n are all functions of S. Obtain S from the condition $y_n = 0$, and obtain y_n' and M_n.

The criterion for critical loading is $-M_n/y_n' = \omega_n$. It should be noted that the value obtained for $(-M_n \div y_n')$ is the restraint that would be required to make the chosen value of Q the actual critical load. In other words, as various values of Q are tried, each trial results in finding some possible physical column for which the chosen value of Q is the critical load. If for any trial the actual end restraint is lower than the required, the column clearly is unstable, and the trial value of Q is too high. Conversely, if the actual end restraint is greater than the required, the column does not buckle, and the trial Q is too low.

Negative values of end restraint mean simply that the end moment M_n applied by the restraint acts to increase rather than decrease the end slope y_n' and could be provided physically by continuity with another column less stable than the one in question.

Fig. 4d, Symmetrical Span.—$S = 0$ in Eqs. (3), (4), and (5). Start with the same values of y_0, y_0', and M_0 as for Fig. 4c. Treat only half the member. The criterion for critical load is, then, $y_n' = 0$.

Fig. 4e, Cantilever, End Loads Only.—$S = 0$. Start with $y_0 = 0$; M_0 = arbitrary; $y_0' = 0$ if left end is fixed or $y_0' = M_0/\omega_0$ if left end is elastically restrained.

Since for this case

$$M_{i-1} = P(y_{max.} - y_{i-1}) = P[(M_0/P) - y_{i-1}]$$

(*Continued on page 138*)

On Some Special Problems in Linearized Axially Symmetric Flow

BERTRAND DES CLERS* AND CHIEH-CHIEN CHANG†

The Johns Hopkins University

SUMMARY

In view of the considerable amount of material published on the linearized treatment of axially symmetric flow, both on the subsonic and the supersonic régime, and because of the complexity of the results, it was thought advisable to work out an example that, by its very simplicity, would give a basic "feeling" for the behavior of bodies in axially symmetric flow.

An infinitely long body with sinusoidal corrugations of the type shown in Fig. 1 was considered, and the first part of this work deals with the study of this body immersed in both purely subsonic and purely supersonic flow, whether in or out of wind tunnels, etc. The second part of the work considers the interaction of concentric annular regions of subsonic and supersonic flow around the same body. The case of a subsonic region is investigated in detail because of its resemblance to the supersonic boundary layer. Whenever deemed necessary, the results were compared or extended to the two-dimensional case by letting the radius of the body become infinite.

Some interesting results are obtained, such as wind-tunnel corrections, deviations from the $1/\sqrt{1 - M^2}$ two-dimensional Prandtl-Glauert compressibility correction, and the fact that the pressure distribution of an axially symmetric body in supersonic flight is no longer proportional to the local slope of the body but lags behind it by an angle that is a function of free-stream Mach Number and body radius. This lag has already been observed in particular problems worked out by the Fourier integral method, such as the minimum drag body problem of thin bodies of revolution. It is also found that the wave drag is finite at a Mach Number of unity, as was deduced by von Kármán in 1935[2] for a similar body. The boundary-layer analogy also shows a few interesting results and, particularly, the effect of the thickness of the subsonic region on the wave drag and pressure distribution of the body.

It is shown briefly in an example how the whole procedure can be extended to a more general axially symmetric body and to any number of concentric annular flows, whether supersonic or subsonic.

LIST OF SYMBOLS

$r_b(x)$	=	equation of the body
$r_i(x)$	=	equation of the gaseous interface
r_0	=	mean radius of the body
i	=	mean radius of the gaseous interface
ϵ	=	amplitude of bumps
L	=	wave length of bumps
α	=	$2\pi/L$
h	=	distance to outer wall (radius of wind tunnel)
M	=	U/a = free-stream Mach Number
β_1	=	$\sqrt{1 - M^2}$
B_2	=	$\sqrt{M^2 - 1}$
r'	=	$r\beta_1$; $r_0' = r_0\beta_1$; $h' = h\beta_1$; $i' = i\beta_1$
r''	=	$r\beta_2$; $r_0'' = r_0\beta_2$; $h'' = h\beta_2$; $i'' = i\beta_2$
T	=	$i - r_0$ = boundary-layer thickness

Received April 28, 1950.

* Graduate Student, Department of Aeronautics.

† Associate Professor of Aeronautics.

$$B = \frac{\rho_1 U_1}{\rho_2 U_2}\left[I_0(\alpha i') + \frac{I_1(\alpha r_0')K_0(\alpha i')}{K_1(\alpha r_0')}\right]$$

$$C = \frac{U_2\beta_1}{U_1\beta_2}\left[I_1(\alpha i') - \frac{I_1(\alpha r_0')K_1(\alpha i')}{K_1(\alpha r_0')}\right]$$

INTRODUCTION

THE EQUATION OF MOTION of an isentropic, inviscid, irrotational fluid can be linearized if we assume that we have a parallel uniform mean flow upon which is superimposed a small disturbance velocity $\vec{q'}$ such that $|q'/U| \ll 1.0$ and $\nabla\varphi = \vec{q'} = u_x'\vec{i_x} + u_r'\vec{i_r}$ where φ is the disturbance potential.

In the case of axial symmetry, the differential equation governing the motion is, in cylindrical coordinates,

$$\frac{\partial^2\varphi}{\partial r^2} + \frac{1}{r}\frac{\partial\varphi}{\partial r} + \frac{\partial^2\varphi}{\partial x^2}(1 - M^2) = 0 \qquad (1)$$

This equation is linear and will allow us to form a general solution, with any particular solutions we can find, by simple superposition. If our boundary condition is bounded and periodic, it can always be expressed as

$$r_b(x) = \sum_{n=0}^{\infty}[a_n \sin(nx) + b_n \cos(nx)] \qquad (2)$$

and it will be sufficient to obtain a solution φ_{sn} or φ_{cn} of Eq. (1) for the simple boundary condition $a_n \sin(nx)$ or $b_n \cos(nx)$, respectively, to build up the solution φ_{r_b} corresponding to the more complicated boundary of Eq. (2):

$$\varphi_{r_b} = \sum_{n=0}^{\infty}[\varphi_{sn} + \varphi_{cn}]$$

Therefore, our problem reduces to the finding of a solution of Eq. (1) for the simple boundary $r_b = r_0 + a \sin(nx)$ or $r_b = r_0 + b \cos(nx)$. This has already been solved in two dimensions (see reference 5), and the results are well known. It is found that, in the case of a sinusoidal wall, say, the pressure distribution is also sinusoidal, being proportional to the slope—that is, 90° out of phase—in the supersonic case and in phase with the wall in the subsonic case. We shall see that this no longer applies in three-dimensional flow.

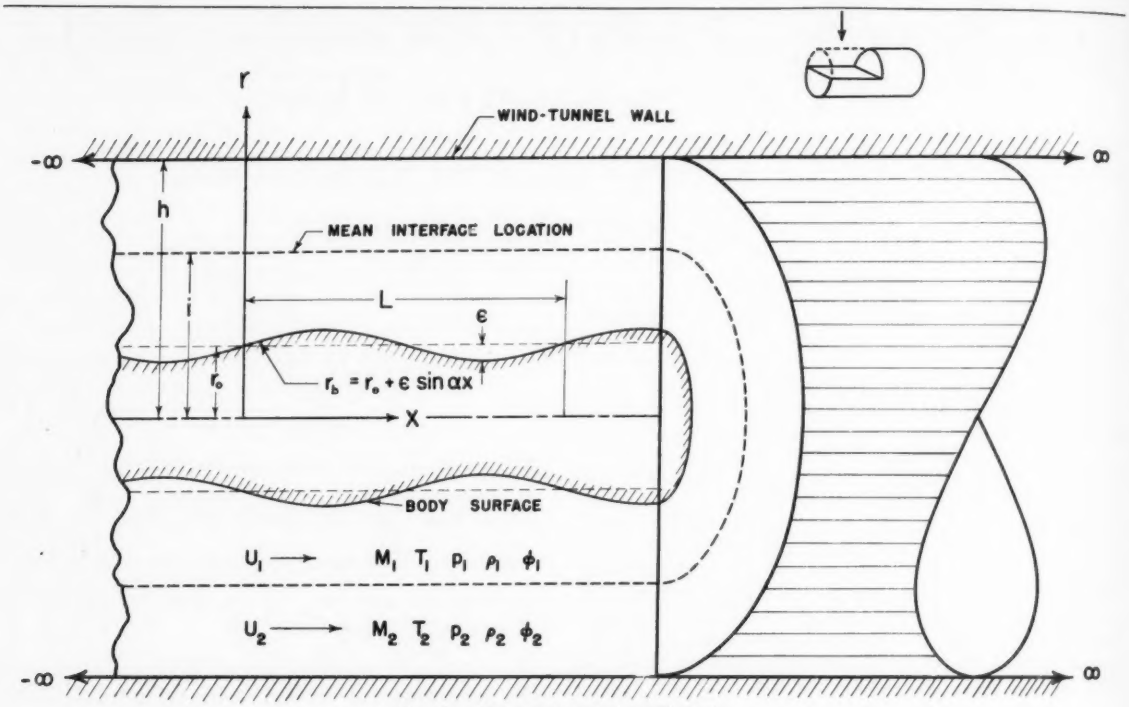

FIG. 1. Picture of body investigated.

LIMITATIONS OF THE THEORY

In order to linearize the equations, we assume small perturbations, u_x'/U, $u_r'/U \ll 1.0$ and irrotationality. Moreover, in the process of solving the equations, we introduce another limitation: Instead of applying the boundary conditions at the exact surface of the body, we apply them at r_0 the mean radius.* We are therefore limited to $\epsilon/r_0 \ll 1.0$.

ANALYSIS

Boundary Conditions

The condition that the flow must follow the surface of the body applies in all cases. This is approximately written

$$(1/U)\,(\partial\varphi/\partial r)_{r_b} = dr_b/dx$$

and if we assume the surface of the body to have the equation

$$r_b = r_0 + \epsilon \sin(\alpha x)$$

the boundary condition reduces to

$$\boxed{(\partial\varphi/\partial r)_{r_b} = U\alpha\epsilon \cos(\alpha x)} \tag{3}$$

The other boundary condition will be furnished by whatever restrictions we impose on the rest of the flow field.

* This is a standard procedure in thin aerofoil theory, where the slope of the surface is given on the chord line.

Subsonic Case: $M < 1.0$

By introducing the new variable $r' = r\beta_1$, we can reduce Eq. (1) to the Laplace equation

$$\boxed{(\partial^2\varphi/\partial r'^2) + (1/r')\,(\partial\varphi/\partial r') + (\partial^2\varphi/\partial x^2) = 0} \tag{4}$$

and if we assume the solution to be of the form $\varphi = R(r')\cdot X(x)$, we obtain the solution

$$\boxed{\varphi = [a \cos(kx) + b \sin(kx)]\,[AI_0(kr') + BK_0(kr')]} \tag{5}$$

where I_0 and K_0 are modified Bessel functions of order zero.

Since we have changed variables, the boundary condition at the wall must be modified accordingly, and Eq. (3) becomes

$$\boxed{\beta_1(\partial\varphi/\partial r')_{r_h} = U\alpha\epsilon\cos(\alpha x)} \tag{6}$$

and if we apply it at r_0, this allows us to evaluate all the constants in Eq. (5) but one, and we get

$$\boxed{\varphi = \frac{U\epsilon}{\beta_1}\cos(\alpha x)\left[\frac{I_0(\alpha r') + DK_0(\alpha r')}{I_1(\alpha r_0') - DK_1(\alpha r_0')}\right]} \tag{7}$$

We now have to introduce another boundary condition to evaluate the constant D. We will consider the three following choices:

Choice A, Solid Wall at $r = h$.—The fact that the flow must be parallel to the wall tells us:

$$(\partial\varphi/\partial r)_h = 0 = (\partial\varphi/\partial r')_h$$

and if we introduce this condition into Eq. (7) for the potential function, we obtain $D = I_1(\alpha h')/K_1(\alpha h')$ and, replacing in Eq. (7),

$$\boxed{\varphi = \frac{U\epsilon}{\beta_1}\cos(\alpha x)\left[\frac{I_0(\alpha r')\,K_1(\alpha h') + K_0(\alpha r')I_1(\alpha h')}{I_1(\alpha r_0')K_1(\alpha h') - K_1(\alpha r_0')I_1(\alpha h')}\right]} \tag{8}$$

Choice B, Free Jet Boundary at $r = h$.—In this case, we must have ambient static pressure at the boundary, since it cannot support any force; therefore, $(\partial\varphi/\partial x)_h = 0$, which allows us to obtain $D = -I_0(\alpha h')/K_0(\alpha h')$ so that the potential function is

$$\boxed{\varphi = \frac{U\epsilon}{\beta_1}\cos(\alpha x)\left[\frac{I_0(\alpha r')K_0(\alpha h') - K_0(\alpha r')I_0(\alpha h')}{I_1(\alpha r_0')K_0(\alpha h') + K_1(\alpha r_0')I_0(\alpha h')}\right]} \tag{9}$$

Choice C, Free Flight.—The only condition that we can impose here is that our solution remain finite at infinity. We can therefore obtain it by letting $h \to \infty$ in Eq. (8), say, and we get

$$\boxed{\varphi = (-U\epsilon/\beta_1)\cos(\alpha x)\left[\frac{K_0(\alpha r')}{K_1(\alpha r_0')}\right]} \tag{10}$$

which vanishes when we let $r \to \infty$, and this satisfies our boundary condition.

Pressure Correction Due to Wind-Tunnel Wall Interference

We now have obtained the velocity potentials, and, since the pressure coefficient is defined as

$$C_P = (-2/U)(\partial\varphi/\partial x)$$

it becomes a simple matter to determine the pressure distribution at the surface of the body, in which we are most interested.

For free flight, we get, from Eq. (10),

$$\boxed{C_{P_{\text{F.F.}}} = (-2\alpha\epsilon/\beta_1)\sin(\alpha x)\left[\frac{K_0(\alpha r_0')}{K_1(\alpha r_0')}\right]} \tag{11}$$

which we can compare with the wind-tunnel pressure distributions.

Case A (Closed-Throat Wind Tunnel).—We obtain, from Eq. (8),

$$\boxed{C_{P_{\text{W.T.}}} = \frac{2\alpha\epsilon}{\beta_1}\sin(\alpha x)\left[\frac{I_0(\alpha r_0')K_1(\alpha h') + K_0(\alpha r_0')I_1(\alpha h')}{I_1(\alpha r_0')K_1(\alpha h') - K_1(\alpha r_0')I_1(\alpha h')}\right]} \tag{12}$$

The ratio of Eqs. (11) and (12) has been plotted in Fig. 2, for various values of $\alpha r_0'$ and compared with the two-dimensional correction corresponding to $\alpha r_0' = \infty$, which is given by

$$(C_{P_{\text{W.T.}}}/C_{P_{\text{F.F.}}})_{\text{2-dim.}} = \coth(\alpha h')$$

It can be seen that this ratio is always greater than unity; the reason the two-dimensional effect is greater than the three-dimensional one for large values of $\alpha h'$ is because of an area effect.

Case B (*Open-Throat Wind Tunnel*).—From Eq. (9),

$$C_{P_{\text{W.T.}}} = \frac{2\alpha\epsilon}{\beta_1} \sin(\alpha x) \left[\frac{I_0(\alpha r_0')K_0(\alpha h') - K_0(\alpha r_0')I_0(\alpha h')}{I_1(\alpha r_0')K_0(\alpha h') + K_1(\alpha r_0')I_0(\alpha h')}\right] \tag{13}$$

and the ratio of Eqs. (11) and (13) has also been plotted on Fig. 2, showing that the measured pressures will be lower than free flight. The corresponding two-dimensional expression ($\alpha r_0' = \infty$) is

$$(C_{P_{\text{W.T.}}}/C_{P_{\text{F.F.}}})_{\text{2-dim.}} = \tanh(\alpha h')$$

It is seen, from the overall nature of Fig. 2, that the wind-tunnel interference becomes negligible for values of ($\alpha h' - \alpha r_0'$) exceeding 2. This shows what size the wind tunnel should be in order to approximate free-flight conditions; this size is seen to increase for any particular model as the Mach Number approaches unity.

***Compressibility Effects* (*Free Flight*)**

Considering the wealth of information available on the results of potential theory and the relative ease with which we can compute the flow of an incompressible, inviscid fluid about any particular body, we would like to know what happens to our calculated pressure distribution when we put the same body in a compressible fluid. The pressure correction has been worked out for two-dimensional flow, known as the Prandtl-Glauert correction,

$$(C_P/C_{P_i})_{\text{2-dim.}} = 1/\beta_1 \tag{14}$$

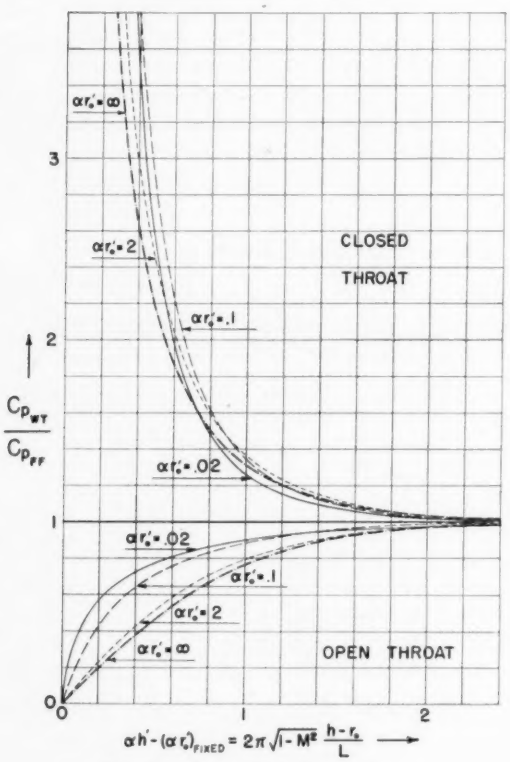

FIG. 2. Wind-tunnel corrections.

where C_{P_i} is the pressure coefficient in the incompressible case. In order to obtain C_{P_i} for our axially symmetric body, we merely set the Mach Number $M = 0$ in Eq. (11), and we obtain

$$\frac{C_P}{C_{P_i}} = \frac{1}{\beta_1}\left[\frac{K_0(\alpha r_0')K_1(\alpha r_0)}{K_1(\alpha r_0')K_0(\alpha r_0)}\right] \tag{15}$$

This equation has been plotted in Fig. 3 for different values of r_0/L and is compared with the two-dimensional expression of Eq. (14) and with the Göthert correction

$$\left(\frac{C_P}{C_{P_i}}\right)_{\text{G.C.}} = 1 + \frac{\log_e \beta_1}{1.7212 + \log_e (r_0/L)} \tag{16}$$

originally obtained by considering the flow about thin ellipsoids of revolution.

It can be shown that Eq. (14) is merely a limiting case of Eq. (15) for $\alpha r_0' \to \infty$ and that Eq. (16) corresponds to taking only the linear terms in the series expansions for the Bessel functions; this last expression is shown not to agree too well, however, even when r_0/L is as

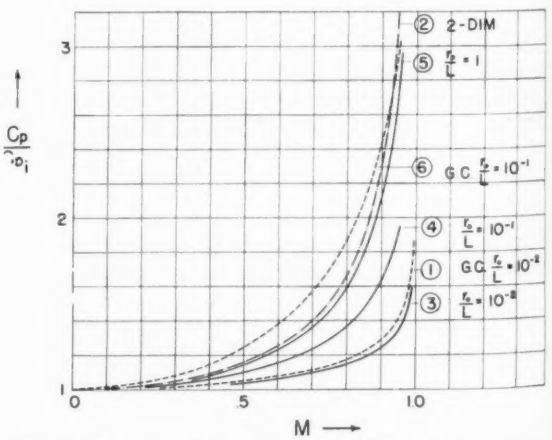

FIG. 3. Compressibility corrections—curve (2), two-dimensional—curves (1) and (6), Göthert correction—curves (3), (4), (5), exact three-dimensional expressions.

small as 10^{-2}, and to be very far off for a value of $r_0/L = 10^{-1}$ over all the practical range of Mach Numbers.

Supersonic Case: *$M > 1.0$*

By introducing a new variable, $r'' = r\beta_2$, we can transform Eq. (1) into the wave equation

$$\boxed{(\partial^2\varphi/\partial r''^2) + (1/r'')(\partial\varphi/\partial r'') = \partial^2\varphi/\partial x^2} \tag{17}$$

and, again assuming the variables to be separable, we obtain a solution of the form

$$\boxed{\varphi = [a\cos(kx) + b\sin(kx)][AJ_0(kr'') + BY_0(kr'')]} \tag{18}$$

and we must again modify our boundary condition at the body in terms of the new coordinate system, so Eq. (3) becomes

$$\boxed{\beta_2(\partial\varphi/\partial r'')_{r_0} = U\alpha\epsilon\cos(\alpha x)} \tag{19}$$

which can be applied immediately to Eq. (18) in order to evaluate some of the constants; we get

$$\boxed{\varphi = -\frac{U\epsilon}{\beta_2}\cos(\alpha x)\left[\frac{J_0(\alpha r'') + DY_0(\alpha r'')}{J_1(\alpha r_0'') + DY_1(\alpha r_0'')}\right]} \tag{20}$$

which contains only one arbitrary constant to be evaluated by introducing one more boundary condition. We will again consider three choices for that extra boundary condition.

Choice A, Solid Wall at $r = h$.—We must have the flow parallel to the wall or

$$(\partial\varphi/\partial r)_h = 0 = (\partial\varphi/\partial r'')_h$$

which gives us $D = -J_1(\alpha h'')/Y_1(\alpha h'')$, where $h'' = h\beta_2$; if we replace into the potential function, we get

$$\boxed{\varphi = -\frac{U\epsilon}{\beta_2}\cos(\alpha x)\left[\frac{J_0(\alpha r'')Y_1(\alpha h'') - Y_0(\alpha r'')J_1(\alpha h'')}{J_1(\alpha r_0'')Y_1(\alpha h'') - Y_1(\alpha r_0'')J_1(\alpha h'')}\right]} \tag{21}$$

Choice B, Free-Jet Boundary at $r = h$.—In this case, we must specify the pressure at the boundary to be ambient static pressure or

$$(\partial\varphi/\partial x)_h = 0$$

which gives us $D = -J_0(\alpha h'')/Y_0(\alpha h'')$ and the potential function becomes

$$\boxed{\varphi = -\frac{U\epsilon}{\beta_2}\cos(\alpha x)\left[\frac{J_0(\alpha r'')Y_0(\alpha h'') - Y_0(\alpha r'')J_0(\alpha h'')}{J_1(\alpha r_0'')Y_0(\alpha h'') - Y_1(\alpha r_0'')J_0(\alpha h'')}\right]} \tag{22}$$

Choice C, Free Flight.—The only further restriction that we can impose on the flow is to eliminate the disturbances from infinity—i.e., the incoming set of Mach waves. This is done by considering the Mach waves to become very nearly plane waves at a large distance from the body where the potential function will therefore be of the form

$$\varphi = F(x - r'') + G(x + r'')$$

and making $G \equiv 0$. Using the asymptotic expansions of J_n and Y_n, we can evaluate the constant.* We get, after also applying the boundary condition at the body,

$$\boxed{\varphi = \frac{-U\epsilon}{\beta_2[J_1^2(\alpha r_0'') + Y_1^2(\alpha r_0'')]}\{[J_1(\alpha r_0'')J_0(\alpha r'') + Y_1(\alpha r_0'')Y_0(\alpha r'')]\cos(\alpha x) + [J_1(\alpha r_0'')Y_0(\alpha r'') - Y_1(\alpha r_0'')J_0(\alpha r'')]\sin(\alpha x)\}} \tag{23}$$

* The same result can be obtained by taking $\varphi = Re[Ae^{i\alpha z}H_0^{(2)}(\alpha r'')]$, which represents the outgoing family of waves,[2] while . . . $H_0^{(1)}(\alpha r'')$ represents the incoming family.

Free-Flight Pressure Distribution

Differentiating Eq. (23) with respect to x and multiplying it by $-2/U$, we obtain

$$C_P = \frac{-2\alpha\epsilon}{\beta_2[J_1^2(\alpha r_0'') + Y_1^2(\alpha r_0'')]}\left\{[J_0(\alpha r_0'')J_1(\alpha r_0'') + Y_0(\alpha r_0'')Y_1(\alpha r_0'')]^2 + \frac{4}{\pi^2(\alpha r_0'')^2}\right\}^{1/2} \sin(\alpha x - \psi) \tag{24}$$

where

$$\psi = \tan^{-1}\left\{\frac{2}{\pi\alpha r_0''[J_0(\alpha r_0'')J_1(\alpha r_0'') + Y_0(\alpha r_0'')Y_1(\alpha r_0'')]}\right\} \tag{25}$$

This shows us that the pressure distribution is again sinusoidal but out of phase by an angle ψ with the body surface. This immediately tells us that we will have drag.

If we compare Eq. (24) with the corresponding two-dimensional expression

$$(C_P)_{2\text{-dim.}} = -(2\alpha\epsilon/\beta_2)\sin[\alpha x - (\pi/2)]$$

we see that their ratio and also the phase angle ψ contain the different parameters r_0, L, and M only in the form of the product

$$\alpha r_0'' = 2\pi(r_0/L)\beta_2$$

Therefore, their value will be the same for equal values of $\alpha r_0''$, irrespective of the contributions of the individual parameters.

In Fig. 4, we have compared the two- and three-dimensional expressions, and it is seen that this ratio is close to unity from a value of $\alpha r_0'' = 4.0$ on. In other words, as far as the amplitude of the pressure coefficient is concerned, a body with $\alpha r_0'' \geqslant 4.0$ is two-dimensional to all practical purposes. However, it can be seen from Fig. 5 that the phase shift does not go to the two-dimensional value of $\pi/2$ quite so fast. (The scale in terms of Mach Number is shown for a body of $r_0/L = 1.0$.)

We can investigate what happens at extremely small values of $\alpha r_0''$ by taking only the linear terms in the series expansions of the Bessel functions. We find that, for $\alpha r_0'' \ll 1.0$,

$$C_P \approx \frac{-4\epsilon}{\pi r_0\beta_2^2}\left\{1 + \frac{4}{\pi^2}[\log_e(\alpha r_0'')]^2\right\}^{1/2} \sin(\alpha x - \psi)$$

where

$$\psi \approx \tan^{-1}[\pi/2 \log_e(\alpha r_0'')]$$

and, similarly, if we investigate the case of $\alpha r_0'' \gg 1.0$, we find the two-dimensional expression for the C_P with $\psi = \pi/2$ given above. The fact that the pressure distribution lagged 90° behind the wall corrugations and had an amplitude proportional to $\alpha\epsilon$ (or the slope) in this case was already known.

Free-Flight Wave Drag

Taking a cylindrical control surface around the body and choosing it of radius r_0 in order to use the expressions already obtained for the derivatives, we have

$$D = -2\pi r_0\rho\int_0^L \left(\frac{\partial\varphi}{\partial x}\right)_{r_0}\left(\frac{\partial\varphi}{\partial r}\right)_{r_0} dx$$

which gives us

$$D = 4\pi\rho U^2\epsilon^2/\beta_2^2[J_1^2(\alpha r_0'') + Y_1^2(\alpha r_0'')]$$

and, if we introduce the drag coefficient, we get

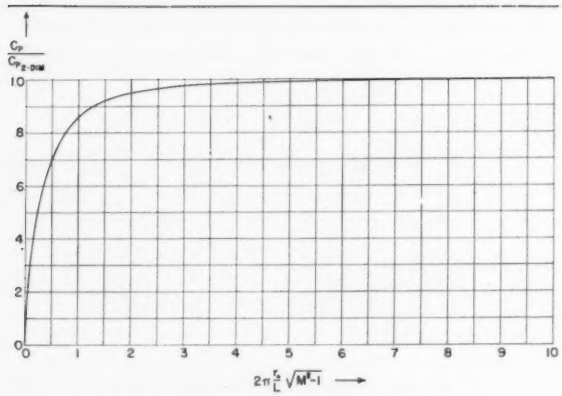

FIG. 4. Supersonic pressure distribution.

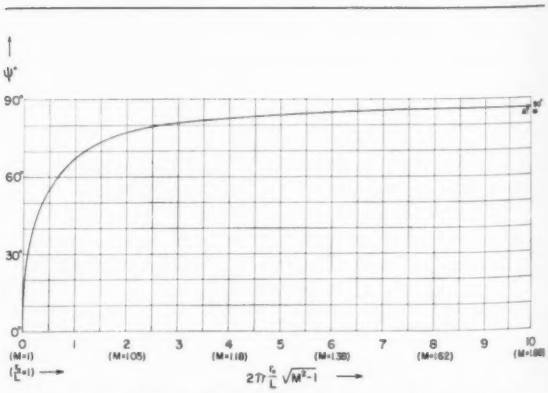

FIG. 5. Phase lag of supersonic pressure distribution

$$C_D = \frac{4}{\beta_2^2} \frac{(\epsilon/L)^2 (L/r_0)}{[J_1^2(\alpha r_0'') + Y_1^2(\alpha r_0'')]} \tag{26}$$

This equation has been plotted in Fig. 6a for a body of $r_0/L = 1.0$, $\epsilon/L = 10^{-2}$, as well as the two-dimensional drag coefficient

$$(C_D)_{2\text{-dim.}} = 4\pi^2(\epsilon/L)^2/\beta_2$$

for the same ϵ/L of 10^{-2}.

One can see clearly that, although the two-dimensional drag coefficient becomes infinite at a Mach Number of unity, the three-dimensional one has a definite value of

$$(C_D)_{M=1.0} = 4\pi^4(\epsilon/L)^2(r_0/L)$$

as had been obtained by von Kármán in his 1935 paper.[2] This finite value is explained by the fact that, although the C_P becomes infinite, the pressure distribution is exactly in phase with the wall as in the subsonic case.

We have also plotted the ratio $C_D/C_{D_{2\text{-dim.}}}$ in Fig. 6b, which is again a function only of $\alpha r_0''$. It can be shown to have a slope of $\pi^2/4$ at the origin.

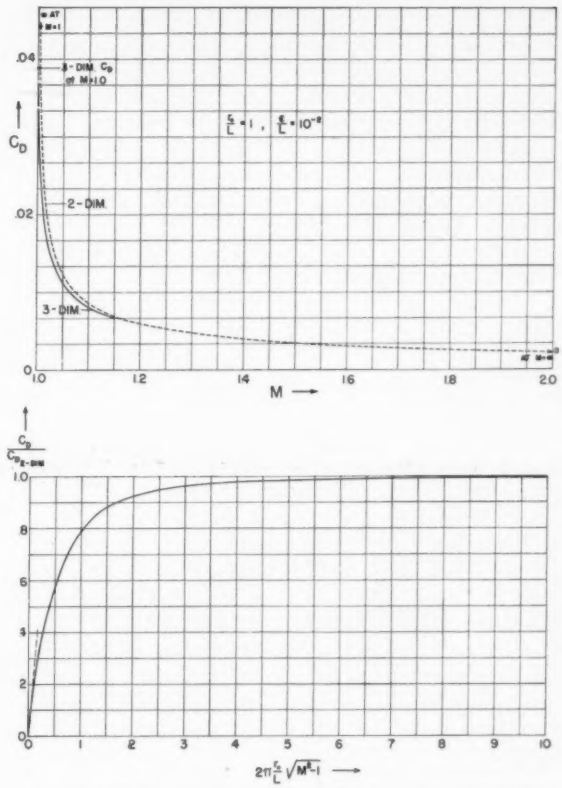

FIGS. 6a (*top*) and 6b (*bottom*). Wave drag: (a) Specific body of $r_0/L = 1$, $\epsilon/L = 10^{-2}$ compared with two-dimensional case, same ϵ/L. (b) Ratio of above 2, valid for any ϵ/L.

Example

Let us consider a boundary

$$r_b(x) = B_0 + \sum_{n=1}^{\infty} B_n \cos(nx)$$

where

$$B_0 = (1/\pi)\,[\sin\theta + (\pi - \theta)\cos\theta]$$

$$B_n = \frac{1}{n\pi}\left[\frac{\sin(n-1)\theta}{n-1} - \frac{\sin(n+1)\theta}{n+1}\right]$$

which is a body of the type of Fig. 7 with parabolic bumps.

(*A*) *Subsonic Case.*—Let us try to find a solution of the Laplace equation in $r' = r\beta_1$ which will satisfy the above boundary conditions. We will take a solution of the form

$$\varphi = \sum_k [a_k \cos(kx) + b_k \sin(kx)] \times [A_k I_0(kr') + B_k K_0(kr')]$$

and the boundary conditions are: (a)

$$(\beta_1/U)\,(\partial\varphi/\partial r')_{r_b} = dr_b/dx$$

flow must follow wall. We assume θ small and evaluate at $r = 1.0$. (b) Solution must remain finite at infinity, from which we find

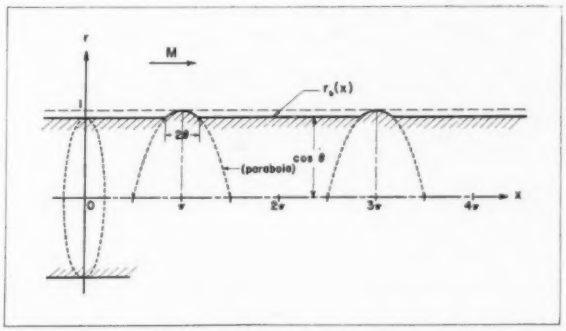

FIG. 7. Shape of more general body investigated.

$$\varphi = \frac{U}{\beta_1} \sum_{n=1}^{\infty} B_n \left[\frac{K_0(nr')}{K_1(n\beta_1)}\right] \sin(nx)$$

from which we can find the pressure coefficient

$$C_P = -\frac{2}{\beta_1} \sum_{n=1}^{\infty} nB_n \left[\frac{K_0(n\beta_1)}{K_1(n\beta_1)}\right] \cos(nx)$$

This shows that we have merely introduced a weighing function $n[K_0(n\beta_1)/K_1(n\beta_1)]$ into the equation of the boundary.

(*B*) *Supersonic Case.*—When $M > 1.0$, we have a solution of the form

$$\varphi = \sum_k [a_k J_0(kr'') + b_k Y_0(kr'')] \cos(kx) + [a_k Y_0(kr'') - b_k J_0(kr'')] \sin(kx)$$

where we have already introduced the fact that we only allow outgoing waves. Our other boundary condition is

$$(\beta_2/U)(\partial\varphi/\partial r'')_{r_b} = dr_b/dx$$

flow must be parallel to the wall, which we evaluate at $r = 1.0$, for small θ. We then get

$$\varphi = \frac{U}{\beta_2} \sum_{n=1}^{\infty} \frac{B_n}{J_1^2(n\beta_2) + Y_1^2(n\beta_2)} \Big\{ [Y_1(n\beta_2) J_0(nr'') - J_1(n\beta_2) Y_0(nr'')] \cos(nx) + [Y_1(n\beta_2) Y_0(nr'') + J_1(n\beta_2) J_0(nr'')] \sin(nx) \Big\}$$

and we can find the pressure distribution at the body

$$C_P = -\frac{2}{\beta_2} \sum_{n=1}^{\infty} \frac{n\beta_n}{J_1^2(n\beta_2) + Y_1^2(n\beta_2)} \Big\{ [Y_1(n\beta_2) Y_0(n\beta_2) + J_1(n\beta_2) J_0(n\beta_2)] \cos(nx) - \frac{2}{\pi n\beta_2} \sin(nx) \Big\}$$

It is therefore a straightforward procedure to calculate the complete flow configuration for any such complicated boundary.

Mixed Flow

Let us consider the problem of having two concentric flows of different Mach Numbers, densities, velocities, etc., separated by a discontinuity surface or gaseous interface $r_i(x)$ and with two arbitrary boundaries $r_h(x)$ and $r_b(x)$. Then, we still will have the differential equation

$$\frac{\partial^2\varphi}{\partial r^2} + \frac{1}{r}\frac{\partial\varphi}{\partial r} + (1 - M^2)\frac{\partial^2\varphi}{\partial x^2} = 0 \qquad (27)$$

which will be satisfied by both φ_1 and φ_2 and for which we have the four following boundary conditions:

$$(1/U_1)(\partial\varphi_1/\partial r)_{r_b} = dr_b(x)/dx$$

flow must be parallel to $r_b(x)$.

$$-\rho_1 U_1(\partial\varphi_1/\partial x)_{r_i} = -\rho_2 U_2(\partial\varphi_2/\partial x)_{r_i}$$

same pressure on both sides of the interface.

$$(1/U_1)(\partial\varphi_1/\partial r)_{r_i} = (1/U_2)(\partial\varphi_2/\partial r)_{r_i}$$

same flow inclination on both sides of the interface.

$$(1/U_2)(\partial\varphi_2/\partial r)_{r_i} = dr_h(x)/dx$$

flow must be parallel to $r_h(x)$; theoretically, this allows us to solve for both φ_1 and φ_2, thus characterizing everything about the flow on both sides of the interface r_i. It is clear that we can also solve this problem for any number of discontinuity surfaces.

We will only solve a particular case here which was thought to be most important because of its interest as a first approximation to the supersonic boundary-layer theory as represented by a step function velocity profile.

Analysis—Free Flight—Mixed Flow

We will limit the present investigation to the particular case where the equation of the body is

$$r_b = r_0 + \epsilon \sin(\alpha x)$$

as in the first section, where the region close to the body and up to r_i is subsonic at a Mach Number $M_1 < 1.0$, pressure P_1, density ρ_1, temperature τ_1, and for which the flow is supersonic and unbounded for $r > r_i$, with flow functions $M_2 > 1.0$, P_2, ρ_2, τ_2.

The boundary conditions for this case are the following:

(1) For φ_1 only,

$$(1/U_1)(\partial\varphi_1/\partial r)_{r_0} = \alpha\epsilon \cos(\alpha x)$$

flow must follow wall.

(2) For φ_1 and φ_2,

$$-\rho_1 U_1(\partial\varphi_1/\partial x)_i = -\rho_2 U_2(\partial\varphi_2/\partial x)_i$$

same pressure on both sides of interface.

(3) For φ_1 and φ_2,

$$(1/U_1)(\partial\varphi_1/\partial r)_i = (1/U_2)(\partial\varphi_2/\partial r)_i$$

same flow inclination on both sides.

(4) For φ_2 only, we must only have the diverging family of waves—i.e., no disturbances coming from infinity.

We know that the potential functions are of the kind

$$\varphi_1 = [a_1 I_0(\alpha r') + a_2 K_0(\alpha r')] \cos(\alpha x) + [a_3 I_0(\alpha r') + a_4 K_0(\alpha r')] \sin(\alpha x) \qquad (28)$$

and

$$\varphi_2 = [b_1 J_0(\alpha r'') + b_2 Y_0(\alpha r'')] \cos(\alpha x) + [b_1 Y_0(\alpha r'') - b_2 J_0(\alpha r'')] \sin(\alpha x) \tag{29}$$

applying condition (4) to φ_2, as we had done in the first part of this work. After some labor, we get

$$a_1 = \frac{-U_1\epsilon}{\beta_1 K_1(\alpha r_0'')} \cdot \frac{1}{(BJ_1 + CJ_0)^2 + (BY_1 + CY_0)^2} \left\{ \frac{U_2\beta_1}{U_1\beta_2} K_1 [C(J_0^2 + Y_0^2) + B(J_0J_1 + Y_0Y_1)] - \frac{\rho_1 U_1}{\rho_2 U_2} K_0 [B(J_1^2 + Y_1^2) + C(J_0J_1 + Y_0Y_1)] \right\}$$

where the J_n and Y_n are evaluated at $\alpha i'' = (2\pi/L) i\beta_2$ and the K_n at $\alpha i' = (2\pi/L) i\beta_1$ and similarly for the following equations.

B and C have the following meaning:

$$B = \frac{\rho_1 U_1}{\rho_2 U_2} \left[I_0(\alpha i') + \frac{I_1(\alpha r_0') K_0(\alpha i')}{K_1(\alpha r_0')} \right] \quad \text{and} \quad C = \frac{U_2\beta_1}{U_1\beta_2} \left[I_1(\alpha i') - \frac{I_1(\alpha r_0') K_1(\alpha i')}{K_1(\alpha r_0')} \right]$$

we also get

$$a_3 = \frac{-U_1\epsilon}{\beta_2 K_1(\alpha r_0')} \cdot \frac{\rho_1 U_1}{\rho_2 U_2} \cdot \frac{U_2\beta_1}{U_1\beta_2} \cdot \frac{2}{\pi(\alpha i')^2} \cdot \frac{1}{(BJ_1 + CJ_0)^2 + (BY_1 + CY_0)^2}$$

$$a_2 = [a_1\beta_1 I_1(\alpha r_0') - U_1\epsilon]/\beta_1 K_1(\alpha r_0')$$

$$a_4 = a_3 [I_1(\alpha r_0')/K_1(\alpha r_0')]$$

which determines φ_1 entirely. We similarly obtain b_1 and b_2.

$$b_1 = \frac{-U_1\epsilon}{\beta_1 K_1(\alpha r_0')} \cdot \frac{\rho_1 U_1}{\rho_2 U_2} \cdot \frac{U_2\beta_1}{U_1\beta_2} \cdot \frac{1}{(\alpha i')} \cdot \frac{BJ_1 + CJ_0}{(BJ_1 + CJ_0)^2 + (BY_1 + CY_0)^2}$$

$$b_2 = \frac{-U_1\epsilon}{\beta_1 K_1(\alpha r_0')} \cdot \frac{\rho_1 U_1}{\rho_2 U_2} \cdot \frac{U_2\beta_1}{U_1\beta_2} \cdot \frac{1}{(\alpha i')} \cdot \frac{BY_1 + CY_0}{(BJ_1 + CJ_0)^2 + (BY_1 + CY_0)^2}$$

Now we can determine everything about both regions of the flow.

Shape of the Gaseous Interface

The local slope of the interface is given by

$$(dr_i/dx) = (1/U_2)(\partial\varphi_2/\partial r)_i$$

and differentiating φ_2, we get

$$\frac{dr_i}{dx} = \frac{\rho_1 U_1}{\rho_2 U_2} \cdot \frac{(\epsilon/i)}{\beta_1 K_1(\alpha r_0')} \left[\frac{J_1^2 + Y_1^2}{(BJ_1 + CJ_0)^2 + (BY_1 + CY_0)^2} \right]^{1/2} \cos(\alpha x - \psi_1)$$

where

$$\psi_1 = \tan^{-1} \left[\frac{-2C}{\pi\alpha i''} \cdot \frac{1}{B(J_1^2 + Y_1^2) + C(J_0J_1 + Y_0Y_1)} \right] \tag{30}$$

and, if we integrate with respect to x above, we get

$$r_i = i + \epsilon_i \sin(\alpha x - \psi_1)$$

where ϵ_i is the amplitude of the wiggles on the interface

$$\frac{\epsilon_i}{\epsilon} = \frac{\rho_1 U_1}{\rho_2 U_2} \cdot \frac{1}{\alpha i' K_1(\alpha r_0')} \cdot \left[\frac{J_1^2 + Y_1^2}{(BJ_1 + CJ_0)^2 + (BY_1 + CY_0)^2} \right]^{1/2} \tag{31}$$

which shows us that the interface is a corrugated pipe of mean radius i, with bumps of an amplitude ϵ_i and out of phase with the wall bumps by the angle ψ_1. ψ_1 turns out to be negative, which means that the interface lies ahead

of the body by that angle. It is seen in Figs. 7 and 8* that, when we shrink the subsonic region to zero, the interface coincides with the body and that the amplitude of the wiggles on the interface decreases sharply as we increase the thickness of the subsonic region. We have also plotted on Figs. 7 and 8 the corresponding limiting case of $r_0/L = \infty$ —e.g., the two dimensional case—for which we find

$$\left(\frac{\epsilon_i}{\epsilon}\right)_{2\text{-dim.}} = \left[\frac{1}{\cosh^2 \alpha\beta_1 T + (\rho_2^2 U_2^2/\rho_1^2 U_1^2)\cdot (U_2^2\beta_1^2/U_1^2\beta_2^2) \sinh^2 \alpha\beta_1 T}\right] \tag{32}$$

$$\text{and} \quad (\psi_i)_{2\text{-dim.}} = \tan^{-1}[-(\rho_2 U_2/\rho_1 U_1)\cdot(U_2\beta_1/U_1\beta_2) \tanh \alpha\beta_1 T] \tag{33}$$

where T is defined as $(i - r_0)$, "the boundary-layer" thickness. The amplitude ϵ_i is seen to decrease much more gradually, starting with zero slope at the origin, while the phase angle rises much more abruptly and later flattens out.

Pressure Distribution at the Body

Let us define the pressure coefficient at the body as

$$C_P = -(2/U_2)\ (\partial\varphi_1/\partial x)_{r_0}$$

using U_2 as our reference velocity. This choice is consistent with our boundary-layer analogy.

We obtain

$$C_P = \frac{-2}{U_2 r_0 \beta_1 K_1(\alpha r_0')} \left\{[a_1 - U_1\alpha\epsilon r_0 K_0(\alpha r_0')]^2 + a_3^2\right\}^{1/2} \sin\ (\alpha x - \psi_2) \tag{34}$$

where

$$\psi_2 = \tan^{-1}\left[\frac{a_3}{a_1 - U_1\alpha\epsilon r_0 K_0(\alpha r_0')}\right] . \tag{35}$$

and a_1, a_3 are the constants evaluated in the potential and have not been written out here in detail in order to save space.

The two expressions above show us that the pressure distribution is not in phase with the body, which would be the case were it in an infinite subsonic flow field, and that we will therefore have drag. This was to be expected, and the drag should be just the one obtainable from Eq. (26) for a body of radius i, bump amplitudes ϵ_i, and in a free-stream Mach Number M_2. Thus, the corrugations of the interface send out waves that will show up as an overall loss in energy or drag. We have plotted the above results in Figs. 9 and 10 for the particular body considered; as it should be, when we remove the interface further and further away from the body, the value of the C_P tends toward that given by Eq. (11) of the body in an infinite subsonic field (that is, $r_0/L = 10^{-1}$, $\epsilon/L = 10^{-2}$, $M = \sqrt{2}/2$) and represented by the dotted line in Fig. 9. Similarly, when we shrink the subsonic region to zero, the C_P tends to the value given by Eq. (24) for that same body in an infinite supersonic field of Mach Number† equals $\sqrt{2}$.

When we examine the behavior of ψ_2, we see that it *tends toward* the value given by Eq. (25) when the interface coincides with the body and *vanishes* when the subsonic field becomes large.

We must remember that the pressure on the body is due (1) to a subsonic pressure, always in phase with the wall, and (2) to an out-of-phase pressure due to the influence of the interface. But the pressure must be the same on both sides of the interface; therefore, we can consider the additional pressure as the one on a body in purely supersonic flow and with corrugations, diameter, and position equivalent to that of the interface. With this picture in mind, we see immediately that $|\psi_1 + \psi_2|$ must behave as our ψ of Eq. (25), since, when the interface moves

* Figs. 7, etc., apply to a specific body of $r_0/L = 10^{-1}$, $\epsilon/L = 10^{-2}$ and to the case where the two flows were chosen with the same stagnation temperature, $M_1 = \sqrt{2}/2$ and $M_2 = \sqrt{2}$. The static pressures on both sides of the interface were taken equal ($P_1 = P_2$), and the ratios of the flow functions were determined by using the relations: $P = \rho R\tau$, $a^2 = \gamma R\tau$, $\tau_0/\tau = \{1 + [(\gamma - 1)/2]M^2\}$, with $\gamma = 1.40$. The same applies to the two-dimensional limiting case of $r_0/L = \infty$. The only case in which ϵ/L occurs is in Fig. 9. All of the others are valid for any ϵ/L.

† Remembering that we must transfer our C_P in terms of φ_2,

$$C_P = -(2/U_2)\ (\partial\varphi_1/\partial x)_{r_0} = (\rho_2 U_2/\rho_1 U_1)\ [-(2/U_2(\partial\varphi_2/\partial x)_{r_0}]$$

with the help of boundary condition (2), since we must take into account the fact that the C_P given by Eq. (24) is $C_P = -(2/U_2)\times (\partial\varphi_2/\partial x)_{r_0}$.

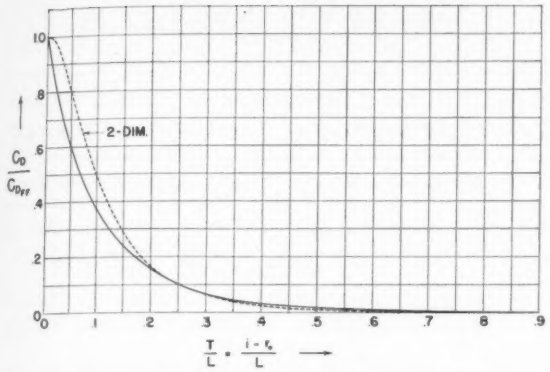

FIG. 8. Amplitude of bumps on interface compared to bumps on the body.

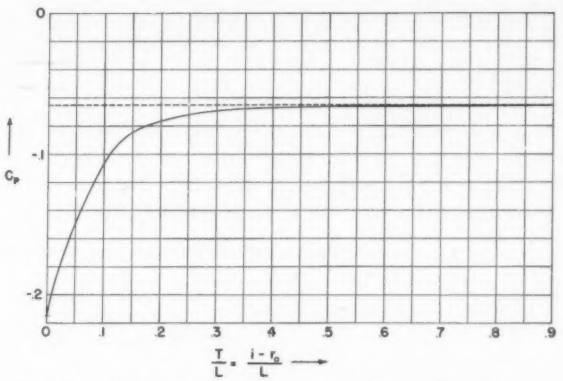

FIG. 10. Amplitude of C_P for numerical example considered: $r_0/L = 10^{-1}$, $\epsilon/L = 10^{-2}$, $M_1 = \sqrt{2}/2$, $M_2 = \sqrt{2}$, $P_1 = P_2$, $r_{0_1} = r_{0_2}$.

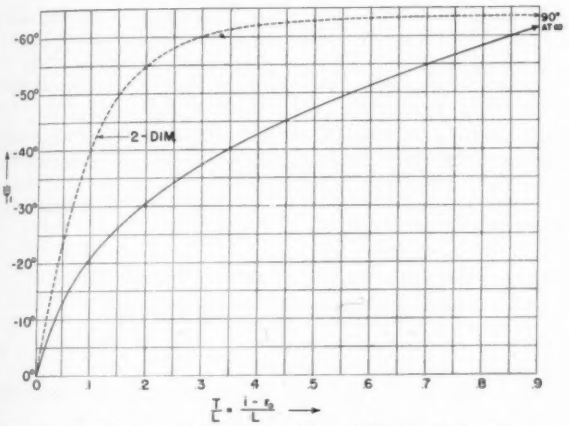

FIG. 9. Angle determining the position of the interface with respect to the body.

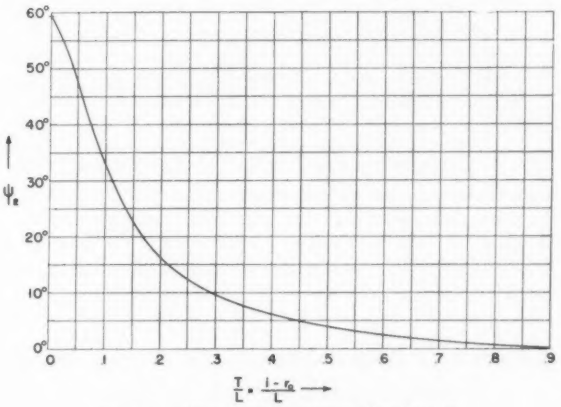

FIG. 11. Phase lag of pressure distribution.

out to infinity, it moves 90° ahead of the body, but the pressure on its outside lags by 90° so that those two effects cancel out, and the additional pressure also gets in phase—i.e., $\psi_2 \to 0$.

Wave Drag

To calculate the drag, we again take a control surface at the body

$$D = -2\pi r_0 \rho_1 \int_0^L \left(\frac{\partial \varphi_1}{\partial x}\right)_{r_0} \left(\frac{\partial \varphi_1}{\partial r}\right)_{r_0} dx = \frac{2\pi \rho_1 a_3 U_1 \epsilon}{\beta_1 K_1(\alpha r_0')} \int_0^{2\pi} \cos^2(\alpha x)\, d(\alpha x)$$

and, if we introduce the drag coefficient C_D again, using free-stream conditions U_2, ρ_2, where $C_D = D/\rho_2 U_2^2 \cdot \pi r_0 L$, we obtain

$$C_D = \frac{\rho_1^2 U_1^2}{\rho_2^2 U_2^2} \cdot \frac{(\epsilon/L)^2}{(i/L)^2\,(r_0/L)} \cdot \frac{1}{\pi^2 \beta_1^2 \beta_2^2 K_1^2(\alpha r_0')} \cdot \frac{1}{(BJ_1 + CJ_0)^2 + (BY_1 + CY_0)^2} \tag{36}$$

where, here again, the J_n and Y_n are evaluated at $\alpha i''$.

In Fig. 12 we have compared this expression with the drag coefficient of the same body in an entirely supersonic field, given by Eq. (26), and have also plotted the limiting case of r_0/L, i/L becoming infinite but keeping $(i - r_0)/L$ finite. We obtain for this case

$$\left(\frac{C_D}{C_{D_{\text{F.F.}}}}\right)_{\text{2-dim.}} = \frac{1}{\cosh^2 \alpha\beta_1 T + (\rho_2^2 U_2^2/\rho_1^2 U_1^2) \cdot (U_2^2 \beta_1^2/U_1^2 \beta_2^2) \sinh^2 \alpha\beta_1 T} \tag{37}$$

which is seen to give

$$\left(C_D/C_{D_{F.F.}}\right)_{2\text{-dim.}} = \left[(\epsilon_i/\epsilon)_{2\text{-dim.}}\right]^2$$

This two-dimensional expression obviously also has zero slope at the origin. The reason for the three-dimensional drag not vanishing so fast as the two-dimensional one, even though the amplitude of the bumps on its interface is smaller, is that the energy-radiating area increases as h, while it stays constant in the two-dimensional case.

This comparison shows us that three-dimensional bodies are affected much more rapidly at first by boundary-layer growth but that the effect is gradual after that initial plunge.

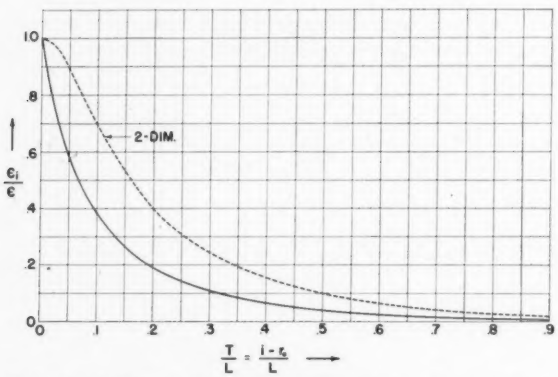

FIG. 12. Influence of boundary-layer thickness on wave drag.

REFERENCES

[1] Reissner, E., *On Compressibility Corrections for Subsonic Flow over Bodies of Revolution*, N.A.C.A. T.N. No. 1815, February, 1949.

[2] von Kármán, Th., *The Problem of Resistance in Compressible Fluids* (Volta Congress), Reale Academia d'Italia, Vol. XIV, pp. 42–44, 1936.

[3] Lamb, H., *Hydrodynamics*, pp. 293–299; Dover Publication, 1945.

[4] Lees, L., *A Discussion of the Application of the Prandtl-Glauert Method to Subsonic Compressible Flow over a Slender Body of Revolution*, N.A.C.A. T.N. No. 1127, September, 1946.

[5] Liepmann and Puckett, *Aerodynamics of a Compressible Fluid*, John Wiley & Sons, Inc., New York, 1947.

[6] Tsien, H. S., and Finston, M., *Interaction Between Parallel Streams of Subsonic and Supersonic Velocities*, Journal of the Aeronautical Sciences, Vol. 16, No. 9, p. 515, September, 1949.

[7] Watson, *Bessel Functions*, Chapt. XI; The Macmillan Company, New York, 1944.

Conical Flow Methods Applied to Uniformly Loaded Wings in Subsonic Flow

(*Continued from page 114*)

Since the x coordinate has been stretched by the amount $1/\sqrt{1-M^2}$ it is necessary to multiply the loading by $\sqrt{1-M^2}$ so that it remains invariant, and the slopes must be diminished by the factor $\sqrt{1-M^2}$; therefore Eq. (17) takes the form

$$z = \frac{(1-M^2)\,u_0}{\pi V}\left[2Q_1(x') + \log\left|x'^2 - 1\right|\right] + \text{constant} \qquad (49)$$

REFERENCES

[1] Jones, Robert T., *Subsonic Flow over Thin Oblique Airfoils at Zero Lift*, N.A.C.A. T. N. No. 1340, 1947.

[2] Hobson, E. W., *The Theory of Spherical and Ellipsoidal Harmonics*, pp. 163–164; Cambridge University Press, London, 1931.

[3] Busemann, Adolf, *Infinitesimal Conical Supersonic Flow*, N.A.C.A. T.M. No. 1100, 1947.

[4] Jones, Robert T., *Estimated Lift-Drag Ratios at Supersonic Speed*, N.A.C.A. T.N. No. 1350, 1947.

[5] Baldwin, Barrett S., Jr., *Triangular Wings Cambered and Twisted to Support Specified Distributions of Lift at Supersonic Speeds*, N.A.C.A. T.N. No. 1816, 1949.

Buckling Load of a Stepped Column

(*Continued from page 126*)

Eqs. (3) and (4) can be simplified to

$$y_i = \frac{M_0}{P} - \left(\frac{M_0}{P} - y_{i-1}\right)\cos\beta_i\lambda_i + \frac{y_{i-1}'}{\beta_i}\sin\beta_i\lambda_i \qquad (3e)$$

$$y_i' = \left(\frac{M_0}{P} - y_{i-1}\right)\beta_i\sin\beta_i\lambda_i + y_{i-1}'\cos\beta_i\lambda_i \qquad (4e)$$

Eq. (5) is then not needed.

The criterion for critical load is $y_n = M_0/P$.

If for convenience the arbitrary value of M_0 is taken as $M_0 = P$, then $M_0/P = 1$ in the above equations.

Fig. 4f, Cantilever, Several Loads.—$S = 0$ in Eqs. (3), (4), and (5). Start with $y_0 = 0$; M_0 = arbitrary; $y_0' = 0$ if left end is fixed or $y_0' = M_0/\omega_0$ if left end is elastically restrained.

The criterion for critical load is $M_n = 0$, or $M_0 = \sum Q_i y_i$.

REFERENCES

[1] Thomson, William T., *Matrix Solution of the n-Section Column*, Journal of the Aeronautical Sciences, Vol. 16, No. 10, pp. 623–624, October, 1949.

[2] Shanley, F. R., *Inelastic Column Theory*, Journal of the Aeronautical Sciences, Vol. 14, No. 5, pp. 261–268, May, 1947.

Readers' Forum

BRIEF REPORTS of investigations in the aeronautical sciences and discussions of papers published in the JOURNAL are presented in this special department. Publication will be completed approximately 8 weeks after receipt of the material. The Editorial Committee does not hold itself responsible for the opinions expressed by the correspondents. Contributions should not exceed 800 words in length.

Generalized Complex Forces in Flutter Calculations

J. E. V. Nilsson and N. B. Langefors
Stress Department, Saab Aircraft Company, Linköping, Sweden
October 18, 1950

BY THE INTRODUCTION OF generalized coordinates q_i in flutter calculations, one encounters the problem of determining the generalized complex air force P_i connected with each generalized coordinate (degree of freedom, mode of vibration). The usual way seems to be to calculate these generalized forces by forming the "virtual work done"

$$\delta W = \sum P_i \, \delta q_i = \sum P_{zj} \, \delta z_j \tag{1}$$

Against this method the objection has been made[1] that such a "work done" cannot be formed with the complex air forces. This objection seems to be correct, since δW in Eq. (1) is complex and cannot represent a work done in Lagrange's sense.

The introduction of generalized coordinates defines, however, a certain coordinate transformation

$$z = Aq \tag{2}$$

from which, in the real case, the transformation rule of the forces is obtained by the knowledge of the fact that the force vector multiplied by a deformation vector forms an invariant (the work done). In a similar way, the complex vectors form a complex invariant

$$\delta \bar{W} = \sum P_i \cdot \delta q_i^* \tag{3}$$

where δq_i^* is the conjugate vector of δq_i. That this is true is seen from the physical fact that the real and imaginary parts of $\delta \bar{W}$ form the active and reactive energy. In a similar manner to the real case, the transformation law of the complex force vector P is obtained from the invariant. It is

$$P = A_t^* P_z \tag{4}$$

where the subscript t indicates that the matrix has been transposed.

In flutter calculations, the generalized coordinates usually are introduced by a real transformation defining, for example, modes of vibration or the vibration amplitudes of a finite number of parts of the wing. Complex modes of vibration are then introduced by adding real forms multiplied by complex coefficients. In this case, when z and q are real, the matrix A is real, and, if P_z is complex, one obtains

$$\delta \bar{W} = \delta W_R + i \delta W_I = \sum P_{zjR} \, \delta z_j + i \sum P_{zjI} \, \delta z_j = \sum P_{iR} \delta q_i + i \sum P_{iI} \delta q_i \tag{5}$$

From this expression it is concluded that, under these conditions, the usual method represented by Eq. (1) defines the same transformation for the real and imaginary parts of P. This is also the case in Eq. (4) when A is real. The two methods are thus identical, and the usual method therefore gives correct results when z and q are real.

REFERENCE

[1] Greidanus, J. H., van de Vooren, A. I., *Mathematical Principles of Flutter Analysis*, Nationaal Luchtvaartlaboratorium Rapport F 43, Amsterdam, 1949.

Vibrations of Rectangular Plates

Harold Lurie
The RAND Corporation
November 6, 1950

THE NATURAL FREQUENCY OF RECTANGULAR PLATES with either clamped or simply supported edges is readily available. However, there is little direct information for plates with mixed edge conditions. In view of the fact that the vibration and buckling problems for a plate are identical eigenvalue problems, it would seem profitable to utilize for the vibration problem the large amount of data that the N.A.C.A. has computed for the buckling of rectangular plates. In particular, if two opposite edges are simply supported, the analogy is extremely simple, no matter what the other two boundary conditions may be. It can be easily shown how the fundamental frequency is determined as a function of the plate buckling factor k.

Let the rectangular plate be simply supported along the two edges $x = 0$ and $x = a$ and have various edge conditions along the other two edges $y = 0$ and $y = b$. Assuming a sine function in the x direction, the differential equation for $f(y)$ for buckling is[1]

$$\frac{d^4f}{dy^4} - \frac{2m^2\pi^2}{a^2}\frac{d^2f}{dy^2} + \left(\frac{m^4\pi^4}{a^4} - \frac{N_x}{D}\frac{m^2\pi^2}{a^2}\right)f = 0 \tag{1}$$

Similarly, the corresponding equation for free vibrations becomes[2]

$$\frac{d^4f}{dy^4} - \frac{2m^2\pi^2}{a^2}\frac{d^2f}{dy^2} + \left(\frac{m^4\pi^4}{a^4} - \frac{\mu\omega^2}{D}\right)f = 0 \tag{2}$$

The general solution for both Eqs. (1) and (2) can be written as

$$f(y) = C_1 \cosh \alpha y + C_2 \sinh \alpha y + C_3 \cos \beta y + C_4 \sin \beta y \tag{3}$$

where the corresponding values for α and β are: for buckling,

$$\alpha = \sqrt{\frac{m^2\pi^2}{a^2} + \sqrt{\frac{N_x}{D}\frac{m^2\pi^2}{a^2}}}; \quad \beta = \sqrt{-\frac{m^2\pi^2}{a^2} + \sqrt{\frac{N_x}{D}\frac{m^2\pi^2}{a^2}}} \tag{4}$$

and, for free vibrations,

$$\alpha = \sqrt{\frac{m^2\pi^2}{a^2} + \sqrt{\frac{\mu\omega^2}{D}}}; \quad \beta = \sqrt{-\frac{m^2\pi^2}{a^2} + \sqrt{\frac{\pi\omega^2}{D}}} \tag{5}$$

Considering the two edges $y = 0$ and $y = b$ to have the same boundary conditions in the vibration case as in the buckling problem, the constants of integration in Eq. (3) will be identical in terms of α and β for the two problems. Hence, for equivalence, let

$$\mu\omega^2/D = (N_x/D)(m^2\pi^2/a^2) \tag{6}$$

The coefficient k for critical buckling is defined as

$$N_x = k(\pi^2 D/b^2) \tag{7}$$

Substituting Eq. (7) into Eq. (6) yields

$$\omega^2 = (m^2\pi^4 D/\mu)[k/(ab)^2] \tag{8}$$

Hence, for any boundary conditions along the edges $y = 0$ and $y = b$, the value of k can be obtained from Timoshenko[1] or the various N.A.C.A. reports,[3,4] and the natural frequency can be computed from Eq. (8).

The vibration problem differs in one respect from the buckling phenomenon—viz., that for the former the fundamental mode always corresponds to $m = 1$. Hence, for the fundamental frequency, Eq. (8) becomes

$$\omega^2 = (\pi^4 D/\mu)[k/(ab)^2] \tag{9}$$

where k is the buckling constant for $m = 1$. This may not necessarily correspond to the lowest value of k for a given a/b ratio, whereas in the case of buckling k and m are always chosen to give the lowest value of k.

References

[1] Timoshenko, S., *Theory of Elastic Stability*, Sect. 65, p. 337; McGraw-Hill Book Company, Inc., New York, 1936.

[2] Voigt, W., *Bemerking zu dem Problem der transversalen Schwingungen rechtickiger Platten*, Nachrichten von der Kgl. Gesellschaft der Wissenschaften, Göttingen, 1893, p. 225.

[3] Lundquist, E. E., and Stowell, E. Z., *Critical Compressive Stress for Flat Rectangular Plates Supported Along All Edges and Elastically Restrained Against Rotation Along the Unloaded Edges*, N.A.C.A. T.R. No. 733, 1942.

[4] Lundquist, E. E., and Stowell, E. Z., *Critical Compressive Stress for Outstanding Flanges*, N.A.C.A. T.R. No. 734, 1942.

On Supersonic Wing-Body Center of Pressure

G. K. Morikawa and T. F. Coleman

Research and Development Laboratories, Hughes Aircraft Company, Culver City, Calif.

October 23, 1950

The representation of center of pressure for a general family of wing-body configurations (circular cylinder body with *no afterbody* and plan form made up of straight edges) in a stationary linearized supersonic flow may be considered simply for the limiting cases given by "slender body theory" and "strip theory." The results of reference 1 imply that the limiting cases yield the *bracketing limits* of the center of pressure. Results are presented here for the clipped-delta family of wing-body combinations for which the parameters are the diameter-span ratio, $\lambda \equiv a/s$ (where $0 \leq \lambda \leq 1$), the ratio of the tangent of the trailing edge angle (ω_1, cf. Fig. 1) to the tangent of the Mach angle, a_t (where $a_t \geq 0$), and the ratio of the tangent of the trailing edge angle (ω_1) to the tangent of the leading edge angle (ω_0), a_t/m (where $0 \leq a_t/m \leq 1$). The center of pressure C.P./C.P.$_0$ is expressed as a ratio where C.P.$_0$ is the center of pressure for the exposed wing alone referred to the root chord leading edge.

For $a_t = 0$ ("slender body theory," cf. reference 2),

$$\frac{\text{C.P.}}{\text{C.P.}_0} = \frac{1}{1-\lambda}\left[1 - \frac{3}{2}\lambda + 2\left(\frac{\lambda}{1+\lambda}\right)^2\right] \tag{1}$$

which is independent of the parameter a_t/m.

For $a_t = \infty$ ("strip theory," obtained by simple integrations),

$$\frac{\text{C.P.}}{\text{C.P.}_0} = \left[\frac{1 - \frac{1}{2}\left(\frac{a_t}{m}\right)}{1 - \frac{1}{3}\left(\frac{a_t}{m}\right)^2}\right] \times \left\{\frac{\left[1 - \frac{1}{3}\left(\frac{a_t}{m}\right)^2\right] + \lambda - \frac{\lambda^2\left(\frac{a_t}{m}\right)^2}{(1-\lambda)^3}\left[(1-\lambda^2) + 2\lambda \ln \lambda\right]}{\left[1 - \frac{1}{2}\left(\frac{a_t}{m}\right)\right] + \lambda + \frac{\lambda^2\left(\frac{a_t}{m}\right)}{(1-\lambda)^2}\left[(1-\lambda) + \ln \lambda\right]}\right\} \tag{2}$$

Eqs. (1) and (2) are plotted in Fig. 1 and indicate that the deviation of the center of pressure for the wing-body combinations as compared to the exposed wing alone is uniformly less than 7 per cent over the *entire range* of the parameters.

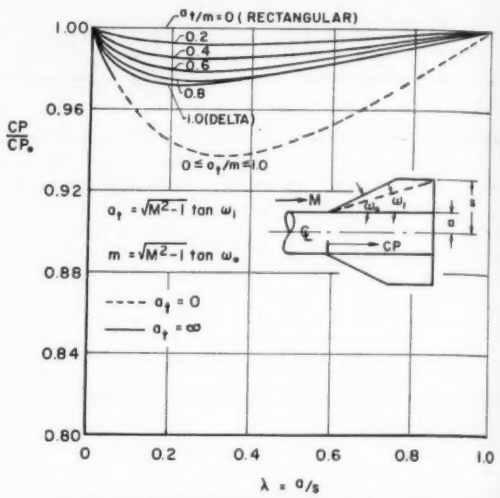

FIG. 1—CENTER OF PRESSURE FOR CLIPPED DELTA WING-BODY COMBINATION WITH NO AFTERBODY

References

[1] Morikawa, George K., *Supersonic Wing-Body Lift*, presented at the Annual Summer Meeting, I.A.S., Los Angeles, July 12–14, 1950. (To be published in the Journal of the Aeronautical Sciences.)

[2] Spreiter, John R., *Aerodynamic Properties of Slender Wing-Body Combinations at Subsonic, Transonic and Supersonic Speeds*, N.A.C.A. T.N. No. 1662, July, 1948.

Airplane Pitching Moment of Inertia

Innes Bouton

Chief Loads Engineer, McDonnell Aircraft Corporation, St. Louis

October 24, 1950

The pitching moment of inertia, I_y, of an airplane is needed to evaluate horizontal tail loads in maneuvers with pitching accelerations. Since the computation of I_y usually follows weight estimates of the detail parts of the airplane, the value of I_y is not available in the early stages of an airplane design when the tail loads are needed for design. Therefore, a reasonable estimate of I_y must be made from the available preliminary data.

A correlation between radius of gyration in pitch, k_y, and airplane length, from which the moment of inertia may be computed, has been established for several classes of airplanes. The correlation formula is $k_y = Cl_A$, where k_y is the radius of gyration in feet, C is a constant depending on type of airplane, and l_A is the overall length of the airplane. Table 1 notes the values of C determined from data on almost 100 different aircraft.

Table 1

Type Engines	No. of Engines	C
Turbojet	1 or 2	0.172
Piston	1	0.176
Piston	2	0.163
Piston	4 or more	0.158
Gliders		0.191

The standard deviation, σ, between the theoretical value determined with the constants above and the actual detailed

moment of inertia computations is approximately 20 per cent. The extremes of individual departures of the theoretical from the actual are plus 63 and minus 31 per cent, and these are values for extremes of configuration. A single value of C, 0.165, could be used for all classes of airplanes with the standard deviation only increasing to 22 per cent. The same single value for C is also obtained in reference 2. Improvement in the accuracy of individual estimates may be obtained by considering the location and relative size of large masses, such as the engines, fuel tanks, and turrets, and by adjusting the radius of gyration up or down slightly when the large masses are at the extreme ends of the airplane or near the c.g.

The method presented above is similar to the methods of references 1 and 2. Reference 3 presents a method that relates the pitching moment of inertia only to the weight as $I_y^{2/5} = 0.113W^{2/5}$. This latter method is of questionable validity and should be used with extreme caution in the design of airplanes, since the standard deviation for the 100 airplanes available is 87 per cent and the individual extremes are plus 346 and minus 68.7 per cent.

The McDonnell XF-85 parasite fighter illustrates the essential fallacy in predicting the moment of inertia without considering airplane length. This airplane is an unconventionally short airplane for its weight, so the method of reference 3 estimates an I_y that is 316 per cent too high. The method presented above predicts an I_y that is 26 per cent low.

References

[1] Gracey, W., *Measured Moments of Inertia of 32 Airplanes*, N.A.C.A. T.N. No. 780, 1940.

[2] Anon., *Empirical Formulae for Moments of Inertia of Aircraft*, R.A.E. Structures Report No. 28, 1948.

[3] Matheney, C. E., *Maximum Pitching Acceleration of Airplanes Measured in Flight*, N.A.C.A. T.N. No. 2103, 1950.

Base Pressures at Supersonic Speeds

J. Leith Potter

Assistant Professor, Department of Aeronautical Engineering, University of Alabama

November 16, 1950

A RECENT PAPER[1] PRESENTS an analysis of drag data for various two- and three-dimensional shapes. The author concludes that, depending upon body shape, the base drag coefficient at supersonic speeds assumes an approximately constant percentage of the theoretical limit, $2/\gamma M^2$. After considering the data available to him, the author suggests that $C_{DB} = 0.7/M^2$ for typical projectiles. Furthermore, he proposes to use a curve of $C_{DB}/C_{DB_{max.}}$ as a function of $(\Delta P_B/q)_{subsonic}$ to estimate base drag coefficients in supersonic flow. The purpose of the present writer is to expand the discussion of base pressures by reviewing some additional data[2] on simple bodies of revolution and circular discs. It will be shown that the processes suggested in reference 1 may easily lead to excessive errors even when used only for purposes of rough estimation.

First consider Fig. 1, where it will be noted that there is considerable effect on C_{DB} due to variations in body length and boat-tailing. No single function of Mach Number alone can be expected to satisfactorily express C_{DB}. In general, it would seem that a method for estimating C_{DB} should take into account the effects of Mach Number, body geometry, and Reynolds Number. This is proved by reference 3 and several unpublished Naval Ordnance Laboratory reports[2] on the subject. The importance of these factors seems to have been recognized in reference 1, but the final recommendations as expressed in Figs. 13 and 14 and paragraph 4 of the "Results" do not clearly indicate how they are

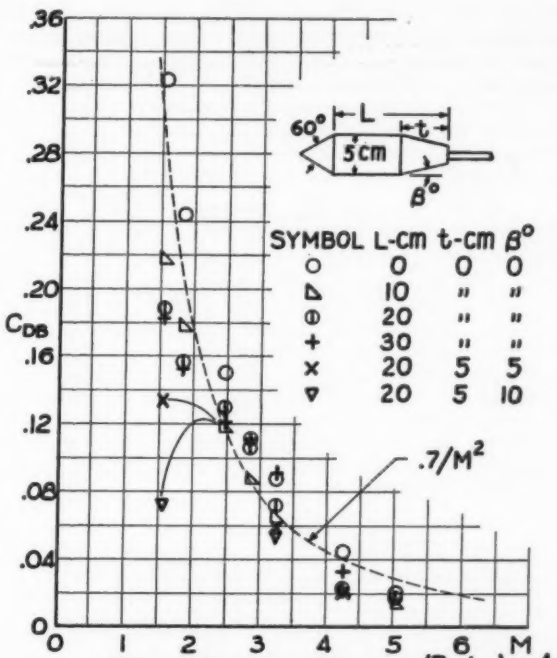

FIG. 1. BASE DRAG COEFFICIENT OF CONE–CYLINDER BODIES

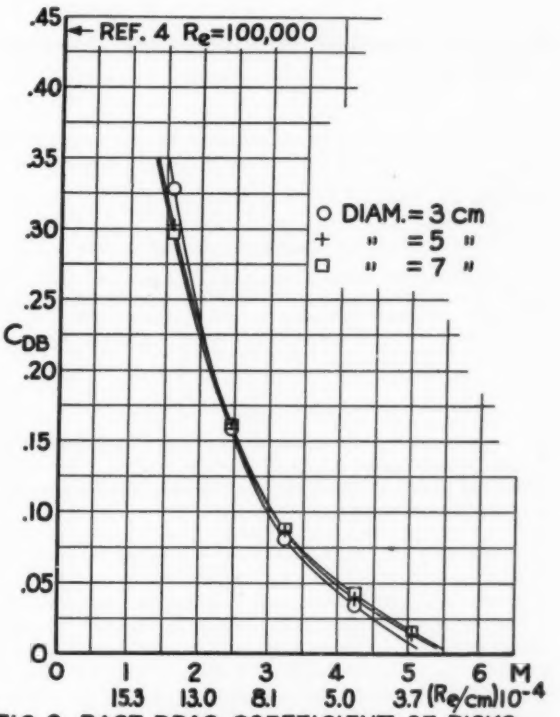

FIG. 2. BASE DRAG COEFFICIENT OF DISKS

to be taken into account. It might be added here that all the available data are not plotted on Fig. 1 of the present comments, since the general trend is sufficiently illustrated by the points

shown. Also, the points for missiles having no boat-tails may be considered corrected for sting effects. Sting diameter for the boat-tail investigations was 1.27 cm., and the corresponding correction has not been determined as yet.

Reference to Fig. 2 will prove that it is risky to estimate base drag on the basis of $(\Delta P_B/q)_{subsonic}$. If $(\Delta P_B/q)_{subsonic} = -0.44$ is taken[4] for a disc at high Reynolds Numbers, one may go to Fig. 14 of reference 1 and find $C_{DB}/C_{DB_{max.}} = 0.7$ at supersonic speeds. However, this value could easily be several hundred per cent in error, since the data of Fig. 2 in this discussion indicate a range of $C_{DB}/C_{DB_{max.}}$ from 0.26 to 0.70 for Mach Numbers between 1.56 and 5.05. It is noted that $(\Delta P_B/q)_{subsonic} = -0.7$ is labeled "disc—Fig. 9" on Fig. 14 of reference 1, but a value of -0.5 is given for a simple disc on the referenced Fig. 9. This is unexplained.

One may conclude that there is a need for much more analytical and experimental investigation before base drag coefficients can be predicted with reasonable accuracy for many common aerodynamic bodies. Typical data such as are presented in Fig. 1 definitely establish the importance of boundary-layer flow in determining base pressures.

References

[1] Hoerner, Sighard F., *Base Drag and Thick Trailing Edges*, Journal of the Aeronautical Sciences, Vol. 17, No. 10, pp. 622–628, October, 1950.

[2] Unpublished U.S. Naval Ordnance Laboratory Aeroballistics Division data (unclassified).

[3] Chapman, Dean R., *An Analysis of Base Pressure at Supersonic Velocities and Comparison with Experiment*, N.A.C.A. T.N. No. 2137, July, 1950.

[4] Rouse, Hunter, *Elementary Mechanics of Fluids*, p. 236; John Wiley & Sons, Inc., New York, 1946.

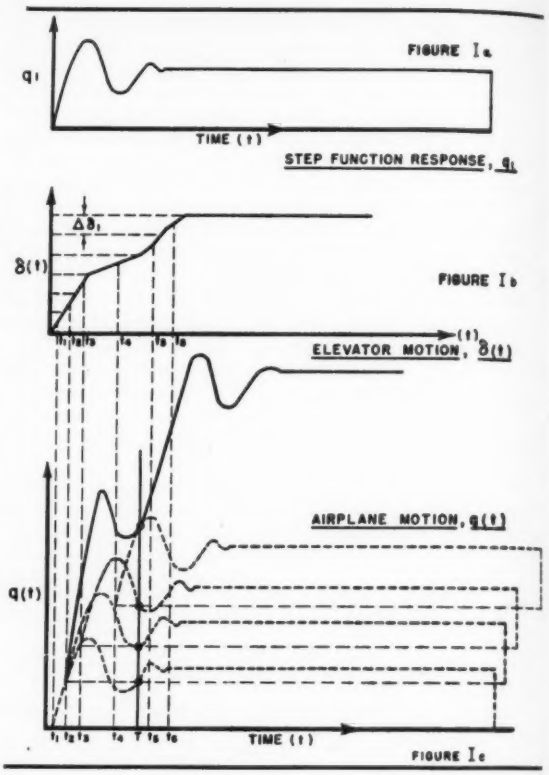

A Simple Graphical Solution of the Duhamel Integral

E. V. Laitone and J. T. Ahlin

Associate Professor, University of California at Berkeley, and Research Engineer, Santa Monica Plant, Douglas Aircraft Company, Inc., Respectively

November 17, 1950

Summary

A graphical solution of the Duhamel Integral is presented which will quickly determine any airplane motion caused by a given control surface deflection. This method also solves the inverse problem, determining the required control surface deflection for any desired motion. It also determines the unit response to a step deflection of the control surface if the response to any arbitrary control surface pulse-type deflection is known.

Discussion

If the so-called indicial response to a step increment of the elevator deflection δ is known, then the time variation of the response q to any arbitrary elevator deflection can be obtained from the Duhamel Integral as[1]

$$q(t) = \int_0^t \dot{q}_1(t-\tau)\, d\delta(\tau) = \int_0^t \frac{d\delta(\tau)}{d\tau}\, q_1(t-\tau)\, d\tau \qquad (1)$$

In reference 1, Jones obtained a graphical solution of Eq. (1) by decomposing the time axis into equal increments. This approach results in an extremely tedious and time-consuming graphical integration. Because of these difficulties, another numerical method has been proposed that does not use the Duhamel Integral; this is the A.A.F. Linear Increment Tabular Integration method of reference 2. This method depends on an approximation of the elevator motion by superposition of linear elements after obtaining the response to a linear elevator deflection from the equations of motion. Thus, at the end of a linear approximation, the approximation must be subtracted out and the succeeding one added in. A lengthy tabular integration is then necessary before the airplane motion is determined. Moreover, this method is not readily applicable to recorded elevator motions that are highly irregular.

The first form of the Duhamel Integral suggests a simpler graphical solution by a decomposition of the elevator deflection into equal increments whereby the elevator deflection δ rather than time $t = \tau$ is taken as primary variable of integration. It is observed that Eq. (1) is approximately

$$q(t) = \sum q_1(t-\tau)\, \Delta\delta_1. \qquad (2)$$

As an example of this method, the pitching motion of an airplane is obtained using a representative indicial response and elevator deflection time history.

From the equations of motion for pitching, as given in reference 2, the response q to a unit step in elevator angle δ_1 is

$$q_1 = \frac{-Z_w M_\delta}{c}\left(1 - e^{-(b/2)t}\sqrt{\frac{c + (bc/Z_w) + (c/Z_w)^2}{c - (b^2/4)}}\right.$$
$$\left.\sin\left\{\sqrt{c - \frac{b^2}{4}}\, t + \tan^{-1}\left[\frac{\sqrt{c - (b^2/4)}}{(b/2) + (c/Z_w)}\right]\right\}\right)$$

with

$$b = -\left[\frac{Z_w}{1 - Z_{\dot{w}}} + M_q - \frac{(U_0 + Z_q)}{1 - Z_{\dot{w}}}\, M_{\dot{w}}\right]$$

and

$$c = [1/(1 - Z_{\dot{w}})]\,[Z_w M_q - (U_0 + Z_q)\, M_w]$$

The aircraft pitching velocity q response to a 1° elevator step (an instantaneous 1° elevator deflection from its trim position at time $t = 0$) is plotted in Fig. Ia.

If the plot of q_1 in Fig. Ia is cut out and used as a template, then the graphical construction for an arbitrary elevator motion,

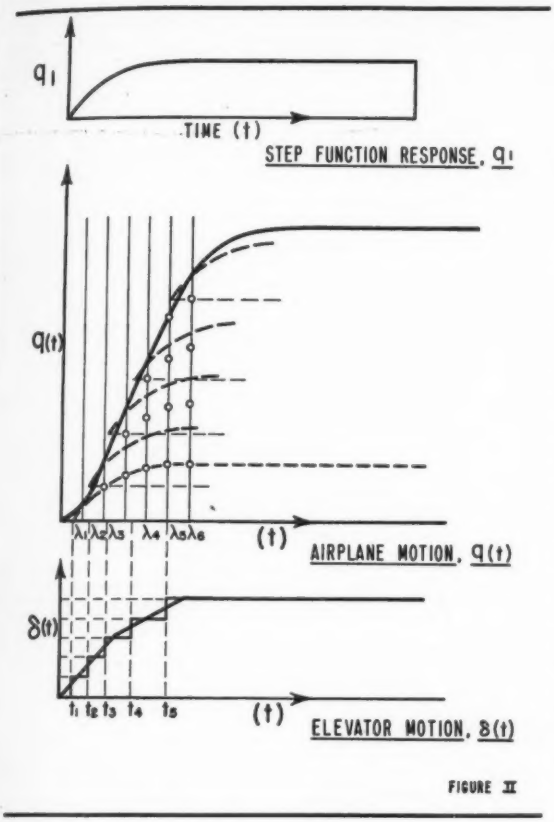

FIGURE II

as in Fig. Ib for example, proceeds as a simple summation of the template ordinates for *equal* increments of $\Delta\delta$, as shown in Fig. Ic.

The example demonstrates how the response can be obtained from an arbitrary elevator time history by summing the proper template ordinates at any desired time T to obtain $q(t)$ at that selected time. To accomplish this, the elevator deflection is decomposed into equal increments ($\Delta\delta_1$), and the step function response q, for $\Delta\delta_1$, is applied successively at the points $t_1, t_2, \ldots, t_k$, where $t_k \leq T$, each time adding the new ordinate to the one previously determined by placing the bottom of the template on the previous point and marking the intersection of the top of the template with the vertical line from T. The points ($t_1, t_2, \ldots, t_k, \ldots, t_r$) correspond to the midpoints of each $\Delta\delta_1$ increment. If the elevator deflection is negative, the corresponding step function increment naturally should be subtracted from previously determined points.

The usually difficult inverse problem of determining the elevator deflection $\delta(t)$ required to produce a given motion $q(t)$ can be solved readily by using the indicial response template and a simple graphical construction. The example in Fig. II illustrates this method.

In this case, the airplane response is divided into equal time increments ($\lambda_1, \lambda_2, \ldots, \lambda_m$), and vertical lines are drawn from each to intersect the curve $q(t)$. The template is now moved horizontally along $q(t) = 0$ until its top contour passes through the intersection of $q(t)$ and λ_1. The origin of the template then gives the time (t_1) corresponding to the midpoint of the elevator step increment required to produce this response. At each of $\lambda_2, \lambda_3, \ldots, \lambda_m$, the intersection of the template profile is marked, thus indicating the airplane motion due to the step increment at $t = t_1$.

The template is moved vertically until the bottom rests on the point just marked on λ_2. Then it is moved horizontally until the contour passes through the intersection of $q(t)$ and λ_2. The origin of the template now gives the abscissa $t = t_2$. Keeping the origin on the vertical line $t = t_2$, the template is moved vertically until the ordinate contributions due to the step at $t = t_2$ have been added to each ordinate previously marked on $\lambda_3, \lambda_4, \ldots, \lambda_m$. This process is continued until the steps determined produce the final airplane motion.

The amplitude of each equal step is determined already by the step function response. Hence, the cascade of steps shown in Fig. II is known. A smooth curve giving the required elevator time history can then be found by fairing through all the equal elevator step increments.

The practical problem of finding the indicial step from any measured airplane motion due to an arbitrary elevator time history can be obtained by trial and error, using elements of this graphical method. After the elevator motion has been represented by step approximations for equal $\Delta\delta$ increments, the problem reduces to one of determining the template necessary to produce the given airplane motion. This is most easily accomplished by attempting to reproduce the airplane motion with a trial template and correcting this template whenever necessary. A linear template should be used as the first approximation. Then the time abscissa γ_1 is determined, beyond which the template fails to yield the correct airplane response. At some later time abscissa γ_2, any discrepancy between the result obtained by using this trial template and the true curve should be algebraically subtracted from the corresponding trial template ordinate at $t = \gamma_2$. This new point should be connected with the ordinate at γ_1 by a straight line, thus yielding a new trial template. A continuation of this iteration process determines the indicial response curve to any desired accuracy by a series of straight lines.

The template method has proved simple, rapid, and accurate in practice. However, it is felt that the versatility of the method is its prime asset, because of the many applications and simplifications that appear.

References

[1] Jones, Robert T., *Calculation of the Motion of Airplanes Under the Influence of Irregular Disturbances*, Journal of the Aeronautical Sciences, Vol. 3, No. 12, pp. 419–425, October, 1936.

[2] Kelly, Joseph, Jr., and Missall, John W., *Maneuvering Horizontal Tail Loads*, Army Air Force Technical Report No. 5185, January 25, 1945.

Aerodynamics of Blasts

L. Ting and H. F. Ludloff
Daniel Guggenheim School of Aeronautics, New York University
November 30, 1950

A THEORY HAS BEEN developed by means of which the pressure and density fields behind blasts passing over arbitrary surfaces can be obtained in explicit analytic form. Assume that an originally plane shock front of given intensity (strong or weak) advances over the surface $f(z)$ of a given thin airfoil or other flat structure. If the inclination of this surface with regard to the direction of propagation of the shock is relatively small, the advancing front will end perpendicularly on the surface at any instant, so that a curved shock front results, as well as a shock configuration that may be interpreted as Mach reflection. Because of the curvature of the shock, the flow behind (the front) is rotational and, for sufficiently strong blasts, is supersonic with regard to the airfoil. Such a case is treated here as a time-dependent perturbation problem, the undisturbed system being the advancing plane shock front and the disturbance being caused by the inclination of the surface $f(z)$.

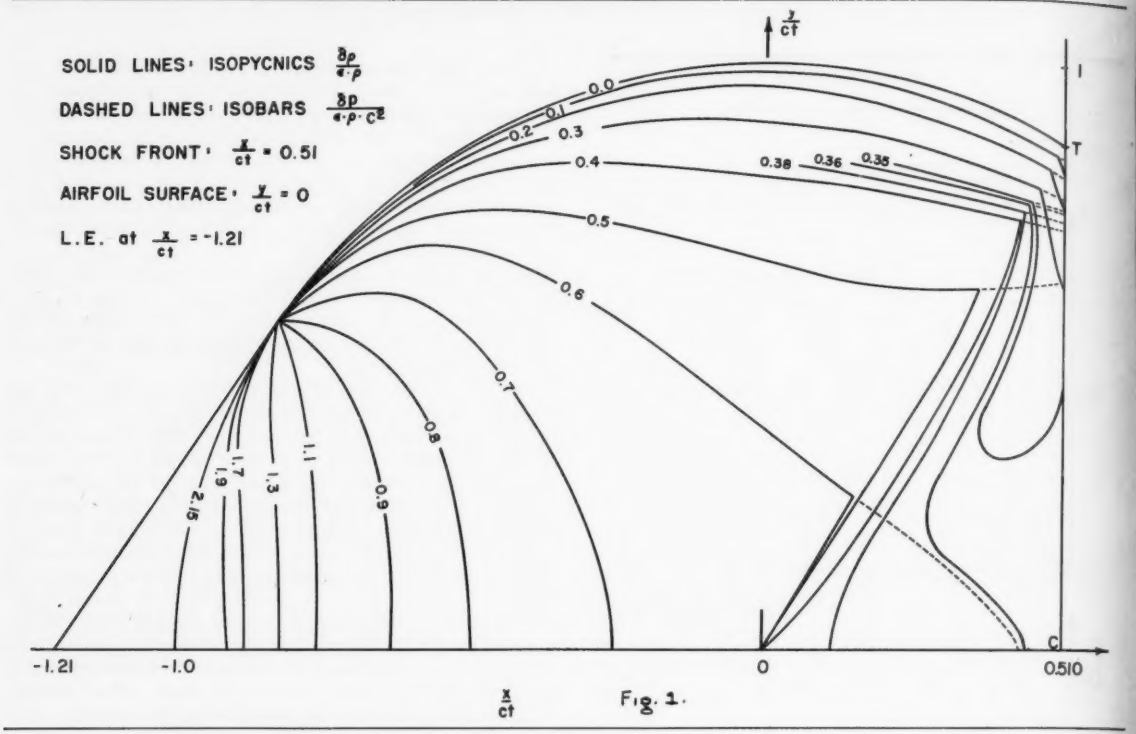

Fig. 1.

Taking into account the rotationality of the flow, it turns out that the disturbance pressure δp satisfies the wave equation. In addition, the usual boundary condition on the airfoil (or other) surface and the conservation laws applied across the disturbed shockfront must be fulfilled. Fixing (x, y, t) in the undisturbed flow behind (the shock) and subsequently introducing $(\bar{x}, \bar{y}, \bar{t})$ obtained from the first system by means of a Lorentz transformation, the following analytic problem may be formulated:

Differential Equation:

$$\Delta(\delta p) - (1/c^2)(\delta p)\bar{t}\bar{t} = 0 \tag{1}$$

Boundary Conditions:

(*Surface*)

$$\text{At } \bar{y} = 0,\ \bar{x} < 0: \quad (\delta p)_{\bar{y}} = A_0 f''\{a[c\bar{t} + (\bar{x}/\lambda_0)]\} \tag{2}$$

(*Shock Front*)

$$\text{At } \bar{y} \geq 0,\ \bar{x} = 0: \quad D^{(2)}(\delta p) = o \tag{3}$$

where $D^{(2)}$ is a differential operator, of the second order, in $\bar{x}$ and $\bar{t}$ and where the parameters A_0, a, and λ_0 are simple (rational) expressions in terms of the shock velocity U_0 relative to the airfoil and the velocity U and Mach Number M of the shock relative to the undisturbed flow behind.

It is now an essential point of this theory that, using some "lost boundary conditions," (3) can be replaced by the condition:

(*Reflected Surface*)

$$\text{At } \bar{y} = 0,\ \bar{x} \geq 0: \quad (\delta p)_{\bar{y}} = \sum_{i=1}^{3} A_i f''\{a[c\bar{t} - (\bar{x}/\lambda_i)]\} \tag{4}$$

where again the A_i and λ_i are simple expressions in U_0, U, and M.

This step makes it possible to solve the boundary value problem in terms of a Possio solution:

$$\delta p(\bar{x}, \bar{y}, \bar{t}) = -\frac{1}{\pi}\int d\tau \int d\xi \frac{(\delta p)_y(\xi, 0, \tau)}{\sqrt{(\bar{t} - \tau)^2 - (1/c^2)[(\bar{x} - \xi)^2 + \bar{y}^2]}} \tag{5}$$

After substituting for $(\delta p)_y$ from Eqs. (2) and (4), the integration is carried out over all values of ξ and τ for which the denominator is real. Expression (5) for δp is valid for any surface $f(x)$. This result is not restricted to conical fields as were the results of previous investigations along similar lines.

In order to compare with shock tube experiments, it is necessary to compute also the density field. Note that the isopycnics that appear in any interferogram will differ from the isobars in rotational flow. It turns out that here the rotational flow is confined to a triangular domain $T0C$, immediately behind the shock front. One obtains

$$\delta\rho = \frac{1}{c^2}\{\delta p(\bar{x}, \bar{y}, \bar{t}) - \Omega \cdot \delta p[0, \bar{y}, \bar{t} - (\bar{x}/cM)]\} \tag{6}$$

For a diamond profile, Eq. (5) can be evaluated explicitly. Using physical coordinates, one obtains simply

$$\delta p = K_0 \cdot \cos^{-1}\frac{ct + \lambda_0 x}{\sqrt{(\lambda_0 \cdot ct + x)^2 + (1 - \lambda_0^2)y^2}} + \sum_{i=1}^{3} K_i \cdot \cos^{-1}\frac{ct - \lambda_i x}{\sqrt{(\lambda_i ct - x)^2 + (1 - \lambda_i^2)\cdot y^2}} \tag{7}$$

and a similar expression for $\delta\rho$. If the shock is behind the maximum thickness point, three more $\cos^{-1}$ terms have to be added in Eq. (7). Again, Ω and K_i are simple expressions in U_0, U, and M.

In Fig. 1, the curves of constant pressure and density are plotted for $(U_0 - U)/c = 1.21$, in accordance with Eq. 7 and the similar expression for $\delta\rho$. It is interesting to note how strongly and suddenly each isopycnic splits off from the corresponding isobar after traversing the demarkation line between irrotational and rotational flow. The point 0 is a singular point, in which a large number of isopycnics ends. Within a thin strip along $0T$, there is a steep density gradient, while there is no appreciable pressure gradient. In other words, a slipstream is obtained. Such result must be expected with every Mach reflection and can be clearly seen in W. Bleakney's interferograms.